Broadband coherent Raman scattering microscopy

Dario Polli[1,2], Vikas Kumar[1], Carlo M. Valensise[1], Marco Marangoni[1] and Giulio Cerullo[1]*

*Corresponding Author: E-mail: giulio.cerullo@polimi.it

[1] IFN-CNR, Dipartimento di Fisica, Politecnico di Milano, Piazza Leonardo da Vinci 32, 20133, Milan, Italy
[2] Center for Nano Science and Technology at Polimi, Istituto Italiano di Tecnologia, Milano 20133, Italy

Abstract

Spontaneous Raman (SR) microscopy allows label-free chemically specific imaging based on the vibrational response of molecules; however, due to the low Raman scattering cross section, it is intrinsically slow. Coherent Raman scattering (CRS) techniques, by coherently exciting all the vibrational oscillators in the focal volume, increase signal levels by several orders of magnitude. In its single-frequency version, CRS microscopy has reached very high imaging speeds, up to the video rate; however, it provides an information which is not sufficient to distinguish spectrally overlapped chemical species within complex heterogeneous systems, such as cells and tissues. Broadband CRS combines the acquisition speed of CRS with the information content of SR, but it is technically very demanding. This paper reviews the current state of the art in broadband CRS microscopy, both in the coherent anti-Stokes Raman scattering (CARS) and the stimulated Raman scattering (SRS) versions. Different technical solutions for broadband CARS and SRS, working both in the frequency and in the time domains, are compared and their merits and drawbacks assessed.

1. Introduction

Optical microscopy represents an extremely powerful investigation tool for life sciences, thanks to its ability of visualizing morphological details in cells and tissues on the sub-micrometer scale. [1] It provides a much higher spatial resolution compared to magnetic resonance imaging, and, at the same time, it does not require the fixation of the sample, as in electron microscopy, thus enabling to work on unprocessed specimens or *in vivo*. Fluorescence microscopy using exogenous (such as dyes or semiconductor quantum dots [2]) or endogenous (such as fluorescent proteins [3]) markers offers a superb sensitivity, down to the single molecule limit. However, the addition of fluorescent markers can hardly be implemented within certain cells or tissues, and in many cases, it gives a strong perturbation to the investigated system. This is particularly true for small molecules, for which the size of the marker is comparable to or even bigger than that of the molecule itself, so that it heavily interferes with its biological function. Finally, cells are susceptible to phototoxicity, particularly with short-wavelength light excitation, which is further enhanced by reactive chemical species generated by the fluorescent molecules under illumination. For these reasons, a broad class of problems in life sciences and in biomedicine call for intrinsic, label-free imaging methods that do not require the addition of any fluorescent molecule.

Every component of a biological specimen (cell or tissue) is characterized by a vibrational spectrum that reflects its molecular structure and provides an endogenous and chemically specific signature that can be exploited for its identification. Vibrational absorption microscopy [4] uses mid-infrared (MIR) light (λ = 3-10 μm), directly resonant with vibrational transitions of the molecule; however, the required long wavelengths result in low spatial resolution and limited penetration depth due to water absorption. Spontaneous Raman (SR) microscopy [5] overcomes these limitations since it uses visible or near-infrared (NIR) light, which provides much higher penetration depth and spatial resolution with respect to its MIR counterpart. In the

SR process the incoming quasi-monochromatic laser light at frequency ω_{pu} (pump frequency) excites the molecule to a virtual state, from which it relaxes to the ground state emitting a photon with lower energy at frequency ω_S (Stokes frequency). As depicted in **Figure 1** (a), $\omega_S = \omega_{pu} - \Omega$ is down-shifted in frequency by the molecular vibration at frequency Ω, which is specific to the chemical bonds and symmetry of the probed molecule. Since a molecule has several vibrational mode frequencies, the SR signal has corresponding discrete bands constituting altogether a wide spectrum red-shifted with respect to the pump light frequency. SR is able to identify selectively many types of biomolecules found in human tissues and cells. [6], [7] The detailed chemical information provided by SR enables a clear distinction between states of a dynamical process: there are already many encouraging reports of the diagnostic success of this technique in cancer research. [8]-[11] SR can detect biochemical differences in irradiated cells and discriminate between normal and cancerous state for skin, bladder and gastric tissues, rat fibroblast cells, human bone and human epithelial cells from a variety of organs.
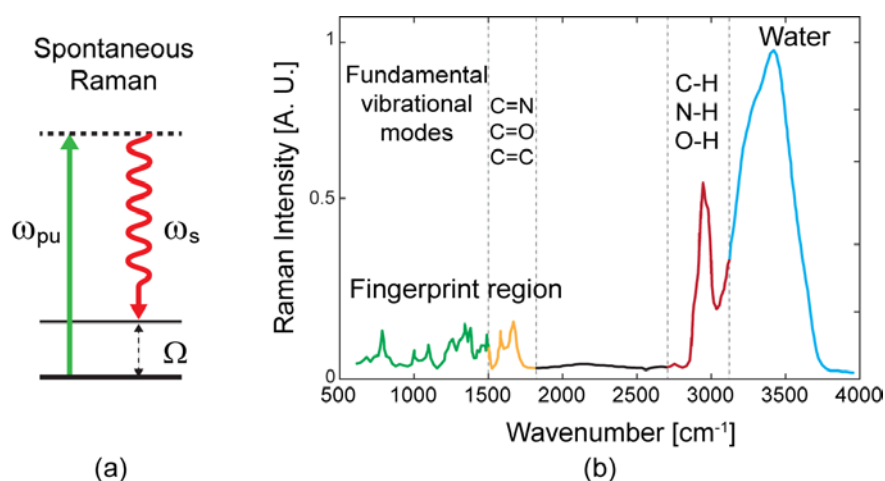
Figure 1 (a) Schematic of the energy levels involved in a Spontaneous Raman (SR) process. (b) SR spectrum (obtained with 514.5 nm laser excitation) of P22 virus at 80 µg/µL concentration in H_2O buffer at 20 ºC, highlighting the most relevant vibrational transitions. The main structurally informative Raman bands occur in the 600–1800 cm^{-1} interval. Figure adapted from [13].

In a typical Raman spectrum there are two vibrational frequency intervals of interest, where specific molecular signatures are clearly identified. This is exemplified in Figure 1 (b), which reports the SR spectrum of a P22 virus in H_2O buffer obtained by irradiation at 514.5 nm (or 19436 cm^{-1} in wavenumber units) with an Ar-ion laser. [13] The most important interval for chemical identification is the so-called fingerprint region in the low wavenumber (600-1800 cm^{-1}) portion of the spectrum (see the green-yellow region in Figure 1 (b)). Here the Raman spectrum contains multiple contributions from proteins and nucleic acids. Vibrational features of proteins arise from aromatic amino acids (phenylalanine, tyrosine and tryptophan), amide groups (especially in the 1500-1700 cm^{-1} region) of secondary protein structures and the stretching or deformation of carbon atoms bonded with nitrogen (C-N stretch), hydrogen (C-H rock, bend or scissoring) or other carbon atoms (C-C stretch). Nucleic acid features include contributions from individual RNA and DNA bases, as well as from the sugar-phosphate backbone of DNA. Double bonds such as C=N, C=O and C=C can be typically monitored in the 1500-1800 cm^{-1} frequency interval (see the yellow region in Figure 1 (b)). The second region of interest is the high wavenumber window (2700-3100 cm^{-1}), where the Raman spectrum is a superposition of broad features (see the red region in Figure 1 (b)) dominated by the stretching of the hydrogen bonds (C-H, N-H, O-H). It is thus well suited for studying long-chain hydrocarbons and lipids (fats, waxes, sterols, fat-soluble vitamins, mono-, di- and triglycerides, phospholipids…). Finally, for wavenumbers longer than 3100 cm^{-1} a very broad and intense Raman peak of water is found. Further extension of the observation window to the silent region (1800 to 2800 cm^{-1}) can be obtained by using some Raman-tag molecules which provide signal without interfering with the biological constituents. [14]-[16] All these signatures at different frequencies provide useful information in order to correctly identify states of cells and tissues.

The main drawback of SR microscopy is its very low scattering cross section, about 10 to 12 orders of magnitude lower than the absorption cross section of molecules, resulting in a

weak incoherent signal which is emitted isotropically from the irradiated volume. As a result, many practical difficulties arise:

(i) it is difficult to separate the weak inelastically scattered SR light from the intense Rayleigh scattered laser light and from the sample fluorescence, which gives rise to a broad baseline, to be subtracted using post-processing methods;

(ii) it is challenging to probe diluted species by SR;

(iii) the required long integration times - seconds or even minutes to obtain Raman spectra with sufficient signal-to-noise ratio (SNR) - make image acquisition times unacceptably long and prevent real-time imaging of dynamical processes in living cells or tissues.

These limitations of SR can be overcome by the use of Coherent Raman Scattering (CRS) techniques. [17], [18] CRS is a class of third-order nonlinear optical spectroscopies which employ a sequence of light pulses to set up and detect a vibrational coherence within the ensemble of molecules inside the laser focus. CRS uses the combination of two pulses, the pump (ω_{pu}) and the red-shifted Stokes (ω_S), to induce collective molecular oscillations in the focal volume. When the difference between pump and Stokes frequencies matches a characteristic vibrational frequency Ω, i.e. $\omega_{pu} - \omega_S = \Omega$, then all molecules are resonantly excited and vibrate in phase. This vibrational coherence enhances the Raman response by many orders of magnitude with respect to the incoherent SR process. In addition, the CRS signal is emitted in a coherent beam, propagating in a direction satisfying a phase-matching condition for the CRS process, and can be easily collected by the detector. CRS microscopy thus provides the following advantages:

(i) in comparison with fluorescence microscopy it is label-free, because it does not require fluorophores or staining, allowing the study of unaltered cells and tissues;

5

(ii)   it typically works out of resonance, i.e. without population transfer into electronic excited states of the molecule, thus minimizing photobleaching and damage to biological samples;

(iii)   since CRS exploits a coherent superposition of the vibrational responses from the excited oscillators, it provides a considerably stronger signal than SR microscopy, allowing for much higher imaging speeds;

(iv)   since CRS is a nonlinear microscopy technique, the signal is generated only in the focal volume, thus exhibiting three-dimensional sectioning capability without need of any physical confocal apertures, similar to multiphoton fluorescence microscopy; [19]

(v)   excitation in the NIR (700-1200 nm) has the advantage of relatively low light absorption by tissues *in vivo* and reduced light scattering by turbid media, so that a high penetration depth (typically in the 0.1-1mm range) is achievable through thick tissues. Furthermore, in this spectral region multi-photon absorption is less probable, so that phototoxicity and tissue damage are greatly reduced.

The two most widely employed CRS techniques are coherent Anti-Stokes Raman scattering (CARS) [20]-[22] and stimulated Raman scattering (SRS). [23]-[25] In the SRS process (**Figure 2** (a)) the coherent interaction with the sample induces stimulated emission from a virtual state to the investigated vibrational state, resulting in a Stokes-field amplification (Stimulated Raman Gain, SRG) and in a simultaneous pump-field attenuation (Stimulated Raman Loss, SRL). In the CARS process (Figure 2 (b)) the vibrational coherence is read by a further interaction with a probe beam at frequency ω_{pr}, generating a coherent radiation at the anti-Stokes frequency $\omega_{aS} = \omega_{pr} + \Omega$ (typically one chooses $\omega_{pr} = \omega_{pu}$ so that $\omega_{aS} = \omega_{pu} + \Omega$). As it will be discussed in detail in the following, CARS and SRS present advantages and drawbacks, so that they are both actively investigated in view of applications.
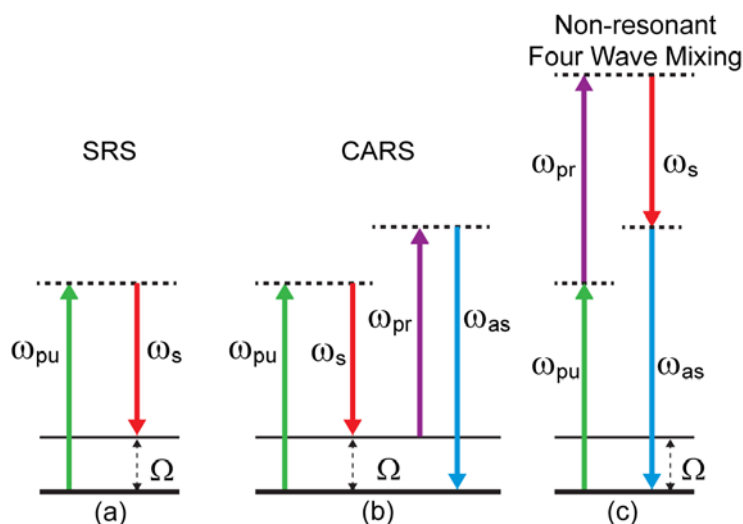
Figure 2 Schematic of energy levels and fields involved in different CRS processes: the resonant SRS (a) and CARS (b), and the non-resonant four-wave-mixing process that is responsible for the NRB in CARS.

Current implementations of CRS, while achieving extremely high acquisition speeds up to the video rate, [26], [27] mostly work at a "single frequency": this name does not indicate a continuous wave (CW) excitation, but the use of picosecond pump and Stokes pulses with an optical bandwidth of a few wavenumbers, matching the typical width of Raman modes in the condensed phase and targeting a single vibrational transition. The single-frequency regime has been successfully employed to track the presence of a molecular species with a specific and rather isolated Raman response, but it is not sufficient to distinguish different components within complex heterogeneous systems, such as cells and tissues, with spectrally overlapped chemical species. SR, on the other hand, provides the full vibrational spectrum and thus contains the maximum amount of chemical information, allowing subtle differentiation between species; however, it suffers from exceedingly long integration times. The obvious solution to this problem is broadband CRS microscopy, which combines the high acquisition speed of coherent techniques with the high information content of SR, as schematically depicted in **Figure 3**.
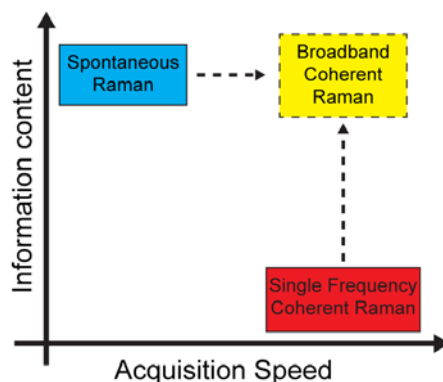
Figure 3 Comparison between spontaneous and coherent Raman scattering techniques in terms of imaging speed and information content.

Broadband CRS microscopy, for reasons that will be clarified in this paper, is technically very challenging and not yet as mature as its single-frequency counterparts, with many different configurations that have been proposed and experimentally demonstrated. According to the nomenclature commonly used in the literature, broadband CRS techniques can be classified according to two categories: (i) hyperspectral CRS, which makes use of a single-frequency CARS/SRS configuration with narrowband pump and Stokes pulses whose detuning is rapidly scanned to build a CARS/SRS spectrum; (ii) multiplex CRS, in which at least one of the pump/Stokes pulses is broadband and the CARS/SRS spectrum is recorded either in the frequency domain by a multichannel detector or in the time domain by a Fourier transform (FT) approach. In its simplest form (other forms will be discussed later on) the conceptual scheme of multiplex CARS and SRS makes use of a narrowband picosecond pump beam and a broadband femtosecond Stokes beam, whose interaction with the sample, as reported in **Figure 4**, populates an ensemble of vibrational levels. In the CARS regime (a), the discrimination between the levels necessarily requires that the vibrational coherence is read out by a narrowband beam, which in the simplest case consists of the pump beam itself. Differently, in SRS, where the vibrational signature can be detected either as a frequency-dependent Stokes amplification (SRG) or as frequency-dependent pump attenuation (SRL), one may either recur to a combination of narrowband pump and broadband Stokes (SRG detection, (b) and (d) panel)

or to a combination of broadband pump and narrowband Stokes (SRL detection, (c) and (e) panel). The latter configuration is also known as inverse Raman scattering (IRS). [28]
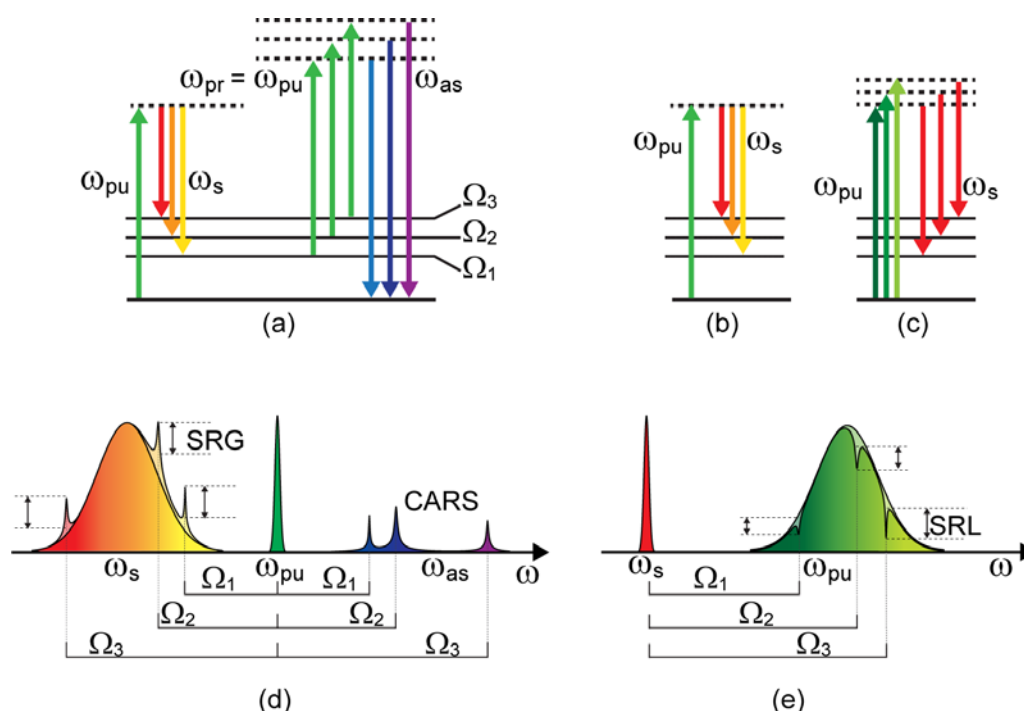

Figure 4 Schematic of energy levels and fields involved in: (a) broadband CARS; (b) SRS with broadband Stokes; (c) SRS with broadband pump. Pump/Stokes spectra and nonlinear signals for the cases of broadband Stokes (d) and broadband pump (e).

This paper reviews the state of the art of broadband CRS techniques, both in the CARS and the SRS modalities. While principles and applications of CRS microscopy have been already deeply reviewed, [17], [18], [29]-[35] this paper has a more technical connotation andfocuses on the description and on the comparative analysis of the many solutions that have been proposed in order to speed up the acquisition broadband CARS/SRS spectra. It is organized as follows; Section 2 recaps the theory of CRS, deriving the expressions for CARS and SRS signals; Section 3 briefly summarizes the current status of single-frequency CRS techniques, both in terms of instrumentation and results; Sections 4 and 5 review the different experimental configurations used for broadband CARS and SRS, respectively; finally, Section 6 proposes a comparative analysis and discusses future developments.

2. Theory of coherent Raman scattering

In general, a CRS process can be described as a four-wave mixing interaction mediated by the third-order nonlinear susceptibility of the medium. [36] The mixing involves four fields at frequencies ω_i, where i=1...4, satisfying the condition $\omega_1 - \omega_2 + \omega_3 = \omega_4$ set by energy conservation. Without loss of generality, the nonlinear signal can be thought as generated at frequency ω_4 according to the equation: [37]

$$\frac{\partial E_4}{\partial z} = -i\alpha_4 P_4^{(3)}\exp(i\Delta k\, z) \tag{1}$$

where z is the propagation direction, $P_4^{(3)} = \varepsilon_0 \chi^{(3)} E_1 E_2^* E_3$ is the third-order nonlinear polarization, $\Delta k = k_1 - k_2 + k_3 - k_4$ is the wave-vector mismatch and $\alpha_4 = \frac{3\omega_4}{4cn_4}$ is a proportionality constant, c being the speed of light in vacuum and n_4 the refractive index of the medium at frequency ω_4. The nonlinear susceptibility $\chi^{(3)}$ of the sample can be decomposed in two terms according to the equation:

$$\chi^{(3)} = \chi_{NR}^{(3)} + \chi_R^{(3)} = \chi_{NR}^{(3)} + Re\left[\chi_R^{(3)}\right] + iIm\left[\chi_R^{(3)}\right], \tag{2}$$

where $\chi_R^{(3)}$ is the resonant nonlinear susceptibility given by the molecules under study and $\chi_{NR}^{(3)}$ is the non-resonant nonlinear susceptibility generated both by the same molecules and by the surrounding medium (through the process shown in Figure 2 (c)). $\chi_{NR}^{(3)}$ is also known as the non-resonant background (NRB). Note that, while $\chi_{NR}^{(3)}$ can be approximated to be real and frequency independent, $\chi_R^{(3)}$ is the superposition of several complex Lorentzian responses related to the different vibrational transitions of the molecules:

$$\chi_R^{(3)}(\omega) = \sum_i \frac{N_i\,\sigma_i}{\omega - \Omega_i - i\Gamma_i}, \tag{3}$$

where N_i is the concentration of Raman active scatterers, σ_i is the cross section, Ω_i the resonance frequency and Γ_i the line-width of the vibrational transition.

Let us first consider the CARS process. In this case we have $\omega_1 = \omega_{pu}$, $\omega_2 = \omega_S$, $\omega_3 = \omega_{pr}$, $\omega_4 = \omega_{aS} = \omega_{pu} + \omega_{pr} - \omega_S$ and the wave-vector mismatch is $\Delta k = k_{pu} + k_{pr} - k_s - k_{aS}$. This is the most general case where the vibrational coherence created by the pump and Stokes fields is read out by a probe field at frequency $\omega_{pr} \neq \omega_{pu}$, giving rise to the so-called three-color or non-degenerate CARS process; [38] however, since in most implementations pump and probe pulses are provided by the same pulse train and are frequency degenerate, we will hereafter set $\omega_{pr} = \omega_{pu}$ (two-color or degenerate CARS) and $\omega_{aS} = 2\omega_{pu} - \omega_S$. In a microscopy configuration, due to the short interaction length, one can neglect the phase mismatch between the interacting fields ($\Delta kL \cong 0$). In this case, by solving Equation (1) under phase-matched conditions, the nonlinear signal becomes:

$$E_{aS} = -i\alpha_{aS}\chi^{(3)}E_{pu}^2 E_S^* L, \tag{4}$$

where L is the nonlinear interaction length within the Raman-active medium. Since the CARS field is at a different frequency with respect to pump and Stokes, it can be easily measured in a background-free manner by directly detecting its intensity (homodyne detection):

$$I_{CARS}(\omega_{pu} - \omega_S) \propto |E_{aS}|^2 \propto |\chi^{(3)}|^2 I_{pu}^2 I_S L^2 =$$

$$= \left[\left|\chi_R^{(3)}(\omega_{pu} - \omega_S)\right|^2 + \chi_{NR}^{(3)2} + 2\chi_{NR}^{(3)}Re\left[\chi_R^{(3)}(\omega_{pu} - \omega_S)\right]\right] I_{pu}^2 I_S L^2, \tag{5}$$

where I_{pu} (I_S) is the pump (Stokes) intensity. Equation 5 shows that the NRB affects considerably the CARS response, since it is responsible for a constant, frequency-independent term ($\chi_{NR}^{(3)2}$) and for a dispersive interference term $2\chi_{NR}^{(3)}Re\left[\chi_R^{(3)}(\omega_{pu} - \omega_S)\right]$ that distorts the Lorentzian-shaped vibrational lines characteristic of SR. This effect is exemplified in **Figure 5**, where the CARS signal is calculated for different contributions of the NRB. In the case where $\chi_{NR}^{(3)}$ dominates over the resonant response, the lineshape of the vibrational feature is heavily distorted and assumes a dispersive-like behavior due to the increasing contribution from the

real part of $\chi_R^{(3)}$. Since NRB may derive from any molecule in the focal volume, its contribution easily becomes relevant for biological samples.
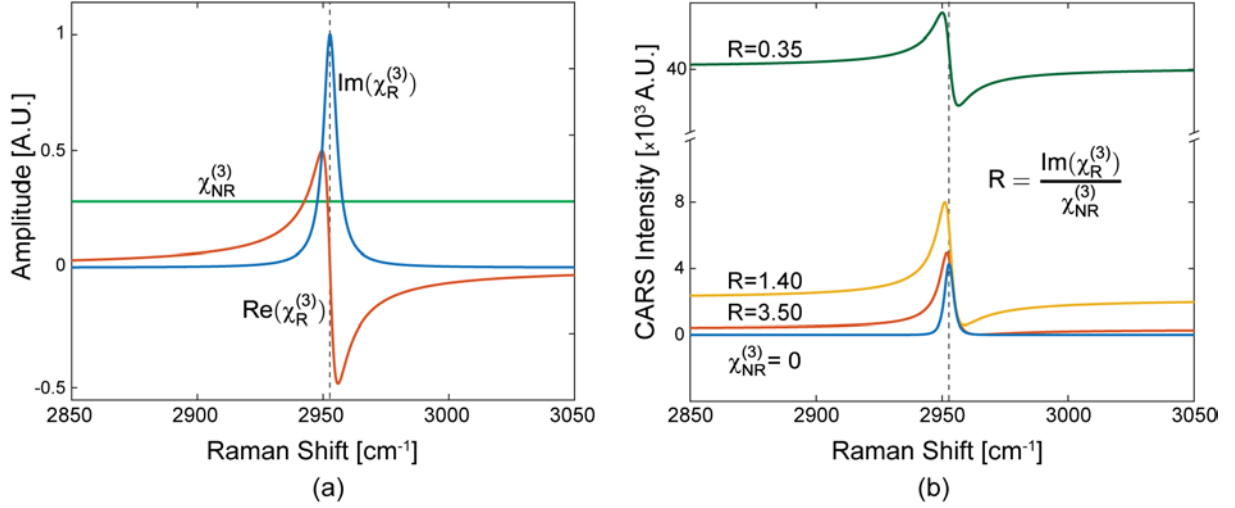

Figure 5 (a) Real and imaginary parts of the resonant third-order susceptibility $\chi_R^{(3)}$ for a vibrational transition centered at 2953 cm^{-1} ; (b) effect of the NRB on the corresponding CARS lineshapes.

This is especially problematic in the case of single-frequency CARS, because it becomes difficult to discriminate whether the measured signal comes from the targeted molecular species or from the background, and the image contrast is thus severely degraded. On the other hand, for the case of broadband detection, the CARS signal in the $\chi_{NR}^{(3)} \gg \chi_R^{(3)}$ limit becomes

$$I_{CARS}(\omega_{pu} - \omega_S) \propto \left[\chi_{NR}^{(3)2} + 2\chi_{NR}^{(3)} Re\left[\chi_R^{(3)}(\omega_{pu} - \omega_S) \right] \right] I_{pu}^2 I_S L^2. \tag{6}$$

This expression shows that the resonant signal is multiplied by the NRB, which is phase coherent with the CARS signal and may then act as a local oscillator (LO) providing its heterodyne amplification. The resonant contribution can in such a case be recovered from the measured CARS spectrum using proper retrieval algorithms, as described in Section 4. In this regime, the retrieved signal scales linearly with $\chi_R^{(3)}$ and thus with the concentration of the probed species.

On the other hand, in the regime when the NRB is negligible ($\chi_{NR}^{(3)} \ll \chi_R^{(3)}$), as for example in the C-H stretching region with its high density of oscillators, the CARS signal becomes:

$$I_{CARS}(\omega_{pu} - \omega_S) \approx \left| \chi_R^{(3)}(\omega_{pu} - \omega_S) \right|^2 I_p^2 I_S L^2 \propto N^2, \tag{7}$$

Here the spectral response preserves a bell-shaped peak centered at Ω , which facilitates species identification even in the single-frequency regime. As a drawback, the CARS signal here scales quadratically with the concentration of oscillators N , thus complicating a quantitative determination of the species concentration and preventing the measurement of highly diluted species. It is worth observing that in a broadband configuration where the Stokes pulses typically extend over hundreds of wavenumbers with a given spectral shape, the CARS and SRS signals must be properly normalized against the Stokes power density for a quantitative evaluation.

In SRS, on the other hand, we have $\omega_1 = \omega_2 = \omega_{pu}$, $\omega_3 = \omega_4 = \omega_S$ and the process is intrinsically phase matched ($\Delta k = 0$). In the weak signal limit, the nonlinear Stokes signal (a similar expression can be derived for the nonlinear pump signal) at the sample output, upon integration of Equation (1), can be written as:

$$\Delta E_S = -i\alpha_s\chi^{(3)}\left|E_{pu}\right|^2 E_S L, \tag{8}$$

Since ΔE_S sits on top of the very large Stokes signal E_S and thus can't be spectrally separated from it, its extraction needs the application of a high-frequency modulation transfer technique from the pump beam. Assuming $|\Delta E_S| \ll E_S$ the measured SRS signal thus becomes:

$$\Delta I_{SRS}\left(\omega_{pu} - \omega_S\right) \propto |E_S + \Delta E_S|^2 - |E_S|^2 \cong 2E_S Re[\Delta E_S] \propto \alpha_S Im\left[\chi_R^{(3)}\left(\omega_{pu} - \omega_S\right)\right]I_p I_S L, \tag{9}$$

which is proportional to the imaginary part of the Lorentzian-shaped nonlinear susceptibility, without any spurious contribution from the NRB, which is effectively suppressed being a real quantity. In addition, the SRS signal is directly proportional to $\chi^{(3)}$, so that it scales linearly with the sample concentration, allowing for an easier quantification of the species concentrations. Interestingly, the small nonlinear signal ΔE_S, which is of the same order as E_{aS}, is multiplied by the large and phase-locked Stokes field E_S (self-heterodyning configuration) acting as a LO and allowing for a large amplification of the SRS signal ($\approx 2E_S\Delta E_S$) with respect

to CARS ($\approx E_{aS}^2$). Such an advantage does not automatically translate into a better SNR (for a detailed discussion see, e.g., [39]), as the SRS signal suffers from the strong linear background given by the Stokes beam. The SRG signal can then be calculated as:

$$SRG(\omega_{pu} - \omega_S) \propto \frac{|E_S + \Delta E_S|^2 - |E_S|^2}{|E_S|^2} \propto \alpha_S Im\left[\chi_R^{(3)}(\omega_{pu} - \omega_S)\right]I_{pu}L. \qquad (10)$$

A similar expression holds for SRL, with I_{pu} replaced by I_S. As a consequence of Equation 10, the highest SRS signal, and thus the best SNR, is obtained by measuring SRG if $I_{pu} \gg I_S$, and SRL if $I_{pu} \ll I_S$.

By comparing CARS and SRS, a rather delicate balance of advantages and drawbacks emerges. CARS has the important advantage of being virtually a background-free process, since the emitted signal has a frequency ω_{aS} differing from those of pump and Stokes. On the other hand, it suffers from the NRB, generated both by the molecular species under study and by the surrounding medium, which does not carry any chemically specific information and, when the concentrations of the target molecules are low, can distort and even overwhelm the resonant signal of interest. In addition, even in the case where the NRB is negligible, due to the homodyne detection the CARS signal scales as the square of the number of oscillators in the focal volume, so that its sensitivity rapidly degrades with decreasing concentration, making it difficult to detect the less abundant biomolecules.

SRS can in principle overcome both limitations of CARS. Its signal is in fact proportional to the imaginary part of the third order susceptibility tensor, $Im(\chi^{(3)})$; since $\chi_{NR}^{(3)}$ is a real quantity, SRS is inherently free from NRB, and measures exclusively the imaginary part of the resonant vibrational response, $Im(\chi^{(3)})$, which has a bell-shaped Lorentzian response similar to SR and provides the sought chemical contrast. While this is true in principle, in practice cross-phase-modulation [36], [40] between pump and Stokes pulses or two-photon absorption [41] can provide artefacts in the SRS signal which are not dependent on the chemical

species. Furthermore, SRS scales linearly with the concentration N, thus allowing the quantitative detection of weakly concentrated species. On the other hand, SRS requires the detection of a small differential transmission signal (SRG or SRL, in practical cases of the order of $10^{-5} \div 10^{-4}$) sitting on the large (and noisy) background given by the Stokes (or the pump) light. The extraction of such a low signal level with a sufficiently high SNR, even when integration times are as short as a few microseconds, is required in order to operate the SRS microscope at high imaging speed: this indeed calls for the use of sophisticated techniques, involving high-speed modulation and lock-in detection, in order to circumvent the typically large laser intensity noise that occurs at low Fourier frequencies and achieve shot-noise limited performance.

In summary, there is not yet a clear winner between CARS and SRS for high-speed vibrational imaging, and the choice of the technique sensitively depends on the problem under study and the available instrumentation. For these reasons, both techniques will be treated on equal footing in the remainder of this Review.

3. Single-frequency CRS microscopy

To set the stage for the main topic of this Review, namely broadband CRS techniques, this paragraph briefly summarizes the state of the art of single-frequency CRS microscopy, both in terms of instrumentation and main results. The most challenging part of a single-frequency CARS/SRS microscope is the excitation source, which has to generate two synchronized laser pulses, the pump and the Stokes, with the following characteristics:

(i)   frequency detuning continuously variable between ∼500 and ∼3500 cm^{-1}, in order to cover all relevant vibrational transitions. This implies that at least one of the pump/Stokes pulses is broadly tunable. For example, assuming a fixed pump wavelength of 800 nm,

the Stokes must be tunable between 835 nm ($\Omega = 500$ cm^{-1}) and 1110 nm ($\Omega = 3500$ cm^{-1});

(ii)   pulse duration of 1-2 ps, corresponding to a bandwidth of ≈ 10-cm^{-1} for transform-limited (TL) pulses, in such a way to match the typical linewidths of vibrational transitions in the condensed phase. This choice optimizes the trade-off between peak power, which enhances the nonlinear CRS signal, and spectral resolution, which is prerequisite for chemical selectivity;

(iii)   NIR wavelengths, from 700 to 1200 nm to minimize photodamage, which is typically due to multiphoton absorption, and increase tissue penetration;

(iv)   high pulse repetition rates, of the order of 10-100 MHz, to maximize the acquisition speed while minimizing the pixel dwell time;

(v)   optical power >100 mW per branch, which is required to compensate for the losses of the optical chain of the microscope while attaining the maximum average power level permitted by biological samples, i.e. 10 – 20 mW at 700 nm and up to 100 mW at 1000 nm.

This combination of characteristics is challenging to be obtained, making CRS microscopy technically more demanding than other nonlinear microscopy techniques, such as two-photon excited fluorescence [19] and second-harmonic generation (SHG) microscopy, [42] that require a single excitation beam. The first CARS microscopy experiments employed two independent electronically synchronized picosecond Ti:sapphire oscillators, resulting in a very bulky and complex system. [43] This was soon superseded by the current "gold standard" in single-frequency CRS microscopy, which consists of a picosecond Nd:YVO$_4$ oscillator synchronously pumping an optical parametric oscillator (OPO). [44] The complexity of such laser system has motivated an intense research effort aimed at drastically reducing footprint and price while increasing reliability, mostly through fiber-format architectures. One class of systems is based

WILEY-VCH

on femtosecond Er:fiber oscillators at 1550 nm, seeding a pair of Er-doped fiber amplifiers (EDFAs), one of them followed by a highly nonlinear fiber (HNFs) for the generation of an octave-spanning continuum from ∼1000 to ∼2200 nm: this enables the synthesis, via frequency doubling and spectral compression of the two pulse trains in a thick SHG crystal, of picosecond fixed frequency pump pulses at ∼775 nm and of tunable picosecond Stokes pulses in the 850-1080 nm range. [45]-[48] This configuration has been recently upgraded by boosting the power of the Stokes arm via Yb:fiber [49] or Tm:fiber [50] amplification. Alternative schemes rely on the combination of a picosecond Yb:fiber oscillator with a fiber-based third-order optical parametric amplifier (OPA) or OPO [51]-[55] or on a high power femtosecond Yb oscillator directly pumping an OPA. [56],[57]

Single-frequency CARS and SRS are conceptually very similar and switching from one technique to the other requires only minor modifications of the optical excitation path and the detection chain. However, an extra requisite on the laser sources of the SRS technique is the low intensity noise at high frequencies, which is required to detect small differential signals. **Figure 6** shows the experimental setup of a CARS/SRS microscope for the case of detection in transmission, typically used for cells or thin tissue slices; for the case of backward (or epi) detection, [58] used for thick tissues, only one objective is employed and the signal is detected via a beam splitter. Pump and Stokes pulses are synchronized by a delay line, collinearly combined by a dichroic mirror (DM), focused on the sample by a microscope objective after going through a scanning unit, and the transmitted light is collimated by a similar objective. For the case of CARS, a sequence of short-pass and notch filters select the anti-Stokes light, which is measured with a photomultiplier. For the case of SRS, a high frequency modulator is inserted on the pump beam (for the case of SRG detection) or on the Stokes beam (for the case of SRL detection) and the Stokes (pump), selected by a sequence of long-pass (short-pass) and notch filters, is sent to a photodiode and to a lock-in amplifier, which synchronously demodulates it

and measures the SRG (SRL). In principle, given the similarity of the configurations, CARS and SRS signals can be detected on the same experimental setup or even simultaneously.
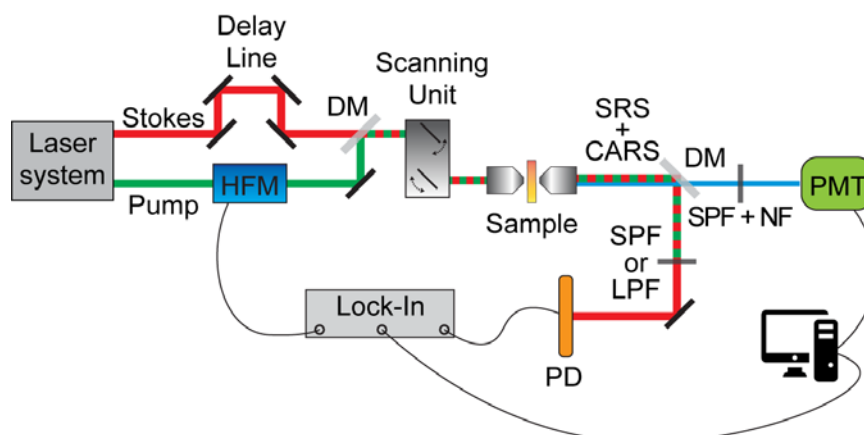

Figure 6 Schematic setup of a CARS/SRS microscope. HFM: high-frequency modulator (not necessary for CARS); DM: dichroic mirror; SPF: short-pass filter; LPF: long-pass filter; NF: notch filter; PMT: Photomultiplier Tube; PD: Photodiode.

As discussed in Section 2, the main problem of single-frequency CARS microscopy is the presence of the NRB, which may distort or even overwhelm the resonant contribution. Single-frequency CARS microscopy works very well in the C-H stretching region where, due to the high density of oscillators, the resonant contribution dominates over the non-resonant terms, and is therefore suitable, e.g. for imaging the distribution of lipids [59] and studying their metabolism. [60] [61] For the fingerprint region, the overwhelming contribution of the NRB makes it difficult to obtain a sufficient chemical contrast and to extract quantitative species concentrations. Many efforts have been devoted to the suppression of NRB, which however significantly increase the experimental complexity. Frequency-modulation CARS (FM-CARS) requires the generation of a second Stokes (pump) field at a slightly different frequency, so as to modulate the difference $\omega_{pu} - \omega_S$ in and out of the vibrational resonance. [62], [63] The NRB, which is independent of frequency detuning, does not contribute to the detected modulated signal and therefore is efficiently suppressed. Alternatively, interferometric CARS (I-CARS) requires the generation of an intense field, acting as a LO, at the anti-Stokes frequency, phase-coherent with the CARS fields and thus interfering with it. [64]-[67] By

properly adjusting the phase of the LO with respect to that of the CARS signal, one can suppress the NRB and at the same time amplify the CARS signal. Despite the elegance of the approaches, both FM-CARS and I-CARS have been seldom adopted because of the additional complexity of their experimental setups.

SRS, on the other hand, is free from NRB, although as mentioned in Section 2 it may suffer from the interference of spurious nonlinear effects, such as cross-phase modulation and two-photon absorption, which can be suppressed with more sophisticated configurations. [68], [69] It is however technologically more demanding than CARS, since it requires the measurement of a tiny differential signal (SRG or SRL) sitting on top of a large (and noisy) background given by the Stokes (or pump) light. The extraction of this signal requires the use of sophisticated detection chains, involving high-speed modulation and synchronous demodulation with a high-frequency lock-in amplifier, to overcome laser fluctuations. Excess laser intensity noise can be cancelled using balanced detection schemes, [47] which split off a fraction of the probe beam before the sample and send it to a reference detector. Such noise suppression, however, turns out to be quite difficult in real microscopy applications, since the spatially dependent transmission and scattering of the sample strongly vary the intensity of the probe beam, bringing it out of balance with the reference beam. To compensate for these variations during image acquisition, several solutions have been used, including auto-balanced detectors [49] and collinear [70] or in-line [71] balanced detection configurations.

In the following we briefly summarize some important experimental results achieved in label-free imaging with single-frequency CARS/SRS. The CARS technique was mainly used to study lipid distribution and their metabolism, due to the very high density of C-H oscillators intrinsic of these long-chain hydrocarbons, which give a resonant signal dominating over the NRB. In a pioneering study, [59] Hellerer *et al.* showed the capability of CARS to image lipid distribution

in the model organism *Caenorhabditis (C.) elegans* and to monitor the impact of genetic modifications on metabolic pathways leading to lipid storage, as shown in **Figure 7**.
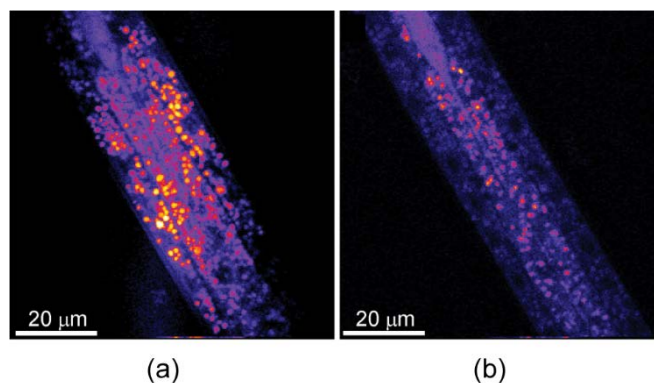

Figure 7 CARS microscopy of lipid storage in *C. elegans*. (a) Autoscaled CARS and (b) two-photon fluorescence images (80 × 80 μm^2, 20-s integration time) of a Nile red-stained daf-4 mutant of *C. elegans* arrested in its dauer stage for 3 weeks. The pharynx can be distinguished in the upper left corner. While the CARS image shows the full distribution of lipid droplets, also the hypodermal collection, the two-photon fluorescence image (excitation at 1064 nm) merely shows the lipid droplets in the intestine. Adapted from [59].

Lipid metabolism was studied also in human liver cells by monitoring the size and distribution of lipid droplets, and allowed to assess the effect of therapeutic drugs on specific pathologies with metabolic pathways leading to lipid accumulation. [72] CARS microscopy was also used to image the lipid-rich myelin sheat that coats the nerve axons and to image demyelination processes that characterize neurodegenerative diseases. [73]-[76]

Single-frequency SRS microscopy has found even broader applications in imaging thanks to its greatly reduced NRB. SRS has proven the capability to differentiate between nucleic acids, proteins and lipids, thanks to their different spectral response in the C-H stretching band, and to map their spatial distribution within living cells [77] (see **Figure 8**).

SRS microscopy has been used to image the dynamic uptake and the intracellular distribution of low-molecular-weight drugs within cells, as recently demonstrated by Fu *et al.* for tyrosin kinase inhibitors. [78] SRS microscopy has also found applications in clinical diagnostics: it has been used to identify squamous cell carcinoma in human skin, by monitoring the protein density and distinguishing the cell nucleus from the cytoplasm, obtaining images whose contrast closely resembles that obtained with classical histopathology. [79] SRS microscopy

has also been exploited for tumor identification, as a faster and potentially more accurate solution than the standard hematoxylin and eosin (H&E) staining: to this purpose, the typical two-colour contrast given by the H&E procedure has been reproduced by tuning the excitation to the CH_2 vibrations of lipids (2845 cm^{-1}) and to the CH_3 vibrations of proteins (2930 cm^{-1}). This "virtual histopathology" approach could potentially avoid artefacts derived from imaging frozen or fixed tissues; it has been used to detect tumor margins in the live brain of a mouse with a xenografted tumor (human glioblastoma multiforme) [80] as well as to accurately reveal tumor infiltrations in freshly excised unprocessed specimens from neurosurgical patients. [81] Recently, using a portable fiber-based SRS microscope in the operating room, a campaign of measurements has been performed on neurosurgical patients, demonstrating a very good agreement of the virtual histopathology with H&E staining. [82], [83]
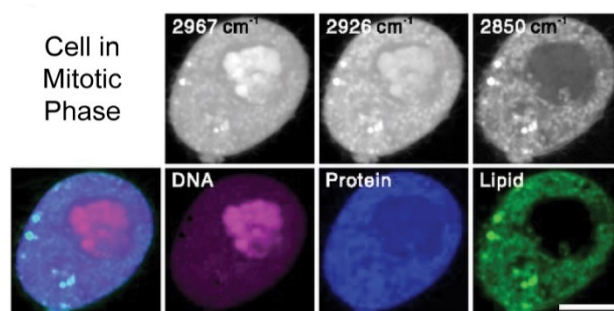

Figure 8 SRS images of a live cell in mitotic phase (prophase) at 2,967, 2,926, and 2,850 cm^{-1}, respectively, and the decomposed distribution of DNA, protein, lipids, and the overlay. Chromosomes were visualized with both high contrast and high signal-to-noise ratio. Adapted from [77].

4. Broadband CARS techniques.

In this Section we review the different techniques employed to measure the CARS spectrum, or at least one portion of it (typically either the C-H stretching or the fingerprint region) for every pixel of the image. We start with hyperspectral CARS approaches which target a single vibrational frequency at a time and obtain the full spectrum by several sequential measurements at several pump-Stokes frequency detunings (Section 4.1); we then discuss multiplex CARS approaches, which combine a narrowband pump and a broadband Stokes pulse, and detect the full CARS spectrum with a spectrometer (Section 4.2); following that we describe time-resolved

CARS, a variant of multiplex CARS which introduces a time delay between excitation and probe pulses in order to efficiently suppress the NRB (Section 4.3); we continue with single-beam CARS, which uses a single broadband pulse and pulse shaping techniques to achieve frequency resolution in the CARS spectrum (Section 4.4); finally we present FT CARS, which measures the CARS signal with a single detector in the time domain and achieves frequency resolution with a FT operation (Section 4.5).

4.1 Hyperspectral CARS

In the simplest configuration of hyperspectral CARS, a fixed narrowband pump and a tunable narrowband Stokes simultaneously excite a sample and the generated CARS signal is acquired sequentially by changing pump-Stokes frequency detuning, to construct the full CARS spectra for every pixel of the image. An elegant method to rapidly vary the frequency detuning is the spectral focusing (SF) technique, pioneered by Hellerer *et al.* [84]. SF enables one to measure hyperspectral CRS signals with high frequency resolution with the use of broadband femtosecond pump and Stokes pulses, both of which are temporally chirped. While a TL pulse has an instantaneous frequency which is equal to the carrier frequency across the whole pulse temporal profile, in a chirped pulse the phase term has a quadratic dependence on time, such that, within the temporal envelope of the pulse, the instantaneous frequency deviates from the carrier frequency in a linear fashion. This effect occurs in any dispersive medium, as group velocity dispersion (GVD) causes the frequency components of a femtosecond pulse to split apart over time, leading to a time-dependent instantaneous frequency and to a pulse lengthening, up to several picoseconds. In this case, the electric field of the chirped pulse, assuming a Gaussian temporal profile, can be written as:

$$E(t) = E_0 exp\left[-\left(\frac{t^2}{2\tau_p^2} + i\alpha t^2\right)\right],$$ (11)

where α is the so-called chirp parameter. Considering two femtosecond pulses with carrier frequencies ω_{pu} and ω_S, both equally chirped with the same parameter α, it turns out that their instantaneous frequency difference (IFD) is constant, and can be varied adjusting the mutual delay Δt between the two pulses

$$IFD(\Delta t) = \omega_{pu} - \omega_S + 2\alpha\Delta t, \tag{12}$$

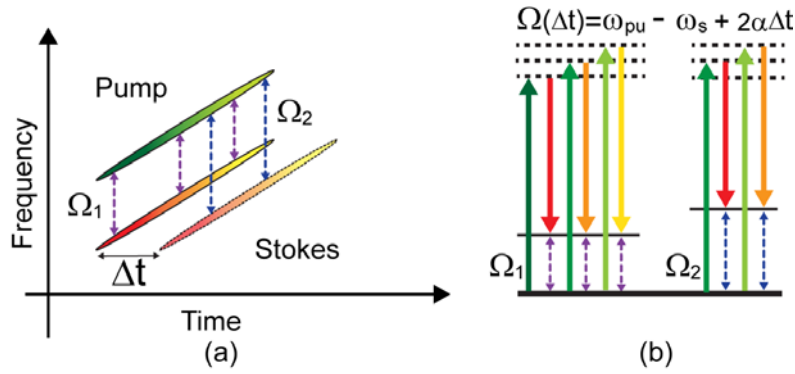as illustrated in Figure 9 (a).

Figure 9 (a) Concept of spectral focusing, showing the time-dependent frequencies of pump and Stokes pulses; (b) level excitation scheme.

This configuration can be exploited in a CRS experiment to excite a vibrational resonance whose energy matches the IFD. In this way, the whole frequency spectrum of the two broadband chirped pulses is "focused" in probing only a single vibrational transition, the one that matches the IFD. Despite the broadband nature of the pulses, thanks to the chirp, the effective spectral bandwidth $\Delta\nu_{eff}$ at which the vibrational modes are probed turns out to be narrower with respect to the pulses bandwidth $\Delta\nu$, [85]

$$\Delta\nu_{eff} = \frac{\Delta\nu}{\sqrt{1+\alpha^2}}, \tag{13}$$

assuming pulses with the same spectral width $\Delta\nu$ and same chirp parameter α. By scanning the delay between pump and Stokes pulses while still maintaining their temporal overlap, it is possible to select and probe a different vibrational resonance, as sketched in Figure 9.

SF has been used for CARS microscopy and spectroscopy. [84]-[86] The setup is similar to the one used for single-colour measurements, except for the pulses involved, and for the optical

systems used to introduce the chirp. The commonly used laser sources for SF-CARS, typically a Ti:sapphire laser pumping either an OPA, an OPO, or a photonic crystal fiber (PCF) for spectral broadening, provide two synchronized femtosecond pulses, around 100 fs long, that are then stretched up to 1 – 10 ps after the chirping stage. The chirping in general can be implemented by means of pulse stretchers consisting of a double-pass grating-lens combination, which allows fine tuning of the chirp parameter by adjusting the distance between lenses and grating. Another typically adopted solution is the use of blocks of highly dispersive glass (such as SF57 or SF6) whose length is selected according to the desired chirp parameter at the pump and Stokes wavelengths. Calculations can be done through Sellmeier equations, which express the refractive index as a function of the wavelength. The delay between pulses is adjusted through mechanical delay lines after recording a calibration curve using a known Raman spectra as a reference. Hellerer *et al.* [84] have utilized 70 fs, 683 nm pulses as the pump obtained by frequency doubling the output of an OPA which was pumped by a regeratively amplified fs laser system, while a 5% fraction of 170 fs, 798 nm output of the same regenerative amplifier served as Stokes. SF was implemented using double-pass grating-lens strechers and led to a spectral resolution of ~8 cm^{-1}, quite comparable to that obtained with ps TL pulses. In another setup, Rocha-Mendoza *et al.* [85] employed a Ti:sapphire laser pumping an OPO with intracavity frequency doubling, where the Ti:sapphire laser and of the OPO output served as Stokes centered at 832 nm and the tunable (650-700nm) pump respectively. Pump and Stokes pulses were chirped for SF by propagation in appropriate lengths of SF57 glass-blocks. A Ti:sapphire laser pumping a PCF for spectral broadening was used by Pegoraro *et al.* [86], Slepkov *et al.* [87] and Mostaço-Guidolin *et al.* [88] to synthesize pump-Stokes pulses chirped in SF6 glass blocks with appropriate thickness. In an important development, Langbein *et al.* [89] have shown that hyperspectral SF-CARS microscopy can be implemented using a single broadband sub-10-fs Ti:sapphire oscillator. A dichroic mirror split the laser output into the pump and the Stokes pulses. To impart an equal

linear chirp to the two pulses, an extra GVD was added to the Stokes pulse through an SF57 glass block before it was recombined on a second dichroic mirror with the pump with an adjustable delay. After that both pulses propagated through another SF57 glass block before entering the microscope. This configuration was later adopted in many experiments. [90]-[93] The major benefit of using a single sub-10fs Ti:sapphire laser over a PCF pumped by Ti:sapphire is the flat and stable spectral phase and high output power. Chen *et al.* [94] have demonstrated hyperspectral frequency-modulation (FM) CARS in the fringerprint region using SF, employing a single sub-10-fs Ti:sapphire laser. For FM-CARS, a Pockels cell was inserted in the pump branch to switch the polarization direction of the input pump pulses at 100-kHz frequency. The two polarization directions were then separated by a polarizing beam splitter and they were sent back to the Pockels cell again to recover their original polarization states after retro-reflecting them separately by two flat mirrors. In this way, the on-off state of the Pockels cell determined the path length of the pump pulses and the corresponding frequency detuning of the SF. Finally, the NRB-free FM-CARS spectrum was acquired by scanning the delay of the Stokes on a photomultiplier read through a lock-in referenced to the Pockels cell signal.

4.2 Multiplex CARS

The first multiplex CARS setup was reported by Müller and Schins [95] and by Cheng *et al.* [96] Both studies used two electronically synchronized Ti:sapphire lasers, a narrowband pump (10 ps, 1.5 cm^{-1}) and a broadband Stokes (80 fs, 180 cm^{-1}) and detected the CARS signal in the forward direction with a spectrometer followed by a CCD.

In these early studies only a limited bandwidth of ≈200 cm^{-1} in the C-H stretching region was covered, with acquisition times on the order of a fraction of a second. An upgraded multiplex CARS system with thousands of cm^{-1} spectral coverage was soon reported by Kee and Cicerone [97] and by Kano and Hamaguchi, [98], [99] then followed by Motzkus and coworkers. [100]-

[102] The experimental setup, which is schematized in **Figure 10** (a), is similar for all cases. It starts from a femtosecond Ti:sapphire oscillator split into two beams. One beam is bandpass-filtered to ≈13 cm^{-1}, corresponding to 1.2 ps duration, and acts as the pump; the second beam undergoes spectral broadening in a nonlinear fiber, either a tapered fiber [97] or a PCF, [98] in such a way that the red-shifted part of it serves as a Stokes beam (Figure 10 (a)).
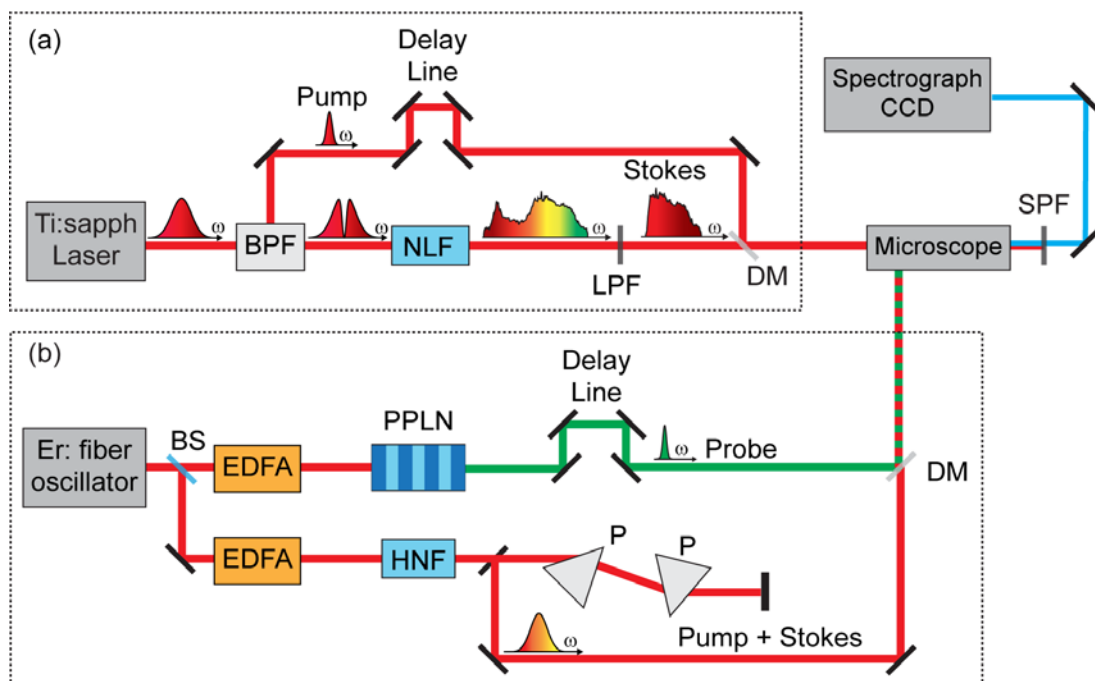
Figure 10 (a) Ti:sapphire-based broadband CARS setup. NLF: nonlinear fiber; BPF: reflective bandpass filter; LPF: longpass filter; DM: dichroich mirror; SPF: shortpass filter. (b): Er:fiber-based CARS setup. EDFA: Erbium doped fiber amplifier; HNF: highly nonlinear fiber; PPLN: periodically poled lithium niobate crystal; P: prisms for pulse compression.

Pump and Stokes are collinearly combined and focused on the sample and the CARS signal, after short-pass filtering, is detected via a spectrometer combined with a CCD. Multiplex CARS imaging was achieved, with typical pixel dwell times ranging from tens to hundreds of milliseconds, thus too slow for biomedical applications. In multiplex CARS the resonant signal is mixed with the NRB, which distorts the lineshapes with respect to those measured in SR. This distortion is particularly relevant in the fingerprint region, where the resonant contribution is weak. Under these conditions, the NRB exceeds the resonant signal and distorts its shape, leading to dispersive features due to the real part of $\chi_R^{(3)}$. It was soon realized, however, that in the

broadband case the NRB is not as detrimental as in the single-frequency configuration. On the one hand, the NRB can act as a LO, intrinsically phase-locked to the nonlinear CARS signal, that allows its heterodyne amplification through the term $2\chi_{NR}^{(3)}Re\left[\chi_R^{(3)}\right]$. On the other hand, the availability of the complete CARS spectrum enables one to apply analytic techniques to retrieve the spectral phase (or equivalently, the real and imaginary part of the nonlinear susceptibility).
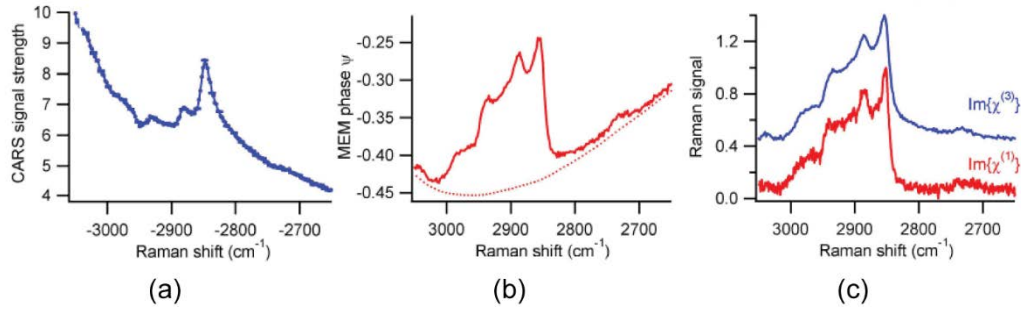

Figure 11 (a) CARS signal in the vicinity of vibrational resonances of a lipid (DMPC) sample; (b) corresponding MEM phase (solid line) and estimated background phase (dotted line); (c) Raman line-shapes obtained from CARS spectrum (blue line) and the corresponding SR spectrum (red line). Adapted from [104].

The first technique used to this purpose was the maximum entropy method (MEM) introduced by Vartiainien *et al.*, [103], [104] which does not require any *a priori* knowledge about the vibrational bands (positions, linewidths and amplitudes) contained in the spectrum. The idea of the MEM method is to express the complex nonlinear response as:

$$X^{(3)}(\omega) = \chi_{NR}^{(3)} + Re\left[\chi_R^{(3)}(\omega)\right] + iIm\left[\chi_R^{(3)}(\omega)\right] = |\chi^{(3)}(\omega)|\,exp(i\theta(\omega)), \qquad (14)$$

where $\omega = \omega_{pu} - \omega_S$. The MEM method extracts from the experimental data an estimated value of the phase, $\theta_{est}(\omega)$, by nonlinear polynomial fitting, and uses it to retrieve the imaginary part of the estimated resonant nonlinear susceptibility $\chi_{Rest}^{(3)}(\omega)$ which, considering the real nature of the NRB, can be expressed as:

$$Im\left[\chi_{Rest}^{(3)}(\omega)\right] \cong |\chi^{(3)}(\omega)|sin(\theta_{est}(\omega)) \qquad (15)$$

Figure 11 provides an example of application of the MEM to reconstruct the phase and the imaginary part of the nonlinear susceptibility.

Another phase retrieval technique, based on time-domain Kramers-Kronig (TDKK) transform including the causality condition, [105] was proposed by Cicerone *et al.*, allowing to work in the realistic condition of non-uniform spectral density of the broadband Stokes pulse, which leads to a not spectrally flat NRB. The MEM and TDKK approaches have been demonstrated to be functionally equivalent for multiplex CARS microscopy. [106]

In a parallel development, multiplex CARS has also been pursued starting from a nanosecond laser system. The experimental setup reported by Okuno *et al.* [107], [108] is remarkably simple: it starts from a passively Q-switched microchip Nd:YAG laser emitting 1064-nm pulses with 10-μJ energy, <1 cm^{-1} bandwidth and <1ns duration, at 33 kHz repetition rate. The laser output is divided by a beam splitter: one beam directly constitutes the pump for the CARS process, while the other one is launched in a 6-m-long air-silica PCF for supercontinuum (SC) generation. The PCF is designed to provide zero dispersion at wavelengths slightly shorter than 1064 nm, so that a broadband SC is generated as the result of modulation instability, soliton formation, soliton self-frequency-shift and soliton interaction. [109] The near-IR part of the SC is used as the Stokes pulse; it extends from 1.05 to 1.8 μm and thus fully covers the fingerprint and C-H stretching regions. The SC is collimated by a microscope objective and cleaned up with a series of filters to eliminate components at the anti-Stokes frequencies. Pump and Stokes pulse are collinearly recombined by a notch filter and focused on the sample; the transmitted CARS signal, after filtering, is detected by a spectrometer with a CCD camera. Since both pump and Stokes pulses have $\approx$ns duration, their synchronization is not critical and not affected by the chirp acquired by the Stokes pulse in the PCF. Further optimized versions of the microchip-based laser have been reported in. [110]-[112]

The multiplex CARS setup based on the sub-nanosecond microchip laser offers the advantages of low-cost, compactness and robustness. It has been used, in combination with the MEM method, to extract the fingerprint Raman spectra of living yeast cells and extract dynamical information.

WILEY-VCH

[113] On the other hand it also has some drawbacks: (i) the sub-nanosecond duration of the pump pulse is longer than the optimum value (2-5 ps) required to match vibrational linewidths in the condensed phase, so that for a given average power the peak power available and thus the CARS signal strength is lower; (ii) the microchip laser has low repetition rates of the order of tens of kHz; (iii) the SC generated by the PCF suffers from shot to shot instabilities, which require averaging over multiple laser shots. The combination of these factors leads to rather long pixel dwell times, of the order of tens to hundreds of milliseconds.
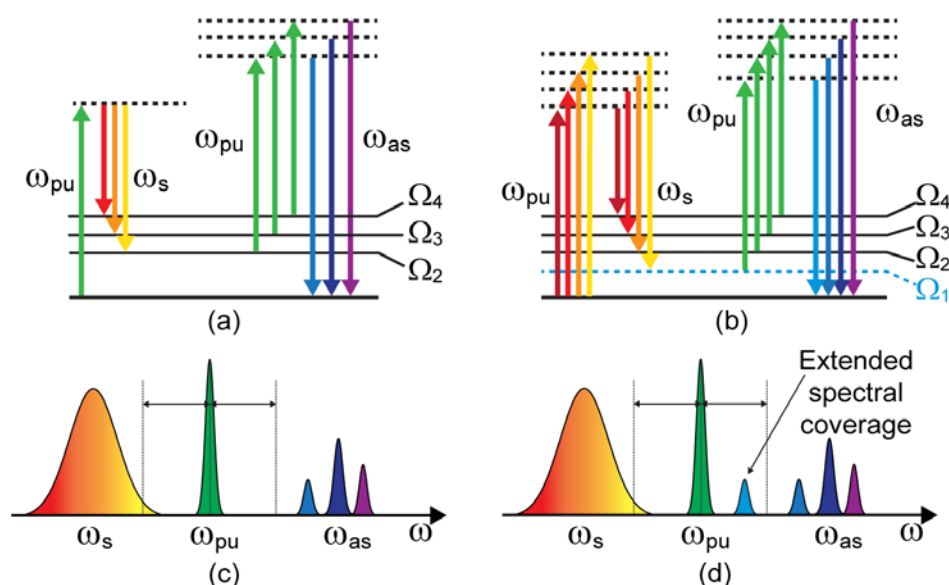

Figure 12 Different CARS excitation mechanisms used by Cicerone *et al.* [38]. (a,c) Two-colour mechanism. (b,d) Three-colour mechanism (ISRS).

The so far presented multiplex CARS systems work reasonably well in the C-H stretching band, with its high density of oscillators, but provide signals that are too weak in the critical fingerprint region. An important breakthrough has been recently achieved by the Cicerone group [38] using the laser system shown in Figure 10 (b). The system starts with a femtosecond Er:fiber laser oscillator followed by two EDFA arms, each generating synchronized pulse trains with 350-mW average power; [114] one arm is frequency doubled to generate narrowband pulses at 770 nm with flattop 3.8 ps temporal profile, while the other is spectrally broadened in a HNF to generate a SC spanning the 900-1350 nm wavelength region, which is compressed to a 16 fs duration by

29

a prism pair. This pulse combination allows to extract the CARS response by both the two-color and the three-color mechanism, as sketched in **Figure 12**.

In the two-color process, the narrowband pulse acts as pump and the broadband one as Stokes, enabling one to access the 2000-3500 cm^{-1} frequency range. In the three-colour mechanism, the broadband 16-fs pulse acts as both pump and Stokes (see Figure 12 (b)), generating the vibrational coherence by the so-called Impulsive Stimulated Raman Scattering (ISRS) mechanism. [115], [116] ISRS is a time-domain, single-pulse version of SRS, in which the different frequency components of a single broadband pulse simultaneously excite virtual levels and stimulate the emission down to vibrational levels of the ground state. The ISRS process creates a vibrational coherence in all modes with frequencies falling within the excitation laser bandwidth, provided that the pulse has a temporal duration close to the TL value, so that all frequencies interact nearly simultaneously with the sample. As a rule of thumb, one can say that ISRS is able to create a vibrational coherence at frequencies up to the reciprocal of the pulse duration, so that the 16-fs SC pulse can efficiently excite frequencies in the fingerprint region. This vibrational coherence is then read out by a further interaction with the narrowband 770-nm probe pulse, which generates the CARS signal. Here the probe pulse is deliberately synchronized with the SC pulse, to generate a strong NRB which acts as heterodyne amplifier of the nonlinear CARS signal (for methods of NRB reduction by delaying the probe pulse, see Section 4.2). This combination of efficient impulsive excitation and heterodyne amplification by the NRB enables to greatly enhance the weak fingerprint signal. The setup allows to retrieve Raman spectra in the whole biologically relevant frequency region (500-3500 cm^{-1}) with 10 cm^{-1} frequency resolution and 3.5 ms pixel dwell time. It was applied to three-dimensional imaging of murine liver tissue sections, reported in **Figure 13**, enabling the authors to differentiate proteins, collagen and DNA based on their chemical signatures in the fingerprint region, as well as to histopathology, by

identifying the tumor margins in a xenograft glioblastoma implanted in mouse brain. The results

by Cicerone *et al.* represent the current state of the art in multiplex CARS microscopy.

4.3 Time-resolved CARS

Time-resolved CARS (TR-CARS) is an elegant multiplex approach that allows one to

effectively remove the NRB. TR-CARS uses the pulse sequence depicted in **Figure 14** (a), in

which the probe pulse (ω_{pr}) that reads the vibrational coherence generated by the pump and

Stokes pulses is delayed by a time Δt with respect to the synchronized pump and Stokes pulses,

to avoid any temporal overlap with them. In this way the resonant nonlinear susceptibility $\chi_R^{(3)}$,

which corresponds to the vibrational coherence generated by the pump and Stokes pulses and

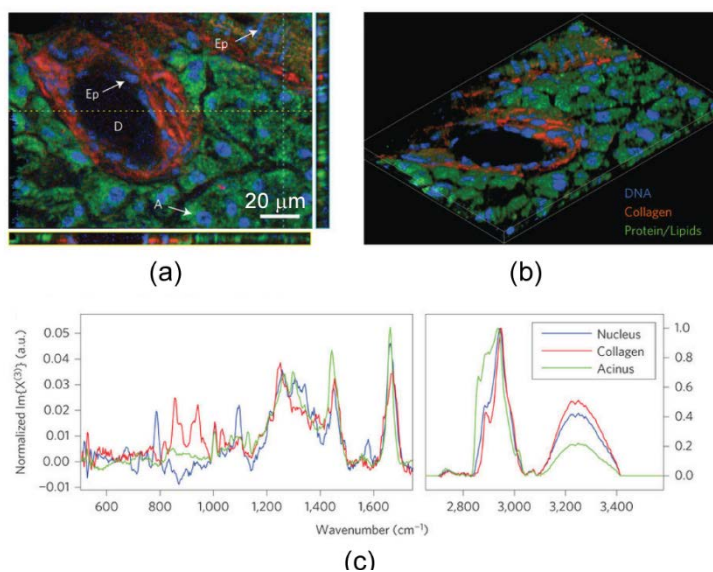which persists on the picosecond timescale that characterizes vibrational dephasing in

Figure 13 (a) Single pseudocolour multiplex CARS image of murine liver tissue obtained from a z-stack image collection: nuclei (785 cm⁻¹) highlighted in blue, collagen (855 cm⁻¹) in red and a composite of lipids and proteins in green (1,665 cm⁻¹). D, exocrine duct; A, acinar cell; Ep, epithelial cell. Two axial planes are also shown to provide histochemical depth information. (b) Three-dimensional reconstruction of pancreatic ducts from ten z-stack images. (c) Single-pixel multiplex CARS spectra taken from within an epithelial cell nucleus, within the fibrous collagen and from within the cytosol of an acinar cell. Adapted by permission from Macmillan Publishers Ltd: Nature Photonics [38], © (2014)

molecules, [117] is sampled by the probe pulse. On the other hand the NRB, which is generated

by the four-wave-mixing process $\omega_{aS} = \omega_{pu} - \omega_S + \omega_{pr}$, mediated by the instantaneous non-

resonant nonlinear susceptibility $\chi_{NR}^{(3)}$, is completely suppressed, since it would require the

temporal overlap of pump, Stokes and probe pulses. The price to be paid is that the time-delayed

probe pulse interacts with a vibrational coherence that has decayed with a dephasing time T_{2v}, leading to a reduction of the useful CARS signal by $e^{(-2\Delta t/T_{2v})}$, as depicted in Figure 14.
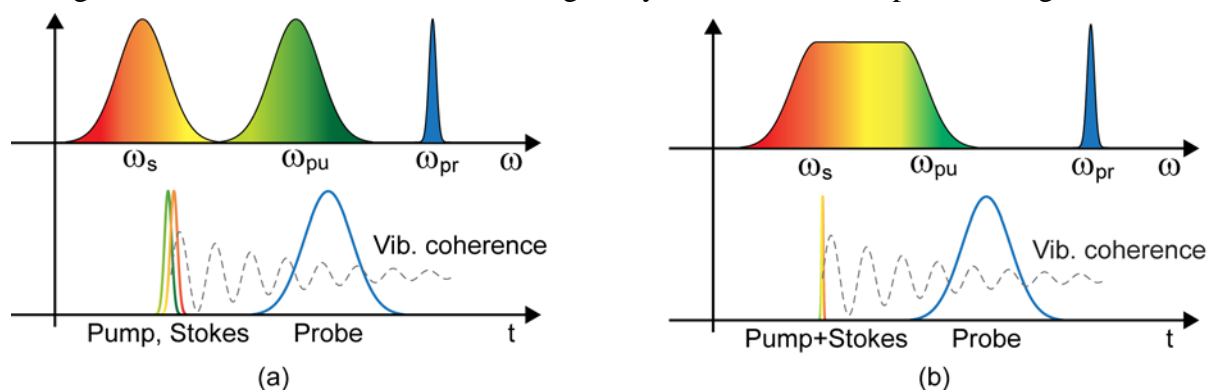

Figure 14 TR-CARS pulse sequence in the (a) three-colour configuration [120] and (b) two-colour configuration, with the vibrational coherence generated by ISRS. [121]

TR-CARS was first demonstrated in 1980 using a non-collinear interaction geometry in a two-colour configuration ($\omega_{pu} = \omega_{pr}$) [118] and exploiting phase-matching to select the interaction of interest. In a collinear geometry, suitable for microscopy, TR-CARS requires a three-colour configuration, to prevent spectral overlap of the useful CARS signal with the NRB generated by the two-colour process $\omega_{aS} = 2\omega_{pu} - \omega_S$. The generation of three independent synchronized pulses with different colors makes TR-CARS quite complicated and limits its practical applicability. Pestov *et al.* [119],[120] employed a three-pulse configuration with broadband pump and Stokes pulses, produced by a femtosecond Ti:sapphire laser (803 nm, 32 nm bandwidth, Stokes) driving an OPA (714-734 nm, pump), and a narrowband (580 nm, <1 nm bandwidth) probe pulse obtained by frequency filtering the output of a second OPA with a 4f pulse shaper. Using a delay of $\Delta t \approx 1.5$ ps and μJ-level energy per pulse, they were able to detect CARS spectra of sodium dipicolinate (NaDPA) molecules, which are markers for bacterial spores, with integration time of the order of 1 s.

An elegant scheme of TR-CARS, based on a compact fiber laser system, was introduced by Selm *et al.* [121] The system is similar to the one shown in Figure 10 (b): it starts from a mode-locked femtosecond Er:fiber laser at 40 MHz repetition rate, seeding two EDFAs, generating synchronized pulse trains with 350 mW average power. [122] One of them produces

in a properly designed HNF an octave-spanning continuum that features an ultra-broadband dispersive wave extending from 950 nm to 1450 nm. As this is broadband enough to contain both pump (ω_{pu}) and Stokes (ω_S) frequency components (see Figure 14 (b)), its temporal compression down to the TL duration (11.4-fs) allows excitation by ISRS of all vibrational modes, even beyond 3000 cm^{-1}. The second branch is focused on a 10-mm-long periodically poled lithium niobate (PPLN) crystal, generating 3-ps, 10 cm^{-1} pulses at 777 nm by SHG spectral compression. [123] Such narrowband pulses act as a probe (ω_{pr}) for the vibrational coherence generated by the broadband pulse, generating the CARS signal at the frequencies $\omega_{as} = \omega_{pr} + \Omega$. By delaying the narrowband with respect to the broadband pulse, one suppresses the NRB and recovers a clean vibrational spectrum, as demonstrated by measuring solvents and by imaging the lipid distribution in *C. Elegans*. It should be noted that the spectral compression technique generates pulses with sharp temporal leading edges, [123], [124] which are ideal for the TR-CARS technique, since they enable to effectively suppress the NRB without losing too much signal due to vibrational dephasing. On balance, while TR-CARS enables to elegantly suppress the NRB, it significantly reduces the useful signal, so that its advantages for imaging applications are not obvious.

4.4 Single-beam CARS

Single-beam CARS makes use of only one ultrashort laser pulse to generate the vibrational coherence and to read it out; the required frequency resolution is achieved by the use of coherent control techniques enabled by spectral pulse shaping. The main advantage of single-beam CARS is the simplicity of the excitation source, since it requires only a single broadband laser pulse at a fixed frequency, rather than synchronized multi-frequency pulses. On the other hand, it suffers from the complications inherent with pulse shaping. The pioneering experiment, performed in 2002 by Dudovich *et al.*, [125] starting from a 20-fs Ti:sapphire laser obtained a spectral

resolution of 30 cm^{-1}, which is a factor of 40 better than the pulse bandwidth. The broadband laser was coupled with a pulse shaper, based on a 4f configuration with a spatial light modulator (SLM) in the Fourier plane, [126] which served the dual purpose of controlling the spectral phase of the pulse and of filtering out the blue tail of the spectrum, at which the CARS signal is generated (**Figure 15** (a)).
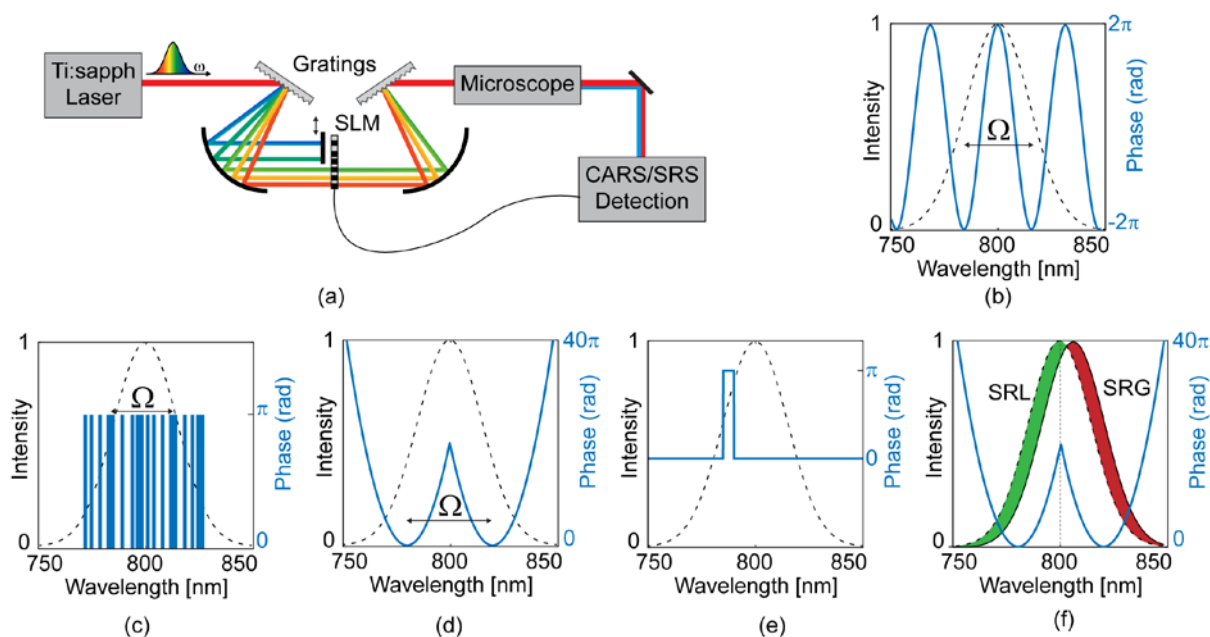

Figure 15 (a) Schematic of single-beam CRS setup employing spatial light modulator (SLM) at the Fourier plane of a grating based pulse shaper where a knife-edge is used to block the blue-tail of the spectrum coinciding the generated CARS signal. Illustration of pulse-shaping phase functions generated by SLM for selective vibrational excitation for CRS: (b) sinusoidal, (c) pseudorandom binary, (d) a pair of frequency-displaced parabolic and (e) 'π gate' phase functions. (f) Pulse-shaping scheme for SRS. Dashed lines are the input Gaussian spectrum envelop while solid Gaussian shape in (f) is output spectrum envelope.

The shaped pulse was sent to the sample and the emitted CARS signal was detected by a photomultiplier followed by a lock-in amplifier, measuring the difference of the signals alternately generated by the shaped pulse and the corresponding unshaped TL pulse. Upon broadband excitation, a given vibrational frequency Ω is populated by multiple pairs of pump and Stokes pulses, with frequency ω and $\omega - \Omega$, and the overall population of a specific level depends on the interference of such excitation pathways. For a TL pulse, constructive interference occurs for all values of Ω and the frequency resolution is lost. On the other hand, by applying a sinusoidal phase modulation of the kind $sin\left(2\pi \frac{\omega}{\Omega_m}\right)$ as shown in Figure 15 (b), one

achieves constructive interference when $\Omega = N\Omega_m$, with N an integer, and destructive interference for other frequencies. Note that this phase pattern corresponds to excitation of the sample with a sequence of pulses with period $\tau = 2\pi/\Omega_m = NT$ where T is the period of the vibration; coherent population of a vibrational level can thus only occur if the period of the pulse sequence is an integer multiple of the corresponding vibrational period. [127] By recording the CARS signal as a function of the period of the phase modulation function and performing a FT, one can then recover the CARS spectrum. A similar sinusoidal phase modulation setup was adopted for low wavenumber (50-400 cm^{-1}) CARS spectroscopy, [128] allowing one to access conformational modes which are important for biomolecules. It should be noted that a sinusoidal phase function excites unwillingly also the second harmonic frequency 2Ω of the desired mode. There are several choices other than the sinusoidal phase function for selectively exciting a single Raman mode of frequency Ω. Lozovoy *et al.* [129] have applied a pseudorandom binary spectral phase function (see Figure 14 (c)) to the SLM of the pulse shaper to achieve much cleaner coherent excitation of a Raman mode at Ω without a contribution at 2Ω; the binary phase pattern repeats twice within a range of Ω. An elegant and practical alternative [130][131] is to apply a pair of frequency-displaced parabolic spectral phase functions to the SLM as shown in Figure 15 (d), which create two time-delayed chirped pump and Stokes pulses, enabling selective coherent excitation of a Raman mode through the SF mechanism. In this case the relative displacement of the minima of the phase parabolas can be scanned to address different vibrational frequencies.

Single-beam CARS, working with a high intensity short pulse, presents the serious disadvantage that impulsive excitation of the instantaneous nonlinear electronic response generates a very large NRB, which distorts the resonant Raman contribution. As in multi-beam CARS, several techniques have been applied to single-beam CARS to minimize the NRB. These approaches exploit the capability of pulse shapers to provide independent and simultaneous control of phase, polarization and amplitude of the pulse frequencies. A first

approach in this direction was proposed by Oron *et al.* [132] for multiplex CARS spectroscopy and later adopted by Katz *et al.* [133] for stand-off backscattered CARS detection. In these experiments a 20-fs mode-locked Ti:sapphire pulse is shaped using an SLM to use the generated NRB as LO for heterodyne amplification of the resonant Raman contribution. The pulse shaper filters out the blue tail of the excitation spectrum, where the CARS signal is generated, and shifts the spectral phase in a narrow band of the pulse spectrum by π to generate a 'π phase gate' (see Figure 15 (e)). The shaped pulse spectrum can be thought as the superposition of a broadband spectrum $E_b(\omega)$, which consists of the pulse spectrum with a tiny hole in correspondence to the phase gate, and a narrowband spectrum $E_n(\omega)$, which is phase shifted by π. The narrowband spectrum generates the CARS signal, while the broadband spectrum, which is hardly affected by the pulse shaping, generates the NRB, which acts as LO and interferes with the CARS signal.

To address the problem of NRB, single-pulse polarization-resolved CARS has also been implemented in two slightly different configurations using a pair of SLMs in the Fourier plane of the shaper, allowing for both spectral phase and polarization shaping. In the configuration by Oron *et al.*, [134] later also adopted by Roy *et al.* [135] for single-beam CARS at higher wavenumbers and by Li *et al.* [136] for stand-off CARS detection, the polarization in a narrow portion on the high-frequency side of the broad excitation spectrum was rotated by pulse shaper from the x-axis to the orthogonal y-axis and the CARS signal was collected along the y polarization. This automatically eliminates all signal contributions which do not involve the narrowband y-component as probe/pump, thus providing frequency resolution. The broadband NRB is reduced by introducing a π phase gate (spectral phase shaping) at the center of the polarization shifted narrowband probe. This splits the probe pulse into two spectrally distinct longer duration probe pulses with opposite phases. Due to the instantaneous and equal non-resonant response, the NRBs generated from the two probes destructively interfere to

cancel each other. On the other hand, the π phase shift compensates for the phase change at resonance, leading to an enhanced resonant Raman signal over this narrow band. However, a small NRB leakage from the polarizer can still be observed.

The NRB can be completely eliminated using the interferometric single-pulse polarization resolved CARS configuration proposed by Lim *et al.* [137],[138] This setup utilizes the same polarization and spectral phase shaping adopted by Oron *et al.*, with pump and Stokes pulses polarized along the x direction and probe pulse polarized along the y direction, while the CARS signal is detected along the ±45° polarization directions with respect to the x direction. To that purpose, after the sample, the polarization was rotated by 45° with respect to the x-plane using an achromatic half-wave plate (Fresnel Rhomb), and then the signal was separated by a Wollaston prism in two perpendicularly polarization directions, whose spectra are detected by a spectrometer with a dual-array CCD. By taking the difference of the acquired spectra and after a suitable normalization, implementing the double quadrature spectral interferometry (DQSI) [139] method, it was possible to retrieve the pure real and imaginary resonant CARS signals upon changing the phase of the narrowband probe pulse. Another approach to handle the NRB is the single-beam heterodyne CARS [140][142] where the blue tail of the excitation pulse, instead of being blocked, is employed as fully phase-locked LO for heterodyning, offering intrinsic interferometric stability. In one case [140] the whole excitation pulse except its blue tail was mechanically chopped at 700Hz, while its spectral phase was sinusoidally modulated by the shaper to provide spectral resolution. On the other hand, the blue tail of the pulse was attenuated by a neutral density filter to 5% to serve as LO and then after the sample the CARS signal, optimized for maximum intensity by varying the phase of the LO, was acquired with a photomultiplier and a lock-in detector referenced to the chopping frequency. To avoid the reduction of the average CARS signal due to the amplitude modulation, in another approach [141] the chopper was replaced by a pair of glass wedges sinusoidally modulating the

phase of the LO at 40 Hz frequency, whereas the excitation field was left unblocked and a sinusoidal phase function was applied to it by the shaper for spectral resolution. In addition, a constant phase was added to the LO to maximize the heterodyne CARS signal, which was detected by the lock-in at the 40-Hz modulation frequency. Wipfler *et al.* [142] proposed a different approach for single-beam heterodyne CARS in which a phase gate was applied to a narrow portion of a broadband pulse for spectral resolution, whereas the combination of the blue tail of the pulse and the NRB generated by the broadband pulse work as LO for the resonant CARS signal. Acquiring four measurements at four different phases of the gate and applying the DQSI approach allowed to extract multiplex CARS spectra.

An alternative pulse shaping technique for single-beam CARS is the so-called "spectral notch" shaping, [143][146] in which a narrow dip is carved in the broad pulse spectrum by a suitable filter. In a time-domain picture, a spectral-notch (or spectral-hole) shaped broadband pulse can be seen as a sum of an ultrashort pump/Stokes pulse and a long duration probe pulse with opposite phase. The ultrashort pulse generates a strong NRB, which works as a LO for homodyne amplification of the small multiplex CARS signal generated by the notch feature. The phase of the interferometric cross-term is governed by the vibrational resonance line-shape and by the phase structure of the notch feature. By recording two spectra at slightly different notch positions, spectrally separated by the notch width, and taking their difference normalized to the non-resonant spectrum, multiplex Raman spectra were retrieved. Natan *et al.* [143] have used an SLM-based pulse shaper to produce the spectral notch, while Shen *et al.* [146] placed a needle in a grating-based 4f pulse shaper and Katz *et al.* [144] and Natan *et al.* [145] used a passive shaper composed of resonant photonic crystal slab (RPCS), which is a waveguide etched with a sub-wavelength grating creating a tunable notch feature in the spectrum. SLM-free heterodyne CARS was also demonstrated by Suzuki *et al.* [147] as a modification of the setup by Oron *et al.* [132] using a frequency-resolved Michelson interferometer which splits a

broadband pulse into a broadband and a time-delayed narrowband pulse, with the phase of the narrowband pulse controlled by a retro-reflector on a piezo stage. In a completely different approach, von Vacano *et al.* [148] have shown time-resolved two-color single-beam CARS with polarization control. Starting from a single TL pulse, first two-color double pulses were created with an SLM-based pulse shaper by applying a linear spectral phase function with different slopes in two spectral regions. Additionally, polarization-shaping was applied to make the two pulses orthogonally polarized. The blue-shifted CARS signal was mostly free from NRB and the spectra were acquired as a function of mutual delay of the two pulses, the FT of which gave final CARS spectra. Recently, single-beam CARS with tailored spectral focusing was successfully demonstrated. [149] [150] A pair of equal quadratic phase functions with an optical frequency spacing matching a Raman resonance was applied to the excitation spectra by the SLM pulse shaper to create a pair of chirped pump and Stokes pulses with constant instantaneous frequency difference and in this way the excitation beam was spectrally focused to excite a single Raman resonance. A narrow portion of the excitation spectrum was reduced in intensity by amplitude shaping and delayed in time by a linear phase function to employ it as the probe to extract the CARS signal after build-up of the coherence.

Single-beam SRS was introduced by the Dantus group, [151][152] using a low repetition rate amplified femtosecond laser; the selective excitation of a single Raman mode was accomplished by an SLM-based pulse shaper using a pair of displaced parabolic phase functions resulting in time-delayed chirped pump and Stokes pulses for spectral focusing (see Figure 15 (f)). In addition, a time-delayed reference pulse, identical in intensity and spectrum but with spectral phase modified by adding material dispersion so as to separate the minima of the two phase parabolas and bring it out of resonance with the targeted Raman mode, was created. The two shaped pulses, the main pulse and the reference pulse, are sent to the sample and the reflected pulses are separated by a dichroic beam splitter into blue and red parts and sent to fast

WILEY-VCH

photodetectors. As a consequence of the Raman process within the main pulse, the blue part experiences SRL and the red part SRG, while the reference pulse is unaltered. Very recently Ito *et al.* [153] have demonstrated single-beam phase-modulated SRS where they used spectral focusing for selective spectroscopic detection. They have divided a broadband laser spectrum into three frequency bands; a broadband pump/Stokes pulse and two narrowband probes, phase modulated (PM) probe and LO probe. Spectral separation of the two probes matches a Raman vibrational mode i.e. $\omega_{PM} - \omega_{LO} = \Omega$, while the PM probe is given a phase modulation with a periodic saw-wave from -π to π, therefore virtually a linear phase. The broadband pump/Stokes pulse coherently excites multiple vibrational modes simultaneously, but when $\omega_{PM} - \omega_{LO} = \Omega$, a selective Raman mode Ω can be targeted using phase-to-intensity conversion process using two-beam coupling via Raman-induced refractive index modulation. As a result an energy exchange, equivalent to SRG and SRL, between two probe pulses takes place and such PM-SRS signal, synchronized with the 2π saw-wave PM frequency, can be easily extracted by lock-in detection at PM frequency. In addition, the two probe spectra were also given an equal linear chirp for spectrally focused detection of PM-SRS and by scanning $\omega_{PM} - \omega_{LO}$, the SRS spectrum was measured.

Overall single-beam CARS, while simplifying the excitation source and lending itself to very elegant implementations, is typically too slow for biomedical imaging applications. On the other hand, since it relaxes the requirements of strict spatio-temporal overlap of pump and Stokes pulses, it lends itself very well to stand-off spectroscopic identifications of molecules, in particular hazardous materials such as biological warfare agents and explosives.

4.5 Fourier-transform CARS

Fourier-transform (FT)-CARS is a time-domain technique using two time-delayed ultrashort pulses (the pump and the probe) with duration shorter than the period of the highest vibrational frequency of interest, as depicted in **Figure 16** (a). The pump pulse excites a vibrational coherence in the sample by ISRS, which in turn produces a time-dependent refractive index change. The probe pulse, which is a time-delayed replica of the pump, senses the time-varying refractive index and gets periodically blue and red-shifted, thus generating both Stokes and anti-Stokes components.
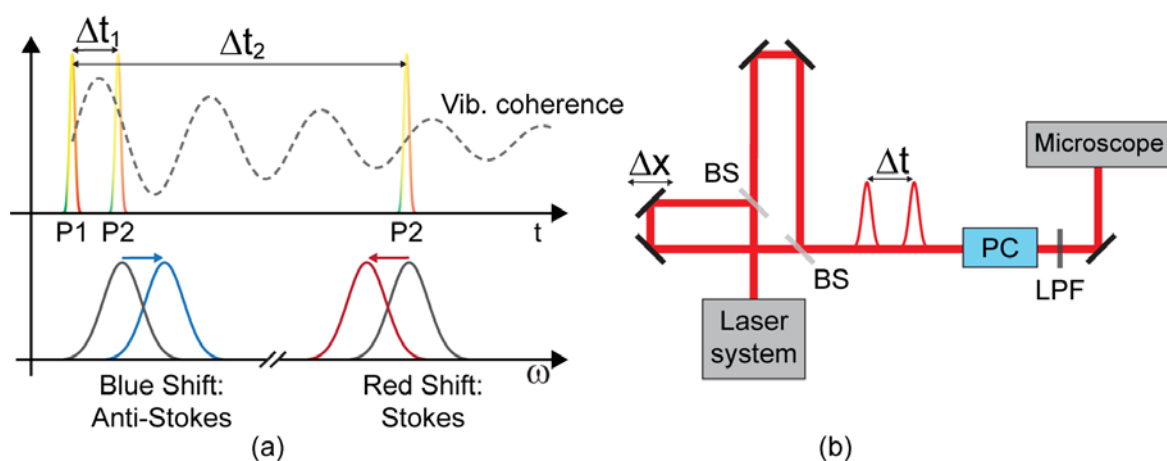

Figure 16 (a) pulse sequence and frequency shift in FT-CARS; P1: first pulse; P2: second pulse. (b) Experimental setup for FT-CARS . BS: beam splitter; PC: prism compressor; LPF: long-pass filter;

The anti-Stokes component is selected by spectral filtering and its energy is recorded as a function of the pump-probe delay, resulting in an oscillating pattern whose FT provides the CARS spectrum. FT-CARS presents the following advantages: (i) it allows the complete suppression of NRB, which is simply achieved by windowing out the contribution around zero delay, where pump and probe pulses are temporally overlapped; (ii) it has a spectral resolution which, like in all FT techniques, can be simply increased by extending the time span of the scan. However, FT-CARS presents also the following drawbacks: (i) it is currently capable to access only the fingerprint range, limited by the shortest pulsewidths (15-20 fs) that may be typically achieved in the focus of a microscope objective; (ii) the high peak powers of the ultrashort pulses greatly enhance multiphoton absorption mechanisms and may lead to photodamage; (iii)

the need to mechanically scan the pump-probe delay may limit the acquisition time of a single trace and thus the pixel dwell time.

A scheme of the FT-CARS setup used in the seminal papers by Ogilvie and coworkers, [154] [155] is shown in Figure 16 (b). It starts with a femtosecond Ti:sapphire laser, generating 15-20 fs pulses at 800 nm. The pulses are sent to a Michelson interferometer, producing two collinear replicas with variable delay which are focused on the sample by a microscope objective. A pulse compressor, consisting either of a prism pair or of multiple bounces on chirped mirrors, pre-compensates the dispersion introduced by the objective, ensuring a nearly TL pulse in the focus. The CARS signal is detected in the forward direction, collected by a second objective and focused on a photomultiplier followed by a data acquisition card. The signal is spectrally isolated from the background light by the combination of a long-pass filter (LPF) before the focusing objective and a short-pass filter (SPF) before the detector. By recording the CARS signal as a function of the delay, windowing out the NRB at time zero and performing a FT, one obtains the CARS spectrum.

It is possible to achieve heterodyne amplification of the CARS signal by the addition of a phase-coherent LO. This is achieved by replacing the LPF in the probe arm with a 4f zero-dispersion pulse shaper, in which a neutral density filter suitably attenuates the anti-Stokes portion of the spectrum down to a level at which it can be used as LO. This enables to amplify the CARS signal by almost two orders of magnitude.

The first experimental implementations of FT-CARS worked at relatively low speeds, limited by the mechanical delay line; recently, the technique has been upgraded to a scan rate of 24000 spectra per second, by the use of a rapid-scan retroreflective optical path length scanner. [156] The scanner is placed in one arm of the Michelson interferometer and consists of a 12-kHz resonant scanning mirror, a 1-inch concave mirror, and a rectangular mirror in a retro-reflective 4f configuration aligned in such way that the reflected pulse travels back along the same path

42

as the incident pulse except for the time delay produced by the scanner. The scanner introduces a maximum pathlength difference of 1 mm, which corresponds to a 10-cm^{-1} frequency resolution of the CARS signal. Since both forward and backward scans can be acquired, the effective scan rate is twice the mirror scan rate, i.e. 24000 spectra per second, corresponding to an acquisition time of 41.7 μs per spectrum. Recently, this system has been equipped with a higher frequency galvo mirror (50 kHz), which allows the measurement of 50000 spectra per second. [157] Finally, Duarte *et al.* [158] recently extended FT-CARS to widefield detection, using galvanometric mirrors for rapid scanning of the focal plane combined to an electron multiplied CCD camera for sensitive acquisition of the CARS signal. The rapid scanning has the advantage of minimizing the sample damage caused by the high peak power of the pulses.

One of the drawbacks of FT-CARS is the need to mechanically scan the delay between pump and probe pulse, which limits the acquisition interval of a single time trace. This limitation can in principle be overcome by dual-comb CARS, which avoids the use of moving parts with a configuration similar to that used for dual-comb absorption spectroscopy. [159], [160] It consists of two ultrashort sub-20-fs lasers, both of which generate frequency combs at slightly different frequencies, [161] which are collinearly combined and focused on the sample: the pump pulse train, with repetition frequency f_{rep}, and the probe pulse train, with a slightly lower repetition frequency $f_{rep} - \Delta f_{rep}$. The pump pulse excites via the ISRS process a vibrational coherence in the sample, as sketched in **Figure 17,** which results in a periodic modulation of its refractive index that in turn determines blue- and red-shifts of the probe pulse. Due to the small difference in the repetition rates of the two combs, for each pump-probe pair the delay increases by

$$\Delta t = \frac{1}{f_{rep} - \Delta f_{rep}} - \frac{1}{f_{rep}} \approx \frac{\Delta f_{rep}}{f_{rep}^2}, \tag{16}$$

thus allowing to rapidly scan the delay. As in FT-CARS, the pump and probe pulses are spectrally filtered by sharp LPF and SPF respectively and the probe energy is measured by a photodetector. By recording the interferogram as a function of pump-probe delay and down-scaling the time axis by a factor $\frac{\Delta f_{rep}}{f_{rep}}$, one obtains by FT the Raman spectrum, similarly to the FT-CARS configuration. The main advantage of dual-comb CARS is the very short acquisition time for a single spectrum, which is of the order of few to tens of microseconds.
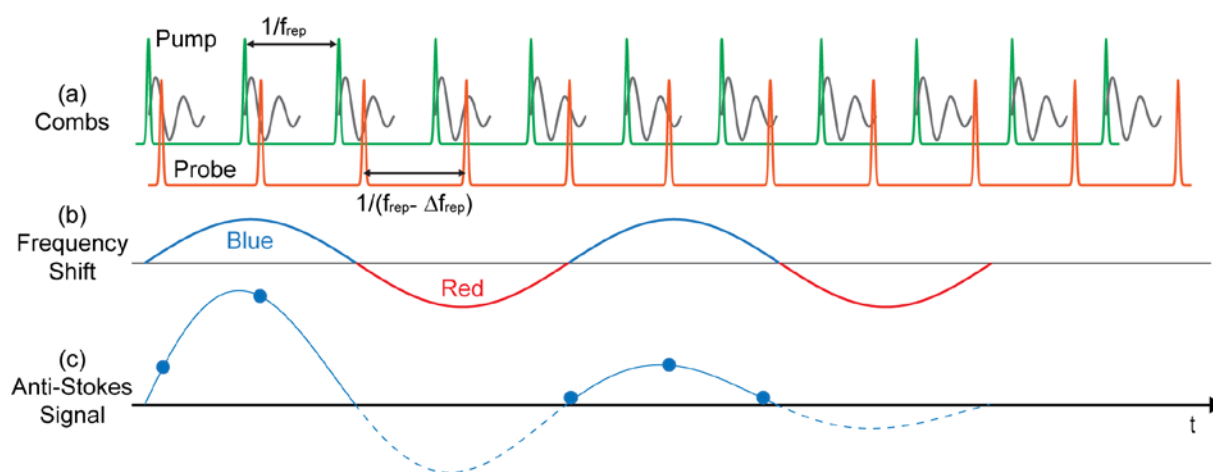

Figure 17 Principle of dual-comb CARS. (a) The pump comb (green) induces via ISRS a vibrational coherence, whose interaction with the probe comb (orange), occurring at different relative delays, produces its periodic blue and red shift (b) (see Figure 16 (a)). Measuring the anti-Stokes signal as a function of time (c), the CARS spectrum can be obtained by FT.

The first dual-comb CARS experiments by Ideguchi *et al.* [162] were performed with two 20-fs Ti:sapphire oscillators working at 100 MHz repetition rate; with $\Delta f_{rep} = 100$ Hz, the CARS spectrum of a mixture of solvents was recorded with high signal to noise in a time of 14.8 μs, with frequency resolution of 6 cm^{-1}. The main drawback of the dual-comb CARS technique when applied to imaging is the long pixel dwell time. In fact, while the acquisition time for a single scan is on the order of 10 μs, the total duration of a scan, required for the two combs to become synchronous again, is $\frac{1}{\Delta f_{rep}}$, which is of the order of 10 ms, leading to a pixel dwell rate of 100 Hz and to a duty cycle (defined as the ratio between the time required for one measurement and the time one has to wait before taking the next one) of the order of 10^{-3}. This drawback can be overcome by increasing the repetition rate of the laser. In fact, if f_{max} is the

highest vibrational frequency to be sampled (approximately corresponding to the inverse of the laser pulsewidth), then according to the Nyquist criterion one should have $\Delta t = \frac{\Delta f_{rep}}{f_{rep}^2} \leq \frac{1}{2 f_{max}}$, so that $\Delta f_{rep} \leq \frac{f_{rep}^2}{2 f_{max}}$; this shows that the maximum pixel dwell rate should in principle scale quadratically with the repetition rate of the laser. Recently, Mohler *et al.* [163] demonstrated dual-comb CARS using two mode-locked Ti:sapphire lasers at 1 GHz repetition rate. This should in principle correspond to an increase of the pixel dwell rate by a factor of 100 with respect to the results achieved in [162] but only a factor of 20 was achieved, up to 2 kHz. The reason for this is that higher repetition rates lead to lower pulse energies and peak powers, and thus to lower CARS signals (which display a cubic scaling with the pulse peak power).

The dual comb approach has also be used by Chen *et al.* in combination with SF [164] to take advantage of a more efficient excitation with respect to the previous FT dual comb CARS implementations. Recently, the dual-comb approach has been extended to a fiber-format laser system, based on two Yb-fiber oscillators followed by spectral broadening in a PCF, to generate sub-20-fs pulses. [165]

5. Broadband SRS techniques

This Section deals with the different experimental approaches adopted to record a broadband SRS spectrum. Due to the advantages of SRS discussed in Section 2, this field of research has been particularly active in recent years. We start with a survey of hyperspectral SRS techniques, which detect a single Raman vibrational frequency at a given time and then sequentially and rapidly scan the pump-Stokes detuning (Section 5.1); we then discuss multiplex SRS approaches, which detect the full SRS spectrum using either multichannel detectors or the photonic time-stretch approach (Section 5.2); finally, we discuss the FT-SRS technique, which detects the SRS spectrum in the time domain with a single detector (Section 5.3).

5.1. Hyperspectral SRS

After the demonstration of single-color SRS imaging at video rate through picosecond OPOs, [27] the first attempts to enhance the chemical specificity through the parallel or sequential acquisition of several vibrational modes relied on the intrinsic tunability of the OPO themselves. The stacking of sequentially acquired SRS images is however time consuming, due to the limited tuning speed of commercial OPOs as well as of most of the alternative laser solutions. [166] [167] A technique which partially circumvents these limitations is Spectrally tailored excitation
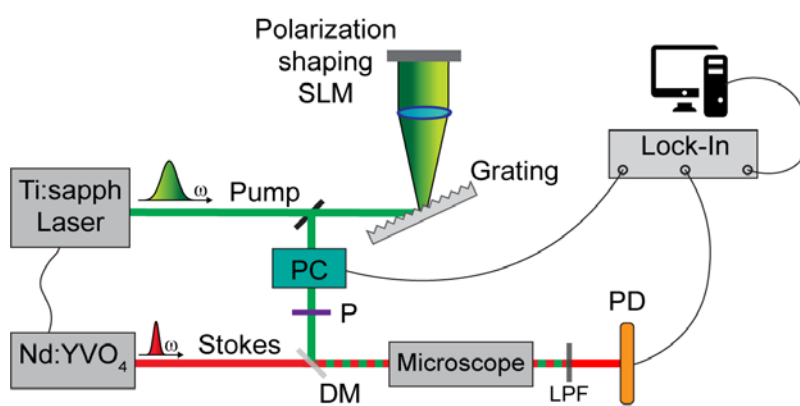

Figure 18 STE-SRS setup. SLM: spatial light modulator; PC: Pockels cell; P: polarizer; DM: dichroic mirror; LPF: longpass filter; PD: photo detector.

SRS (STE-SRS), [168] which allows highly specific imaging of a chemical species in the presence of other interfering species, based on tailored multiplex excitation of its vibrational spectrum. STE-SRS combines a broadband pump with a narrowband Stokes beam and measures the SRG of the Stokes with a single detector. The spectrum of the pump pulse is shaped with a SLM in such way that it predominantly excites the vibrational resonances of the target species; to suppress the contribution from interfering species, a second tailored pump spectrum is also prepared which targets the resonance of those species. The two tailored pump spectra are then rapidly alternated and the difference between the two SRS spectra is measured, thus effectively suppressing the contribution of the interfering species. The experimental configuration of STE-SRS is shown in **Figure 18**: two lasers, a narrowband picosecond Nd:YVO$_4$ laser generating the Stokes pulses and a broadband femtosecond Ti:sapphire laser generating the pump pulses, are electronically synchronized. The broadband pulse is sent to a reflective SLM-based polarization

---

pulse shaper, which encodes the spectra of the target and interfering species in two orthogonal polarizations. The shaped pump spectrum is then sent to a Pockels cell, which rotates the polarization by 90° at 4 MHz modulation rate, followed by a polarizer, so that the two pump spectra tailored to target and interfering species are alternatively transmitted. Pump and Stokes are synchronized, collinearly combined and focused on the sample in a standard single-frequency SRS configuration, in which the SRG of the narrowband Stokes is measured by a single photodiode and a high-frequency lock-in amplifier. STE-SRS was used to quantitatively determine the concentration of cholesterol in the presence of oleic acid, which has a rather similar Raman spectrum, as well as to perform *in-vivo* imaging of the distributions of different types of fatty acids in *C. elegans*. A drawback of the STE-SRS approach is the limited versatility, as it requires an *a-priori* knowledge of the vibrational spectrum of the target molecule and also of the possible interfering species. A similar approach was applied by Rehbinder *et al.* [169] to multiplex CARS, using a pulse shaper to select bands of interest in a broadband Stokes pulse tailored to specific molecules, thus reducing the photon load on the sample, partially suppressing the NRB and allowing fast acquisition of the CARS spectrum with a single detector.

A leap forward in the imaging speed of a hyperspectral SRS microscope was obtained by Ozeki *et al.*, [170] who managed to acquire in 3 seconds up to 90 spectral images made up of 480 x 500 points over a band of 300 cm^{-1} with a spectral detuning of 3 cm^{-1} from one another. This result remains at the state of the art despite the extremely fast evolution of SRS systems over the past 5 years. The achieved performance relies on a very low noise detection chain that enables pixel dwell times of only 0.1 μs, but even more it depends on the possibility to scan the frequency detuning between pump and Stokes beams with a millisecond time response.

The experimental setup used by Ozeki *et al.* is sketched in **Figure 19**. It makes use of a narrowband picosecond Ti:sapphire laser operating at repetition rate f_{rep} = 76 MHz and acting as a fixed-wavelength pump source, which is electronically synchronized to a broadband Yb:fiber oscillator acting as a source of Stokes pulses. The authors chose to detect the SRL of the pump, which is proportional to the average Stokes power, allowing the use of average Stokes powers before the onset of photodamage due to multi-photon absorption.
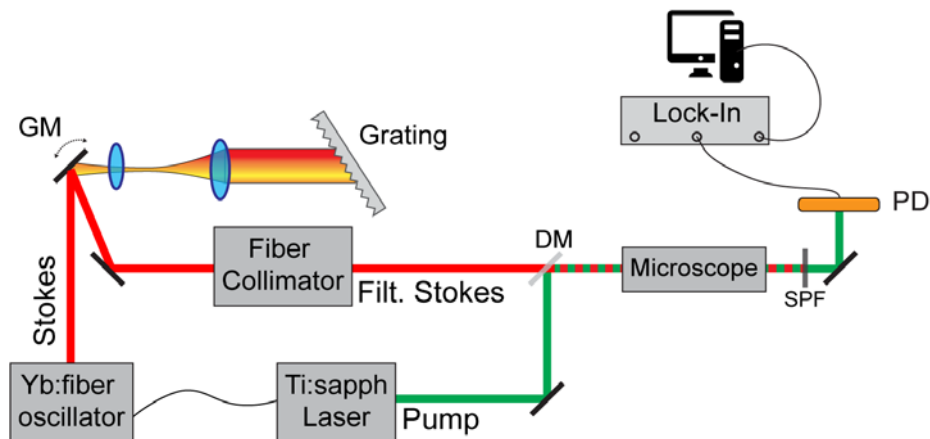

Figure 19 Experimental layout for an hyperspectral SRS microscope used by Ozeki *et al.* [170], allowing rapid tuning of the Stokes wavelength; GM: galvo mirror; DM: dichroich mirror; PD: photo diode.

The repetition rate of the Yb laser is set at 38 MHz so as to allow Stokes beam modulation and lock-in detection at the highest possible frequency, $f_{rep}/2$ = 38 MHz, without relying on external optical modulation. [171] A high-resolution tunable bandpass filter (TBPF) selects within the 30-nm-large oscillation bandwidth of the Yb:fiber oscillator the wavelength to be further amplified by an Yb:doped fiber amplifier (YDFA), up to an average power of 300 mW. [172] The speed of the TBPF is ensured by a galvanometer mirror (GM) introduced in a 4f pulse shaper composed of two relay lenses and of a reflecting grating in Littrow configuration: any change of the GM tilt results in a different incidence angle of light on the grating and hence changes the wavelength component back-reflected by the grating towards the amplifier. By proper synchronization of the GM tilt with the frame rate, almost dead-time-free images can be accumulated at different frequency detunings. From the technical point of view, the major disadvantage of this

configuration is the need for two synchronized laser sources, one of them being a low noise yet rather bulky and costly Ti:sapphire oscillator. The hyperspectral SRS microscope developed by Ozeki *et al.* was used for several biomedical applications, including two-dimensional spectral imaging of rat liver, two-colour three-dimensional imaging of a vessel in rat liver, spectral imaging of several sections of intestinal villi in mouse, and *in-vivo* spectral imaging of mouse ear skin. As an example, **Figure 20** reports three frames of an hyperspectral image of the sebaceous gland of mouse ear skin. A hyperspectral SRS imaging has been also realized by Kong *et al.* [173] who exploited a custom electro-optic Lyot filter, driven by a homemade electronic circuit, to rapidly tune the ouput of an OPO in a line-by-line fashion.
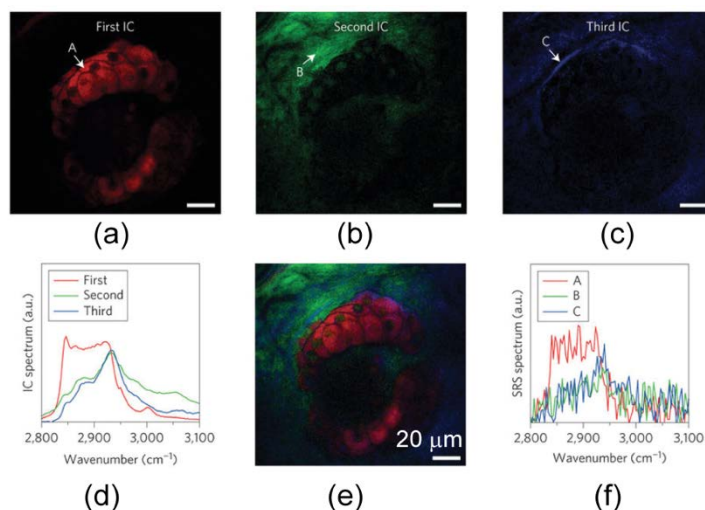

Figure 20 *In vivo* spectral imaging of the sebaceous gland of mouse ear skin. The hyperspectral image is analysed through independent component (IC) analysis. Panels (a), (b) and (c) are isolated ICs, whose spectra are reported in panel (d). The merged image is reported in (e). Panel (f) reports the SRS spectra taken at locations pointed by the arrows. Adapted by permission from Macmillan Publishers Ltd: Nature Photonics [170], © (2012)

In recent years a number of hyperspectral SRS setups have been developed based on the SF approach, where the scanning speed has been increased to a point to be able to interrogate each pixel at variable frequency detuning, typically within 30-60 µs. SF has been applied to SRS microscopy [166] [174] in a variety of configurations that allowed imaging and spectroscopy both in the fingerprint and the C-H stretching regions of synthetic and biological samples. [175] In these early demonstrations, the wavelength selection was performed on a frame-by-frame basis,

through a motorized translation stage. This is a time-consuming procedure that limits the overall acquisition speed. [176]
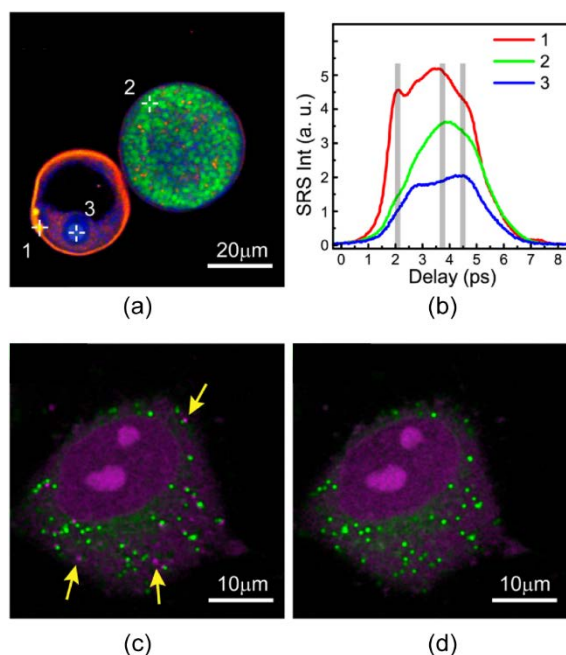

Figure 21 SRS spectroscopic imaging of biological samples using spectral focusing. (a) Three-color image of rice pollen grain. Lipids, starches, and proteins are false-colored red, green, and blue, respectively. (b) SRS spectra of three region of interest marked 1, 2, and 3 in (a), each acquired with 200 ms (c) Frame-by-frame and (d) line-by-line images of live HeLa cell, showing lipid (green) and protein (magenta) distributions; motion artifacts caused by drifting lipid droplets are shown with arrows. Adapted with permission from [180], OSA.

Recently, efforts have been devoted to increase the wavelength tuning speed, using rapid scanning optical delay lines whose designs have been borrowed from optical coherence tomography. [177] Liao *et al.* [178] used a 12-kHz resonant mirror, similar to that used by Hashimoto *et al.* for FT-CARS, to induce a millimetric path length difference between pump and Stokes pulses over a few tens of microseconds: thanks to the synchronization between this rapid scanning delay stage and the GMs of the microscope, SRS spectra spanning a 200 cm^{-1} bandwidth could be measured with 83-μs pixel dwell time and 25-cm^{-1} spectral resolution. The adopted galvo-scanning delay-line tuning resulted in increased wavelength switching speed with respect to conventional motorized delay-line tuning employed in spectral focusing SRS setups. The setup was used to acquire an hyperspectral SRS image of live *C. Albicans* in blood with frames of 400x400 pixels and 1 μs pixel dwell time. Recently, a similar setup [179] has been used as the excitation source for a fiber-based handheld SRS microscope, through which *in situ* imaging of

50

pesticide residuals on a leaf and canine cancerous brain tissue has been demonstrated as well as *in-vivo* imaging of cosmetics on human skin. A similar approach was recently reported by He *et al.*, [180] in which the mechanical delay line consists of a 4f configuration with a diffraction grating, a lens and a galvanometric mirror in the Fourier plane. [181] **Figure 21** reports spectral images of biological samples acquired with this configuration.

Another approach for the rapid scanning of the pump-Stokes delay in SF-SRS that does not rely on any mechanical component is based on the so-called Acousto-Optic Programmable Dispersive Filter (AOPDF). [182], [183] An AOPDF exploits the nearly collinear interaction between a train of ultrashort pulses and an acoustic wave, propagating in a birefringent crystal. If phase matching between optical and acoustic wave is fulfilled, an optical pulse polarized along the ordinary axis of the crystal experiences a partial diffraction to the extraordinary axis due to the interaction with the acoustic wave. As the diffracted pulse travels along the crystal with a different group velocity, it acquires a delay with respect to the original pulse. The amount of delay depends on the position where the interaction occurs and on the group velocity mismatch between ordinary and extraordinary waves. With lasers at a ~100-MHz repetition rate, the acoustic wave propagates a distance shorter than the crystal length during the repetition period (~10 ns), so that the acousto-optic interaction changes position from shot to shot, leading to a linearly growing delay of the diffracted beam. As a result, an AOPDF is able to scan a ps delay range with a repetition rate of tens of kHz. Alshaykh *et al.* [184] used an AOPDF in a hyperspectral SRS setup with femtosecond pump and Stokes pulses: the pump pulses are stretched by thick glass blocks, while the Stokes pulses are sent to the AOPDF which provides both the stretching and the delay. The system enables to perform SRS microscopy pixel by pixel with a 30 kHz scan rate, allowing the acquisition of a 400 x 400 pixels hyperspectral image within 5.3 seconds.

The SF concept was used for the so-called dual-phase SRS developed by He *et al.* [185], in which spectroscopic images are obtained probing simultaneously two different vibrational

51

modes. The setup, sketched in **Figure 22** (a), starts with two synchronized femtosecond pulses, linearly chirped though two SF57 glass rods, serving as pump (3.8 ps) and Stokes (1.8 ps) respectively. A delay line is used to select a first target Raman frequency Ω_1. The Stokes is modulated by an electro-optic modulator (EOM), tuned at one quarter of the laser repetition rate $f_{rep}/4$, such that the modulation period contains exactly four pulses. According to the modulation, the Stokes beam is either transmitted (S_T) or reflected (S_R) by a polarizing beam splitter. The delay of the reflected beam with respect to the pump beam can be precisely adjusted with a second delay line to excite also a second Raman frequency Ω_2 (see Figure 22 (b)). The transmitted and reflected Stokes beams are recombined through a second polarising beam splitter and then overlapped with the pump through a dichroic mirror. The second delay line also plays a fundamental role for the simultaneous detection of the signals produced by the two excited Raman resonances. After the EOM the phase difference between S_T and S_R is equal to
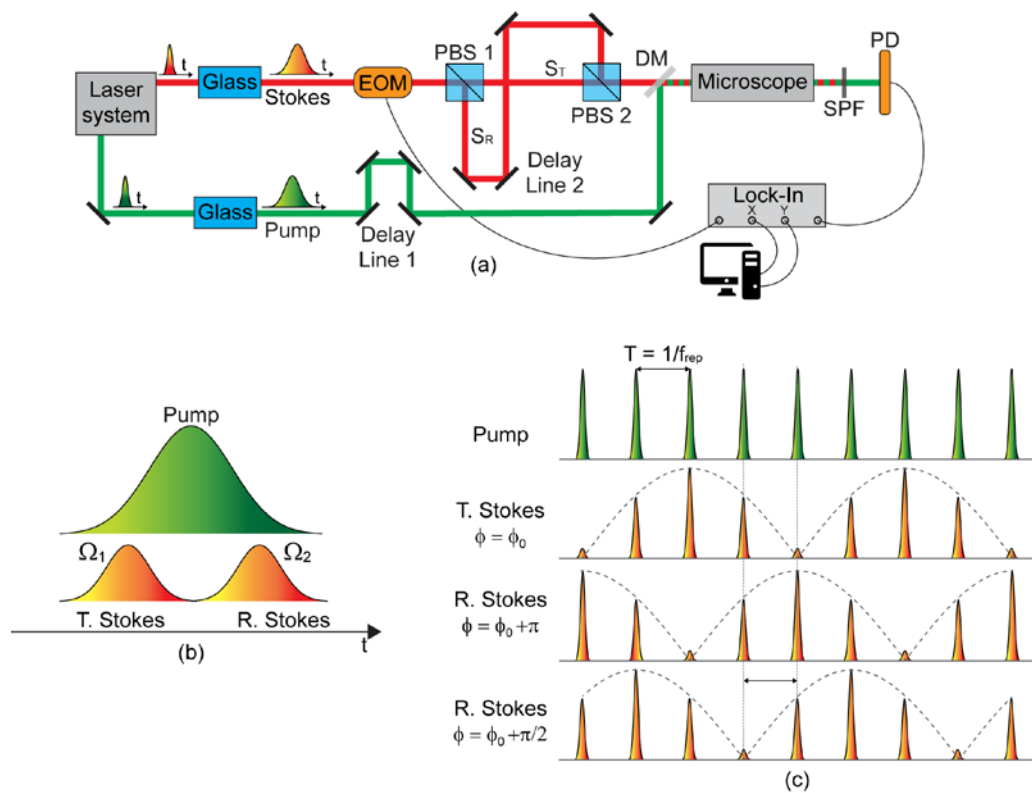

Figure 22 (a) Dual-phase SRS setup; EOM: Electro-optic modulator; PBS: polarizing beam splitter; S_T: Transmitted Stokes; S_R: Reflected Stokes; DM: Dichroic Mirror; SPF: shortpass filter; PD: photodiode. (b) temporal arrangement of pulses; (c) phase shift between transmitted and reflected Stokes.

π. Adding a delay equal to one laser repetition period $T = 1/f_{rep}$, the phase difference is shifted to $\pi/2$, such that the SRL signal reaching the photodiode can be written as

$$I_{SRL} = I(\Omega_1)sin\left(\frac{\pi f_0 t}{2} + \phi_0\right) + I(\Omega_2)cos\left(\frac{\pi f_0 t}{2} + \phi_0\right). \tag{17}$$

Therefore, with a phase sensitive lock-in amplifier one can detect the $I(\Omega_1)$ and $I(\Omega_2)$ components simultaneously through the in-phase (X) and quadrature (Y) output channels with proper setting of the reference phase ϕ_0, as depicted in Figure 22 (c). This system has been used to measure SRS on cultured cells, tissue sections, and live animals, both in transmission and epi detection, producing 512 x512 pixels images with 2 μs of pixel dwell time.

The same principle of phase sensitive detection was applied by Yang *et al.* [186] for simultaneous two-color SRS microscopy. Although the optical setup is conceptually similar to the one described above, the beam manipulation is rather different. The optical setup starts with a conventional IR ps laser, to produce the Stokes pulses, coupled with a tunable OPO, pumped by the second harmonic of the laser, that yields the pump pulses. The Stokes beam is modulated through an EOM and directed into a polarizing beam splitter. The spectrum of the reflected pulses is broadened through self-phase modulation induced by propagation in a 2-m single-mode fiber. The beam is then filtered through a 1 nm bandwidth tunable filter and amplified via a 20 cm ytterbium doped fiber amplifier (YDFA) pumped by a 976 nm laser. The wavelength of the output beam can be tuned adjusting the power of the pulse entering the single-mode fiber and the center wavelength of the filter. Through a second polarizing beam splitter and a dichroic mirror the two Stokes beams are recombined together with the pump, and directed to a laser scanning microscope. By means of two delay lines the optical path of the two Stokes beams is adjusted such that their phase difference is exactly π/2 and the two Raman signals generated can be simultaneously detected though the in-phase and quadrature outputs of a lock-in amplifier. The setup has been tested producing images of mouse brain in both forward- and epi-

detected mode. Moreover, *in vivo* imaging of mouse skin and white blood cells has been demonstrated.

Within the group of hyperspectral SRS techniques one may find also the so-called time-encoded (TICO) Raman. [187] It is based on a frequency-domain mode-locked (FDML) laser, typically used for optical coherence tomography, [188] generating a rapidly tunable monochromatic probe pulse, which is combined with a single-frequency pump pulse. The conceptual scheme of TICO Raman is shown in **Figure 23**: two narrowband laser sources, the Raman pump and the Stokes beam, are collinearly combined and focused on the sample. The Stokes beam is periodically swept in wavelength over time; as the pump-Stokes frequency detuning becomes resonant with a vibrational transition, the Stokes beam experiences the SRG effect. By encoding the Stokes frequency to the sweep time, one can then retrieve the SRG spectrum. The TICO Raman approach combines high acquisition speed, broad spectral coverage (750-3150 cm^{-1}) and high frequency resolution (up to 0.5 cm^{-1}) using a fiber laser system which has the merits of compactness and low cost that are highly desirable characteristics for a clinical setting. In the setup, the monochromatic pump laser is based on a master oscillator power amplifier actively modulated to nanosecond duration in order to increase the peak power, while the Stokes is a FDML laser which can be frequency swept at a
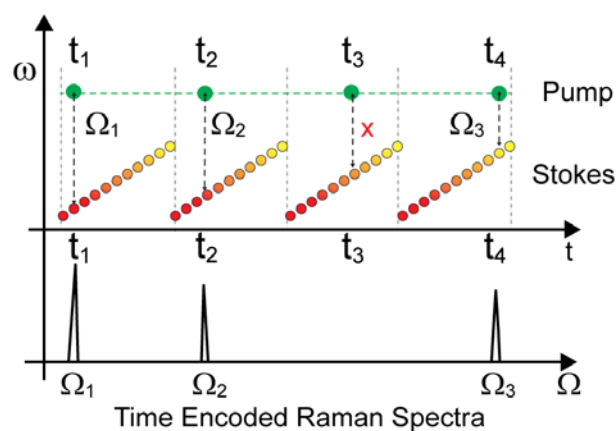

Figure 23 Principle of TICO Raman. The pump frequency is kept fixed, while the frequency of the ns Stokes pulses is periodically sweeped. The temporal overlap between pump and Stokes pulses defines the actual frequency detuning.

rate from 55 to 415 kHz. Pump and Stokes are collinearly combined and focused on the sample, and the Stokes pulse transmitted by the sample, together with a reference pulse, is sent to a balanced photodetector, which cancels the laser noise, allowing to achieve shot-noise-limited performance. Finally, the SRG signal is recorded by a high-speed analog to digital converter (ADC) working at a rate of 1 GS/s and averaged over several sweeps.

By using two FDML Stokes lasers and by frequency shifting the pump, the setup is able to cover the whole 750-3150 cm^{-1} frequency range. In addition, by reducing the span of the probe laser, TICO Raman is able to dynamically zoom on the spectral region of interest. The technique was used to measure (see **Figure 24**) Raman spectra of solvents with remarkably high frequency resolution and has proven the capability of imaging plant cells from *Geranium phaeum* stem in the fingerprint region, distinguishing lignin and olive oil with a pixel dwell time, after averaging, of 16 ms. Further improvements in the performance of TICO Raman are envisaged by boosting the power of the FDML laser through suitable fiber amplifiers, thus decreasing shot noise and improving the acquisition speed.
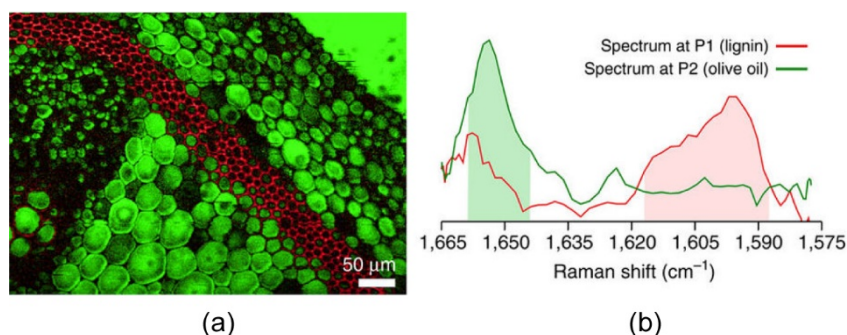

Figure 24 (a) Images of cells from *Geranium phaeum* stem with molecular colour code (lignin in red and olive oil in green). (b) Spectra at two pixels P1 and P2 and integration intervals used for colour coding. Adapted from [187]

All the above-described approaches to hyperspectral SRS microscopy employ a single-frequency configuration (either with narrowband pump/Stokes pulses or with broadband pulses combined with SF) and rapidly scan the pump-Stokes frequency detuning. A different approach is to use a broadband Stokes (pump) pulse and spectrally select a desired narrowband portion of it to achieve rapid wavelength tunability. Typically, such wavelength selection is done by mechanically

moving a diffraction grating or a galvo-mirror. One of these configurations was recently reported by Berto *et al.* ; [189] the setup uses a narrowband pump synchronized to a broadband Stokes, which after the sample is sent to a spectrometer equipped with a programmable fast digital micromirror device (DMD) and then to a single detector. The DMD enables selection of specific Stokes wavelengths for which the SRG is sensitively detected by a high speed lock-in chain, thus allowing a rapid reconstruction of the SRG spectrum. This setup is particularly appealing because it readily lends itself to compressive sensing, which could significantly reduce the acquisition times.

An elegant, purely electrical solution for very quick wavelength tunability is to employ acousto-optic tunable filters (AOTFs), which eliminate any mechanical movement inherent to gratings or galvo-mirrors. The operation principle of AOTFs relies on light diffraction induced by an acoustic wave in an anisotropic medium, whose frequency and amplitude allows controlling the wavelength and the intensity of the diffracted optical wave (see Error! Reference source not found. (a)). The typical wavelength tuning speed of present AOTFs reaches up to a few
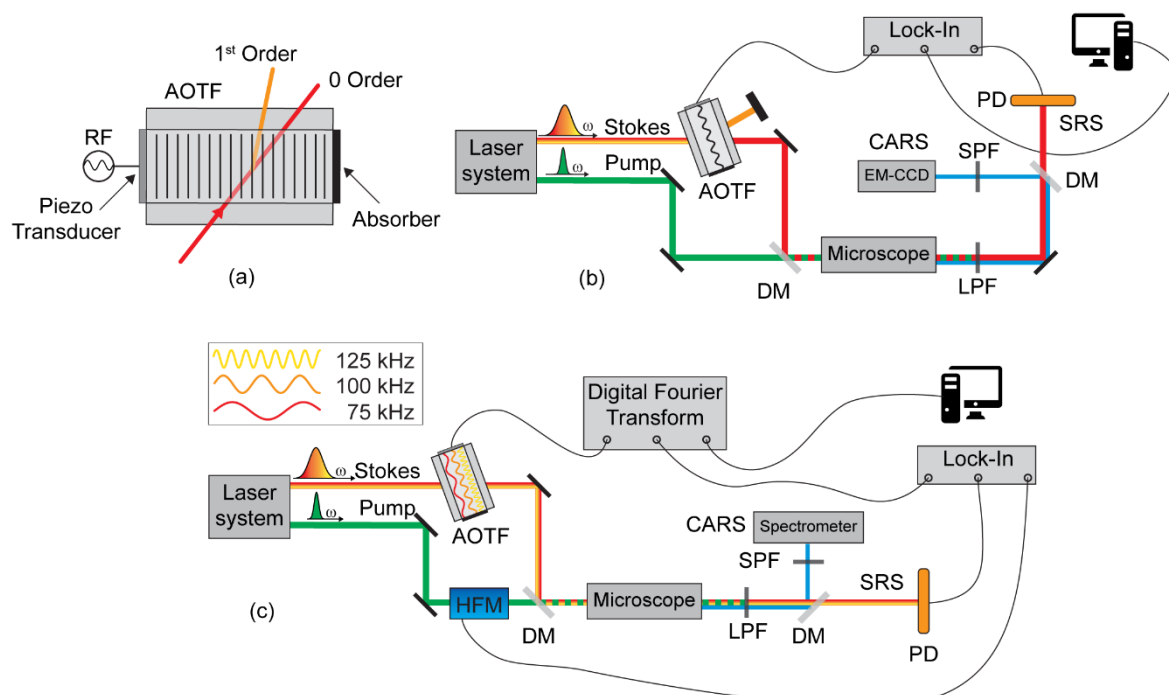

Figure 25 (a) A simplified sketch showing operating principle of acousto-optic tunable filter (AOTF), (b) and (c) illustrates the typical optical setups for single-frequency and multiplex CARS/SRS respectively employing an AOTF in broadband Stokes path; DM: Dichroic Mirror; LPF: long-pass filter; SPF: short-pass filter; PD: photodetector.

microseconds per octave, limited by the acoustic wave's transit time in the birefringent crystal, while the current spectral resolution is < 0.5 nm in visible and ≈2 nm in the NIR spectral range. The maximum intensity modulation frequency is limited to 1 MHz. AOTFs can be applied to CRS microscopy in a variety of modes: (i) in hyperspectral CRS, a single wavelength can be extracted out of a broadband pump/Stokes pulse, then either tuned 'sequentially' across a given range or stepped discretely at predetermined spectral positions; (ii) in multiplex CRS, several illuminating wavelengths can be selected simultaneously by applying different RF signals. In fact, currently available AOTFs are able to multiplex up to eight or sixteen (depending on the model) simultaneous wavelength channels. Schematic of typical setups for hyperspectral CRS and multiplex CRS are depicted in Figure 25 (b) and (c) respectively. Hashimoto *et al.* [190] have demonstrated high-speed hyperspectral CARS imaging of HeLa cells in a multi-focus excitation microscope employing an AOTF in two different configurations: (i) emission (CARS) filtering and (ii) excitation filtering. In the first configuration, the multiplex CARS signal, generated by combined action of a narrowband (picosecond) pump and a broadband (femtosecond) Stokes pulse, was spectrally selected for hyperspectral imaging using an AOTF placed before an electron-multiplying charge-coupled device (EM-CCD) camera. In the second configuration the AOTF was applied to the broadband femtosecond Stokes beam to synthesize a tunable narrowband (picosecond) pulse to be combined it with the narrowband pump on the sample for hyperspectral CARS imaging. In another arrangement, Meng *et al.* [191] have performed both CARS and SRS spectroscopy utilizing an AOTF as an excitation filter. Specifically, they used an AOTF to spectrally select a portion of a SC generated in a single-mode fiber fed by a picosecond 1064 nm Nd:YVO$_4$ laser, to synthesize a tunable seed for an OPA pumped by the SH of the same laser. The amplified signal of the OPA served as a source of tunable pump pulses, whereas a portion of the picosecond 1064 nm laser provided Stokes pulses, for both CARS and SRS spectroscopy. In order to detect SRG, the optional modulation function

of the AOTF was enabled and synchronized with lock-in detection. In a recent advancement, Cahyadi *et al.* [192] have incorporated an intra-cavity AOTF based picosecond mode-locked laser in an hyperspectral CARS setup to achieve fast spectral scanning with speed approaching 20 ms/wavelength change including cavity resynchronization time with a spectral resolution of ~4 cm^{-1}. Likewise, Mars *et al.* [193] have used a picosecond mode-locked 80 MHz Ti:sapphire laser equipped with an AOTF inside the laser cavity to directly obtain tunable Stokes pulses which were further intensity modulated at 20 MHz by an EOM placed outside the cavity, while a similar synchronized picosecond Ti:sapphire laser was used as a pump source. To perform hyperspectral SRS spectroscopy and imaging, in the detection they have used a home-built high-speed SRS lock-in pixel CMOS image sensor. This image sensor was fabricated on a chip that included a 10x10 lock-in pixel array and a pixel driving circuitry. Each lock-in pixel covering 10 μm x 10 μm area incorporated a large-area lateral electric field charge modulator (LEFM) detector and a lock-in readout circuit under it. The LEFM detectors ensure very quick charge transfer in less than few nanoseconds making it suitable for high-speed demodulation in MHz regime. For synchronous detection, a function generator has supplied a clock-signal to master laser, lock-in sensor and AOTF drive. In the same setup, hyperspectral CARS was also demonstrated by acquiring it simultaneously with SRS but through completely different detector system employing EM-CCD.

Furthermore, Fu *et al.* [194] have successfully applied an AOTF equipped with an 8-channel RF drive to demonstrate multiplex SRS microscopy using a femtosecond Ti: sapphire laser as a pump and an electronically synchronized picosecond Yb laser as a Stokes. The scheme is shown in Figure 25 (c). To avoid any channel cross-talk effect, only 3 out of 8 channels of the AOTF were used simultaneously to divide the femtosecond laser output in 3 wavelength bands, each tuned to one Raman signature of the investigated sample. The three channels were modulated at 125, 100 and 75 kHz respectively. Since the AOTF cannot provide intensity modulation beyond 1 MHz,

to enhance the SRS sensitivity, a double-modulation technique was implemented to move the detection at high Fourier frequency. To that purpose, the picosecond Stokes beam was also modulated at 20 MHz using an EOM and then, on the detection side, the total SRS signal was collected pixel-by-pixel on a single photodiode. For every pixel, the signal was first demodulated at 20 MHz using a high speed lock-in and then a real-time digital FT was performed to extract amplitude components of the SRS signal at the three lower modulation frequencies to extract different frequencies. Pixel-by-pixel scanning then ensures the acquisition of a multiplex SRS image.

5.2 Multiplex SRS

The principle scheme of a multiplex SRS setup is shown in **Figure 26**. A laser system produces a narrowband pump pulse and a broadband Stokes (or a broadband pump and a narrowband Stokes for the case of IRS), which are synchronized, collinearly combined and sent to the microscope. The pump pulse is modulated and, after the sample, the broadband Stokes is sent to a multichannel detector, which can be either digital (spectrograph + CCD, Section 5.2.1) or analog (diffraction grating + photodiode array + multichannel lock-in amplifier, Section 5.2.2) and the SRG spectrum is obtained by signal demodulation and normalization by the Stokes spectral density. An additional possibility for high-speed single-shot spectra detection is to mirror frequency into time delay using the photonic time stretch approach (Section 5.2.3).
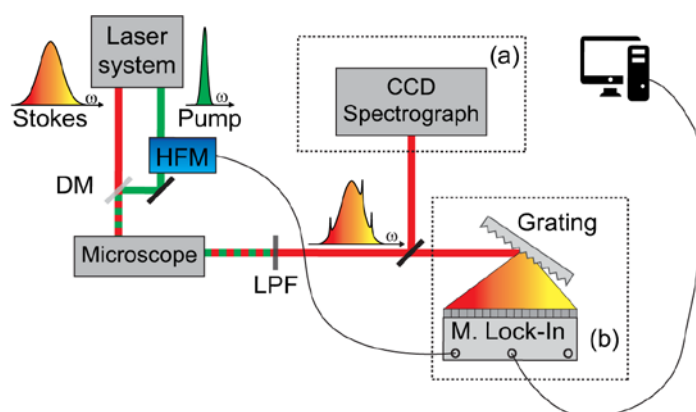

Figure 26 Principle of multiplex SRS detection: (a) using a spectrometer; (b) using a multichannel lock-in amplifier.

5.2.1 Digital demodulation SRS

Multiplex SRS is well known in the context of ultrafast optical spectroscopy, where the addition of a femtosecond actinic pulse to pump and Stokes, in the so-called femtosecond SRS (FSRS) technique [195], [196] enables one to measure time-dependent Raman spectra and to follow the light-induced structural evolution of a molecule in real time. [197], [198] In the context of microscopy, the first implementations of broadband SRS employed an optical multichannel analyzer (OMA), consisting of a dispersive spectrometer coupled to a linear detector array. In their pioneering paper Ploetz *et al.* [199] started with a Ti:sapphire laser generating 100-fs pulses

at 1 kHz repetition rate and 800 nm wavelength. A fraction of the laser output was sent to a bandpass filter, generating narrowband ($\approx$25 cm^{-1}) pump pulses with 270-nJ energy; another fraction was focused in a sapphire plate to generate a broadband white light continuum (WLC), extending both in the visible and the IR. Ploetz *et al.* chose to use the visible part of the WLC, because of its higher stability and the better detector sensitivity in the visible, thus measuring the broadband SRL spectrum (see Figure 4 (e)) according to the IRS process. [28] The narrowband pump pulse and the WLC are collinearly focused on the sample by a reflective Cassegrain objective and the spectrum of the transmitted WLC is measured by an OMA containing a 512-element diode array, working at the full 1-kHz laser repetition rate. By mechanically modulating the pump beam at half the laser repetition rate (500 Hz), it is possible to measure broadband SRL spectra (600-3800 cm^{-1} coverage). However, the low repetition rate of the laser limits both the sensitivity and the acquisition time. In fact, considering typical rms fluctuations of the WLC of the order of 1-2$\times$10^{-3} [200] (with the lower limit set by the full-well capacitance of each sensor pixel, of the order of 10^6 electrons), one can achieve sensitivities of the order of 10^{-4} for a 1 second acquisition time, which is not sufficient for imaging at reasonable speeds. To overcome this limitation, Gilch and coworkers developed an improved source for broadband SRS microscopy [201] with a much higher repetition rate. The system starts with a Ti:sapphire oscillator emiting 8-fs pulses (spanning 700-900 nm wavelength) at 75 MHz repetition rate, which act as broadband pump. A spectral tail of the laser output at 980 nm is selected and amplified in a series of YDFAs, to an average power of $\approx$50 mW. The broadband pump and the narrowband 980-nm Stokes are collinearly combined and the SRL of the pump is measured. While this setup has a much higher repetition rate and thus potentially much better sensitivity, it poses the challenge of how to detect a broad spectrum at high repetition rates. In the paper by Ploetz, the used detector was a diode array with maximum readout rate of 1 kHz, which resulted in pixel dwell times comparable to those achieved with the previous system. [195]

Full exploitation of the high repetition rate of the laser requires solving the technical challenge of building a multichannel detection with high speed and sensitivity.

An attempt in this direction was made by Rock *et al.*, [202] who reported on a broadband SRS system using a high-frame-rate CMOS camera. The system starts with two Ti:sapphire oscillators, one generating narrowband pump pulses and the other generating broadband Stokes pulses, synchronized by a hybrid electronic-optical system. The pump pulse is modulated at high frequencies by an acousto-optic modulator (AOM) and the probe pulse is measured by a CMOS imaging array with a maximum frame rate of 1 MHz (Fastcam SA5, Photron). This device uses an on-board memory buffer to store spectra acquired in real time before batch transferring them to the computer via gigabit Ethernet. By acquiring spectra at the full 1-MHz repetition rate and modulating the pump pulse at 500 kHz, it is possible to measure SRS spectra with a sensitivity of the order of 10^{-4} for 20 ms acquisition time. The system is however limited by the transfer time of the buffered data from the detector to the computer. Even if the detector can acquire a large amount of data in a short time (up to 10^5 spectra in less than one second) it takes a substantial amount of time (up to 5 minutes) to transfer them to a computer, again preventing high speed imaging. Recently, Gilch e *et al.* [203] upgraded their system by the use of a much faster multi-channel detector (Quantum Detectors, ULTRA) enabling to detect spectra with up to 10^8 photons per pixel in a time of 50 μs (corresponding to 20 kHz readout rate). By inserting an AOM in the narrowband Stokes path, they were able to record the SRL spectrum of a solvent (with maximum SRL of 6×10^{-3}) in a time as short as 100 μs (corresponding to a single modulation cycle) with SNR of 14. The same setup was employed for microscopy of a polymer blend sample with pixel dwell times as short as 100 μs. The current sensitivity of this multiplex SRS system is limited by shot noise, which in turn is dictated by the saturation charge of the detector (approximately 6×10^7 electrons full well capacity). A sensitivity improvement by a factor of 3 is expected by the use of an optimized detector, with a one order of magnitude higher full well capacity. [204]

Broadband detection was finally applied to the Raman Induced Kerr Effect (RIKE) [205] technique. RIKE relies on the Raman-induced birefringence that occurs when the pump-Stokes frequency detuning is in resonance with a vibrational transition, leading to a polarization change of the Stokes (pump) field. Shim and Mathies first demonstrated broadband RIKE spectroscopy, [206] while Bachler *et al.* [207] reported on a broadband RIKE microscopy setup that combines a narrowband circularly polarized pump with a broadband linearly polarized Stokes. The transmitted Stokes is detected through a polarizer perpendicular to the Stokes field. In this configuration, the homodyne detected RIKE signal is proportional to a different component of the nonlinear susceptibility sensor $\left|\chi_{1122}^{(3)} - \chi_{1212}^{(3)}\right|^2$ with respect to SRS which is proportional to $\chi_{1111}^{(3)}$ and it gives access to a purely resonant Raman signal in RIKE because the non-resonant third order susceptibility vanishes thanks to the property $Re(\chi_{1122}^{(3)NR}) = Re(\chi_{1212}^{(3)NR})$. [208] However, this signal is quadratic in sample concentration. A standard RIKE setup can be slightly modified for optically-heterodyne detected RIKE (OHD-RIKE) to detect Raman response proportional to $Im(\chi_{1122}^{(3)} - \chi_{1212}^{(3)})$ and linear in sample concentration as in SRS. For that a LO possessing a 90° phase shift with respect to RIKE signal is employed at Stokes field by introducing a λ/4 plate in the Stokes path before the sample and by slightly misaligning its principle axis with respect to Stokes polarization axis. Multiplex OHD-RIKE spectroscopy has been successfully applied by Klenerman *et al.* [209] and McAnally *et al.*, [210] while Freudiger *et al.* [211] in their hyperspectral OHD-RIKE microscopy setup have demonstrated that OHD-RIKE in circular pump excitation probes NRB-free Raman response like SRS. On the other hand, it also overcomes spurious background from cross-phase modulation (XPM) which is the limiting factor for SRS sensitivity in probing low chemical concentrations. In another approach called balanced-detection RIKE (BD-RIKE) spectroscopy and microscopy [212] where RIKE excitation was done with linear rather than circularly-polarized pump, a Raman response

proportional to $Im(\chi_{1122}^{(3)} + \chi_{1212}^{(3)})$ and also amplified by an automatic in-phase LO as in SRS was registered employing a balanced-detection preceded by a half-wave plate oriented at 45° with respect to Stokes polarization and a Wollaston prism. Hyperspectral BD-RIKE microscopy has been successfully demonstrated but it has never been realized yet in multiplex regime. Both OHD-RIKE and BD-RIKE combine the advantages of CARS and SRS in that they detect a signal which is free of both linear background (as in CARS) and NRB (as in SRS). However, similar to other polarization microscopy techniques, they suffer from spurious phase modifications and inherent depolarization in birefringent and heterogeneous samples which generate spurious background signals overlapping with the nonlinear signal of interest, and are especially detrimental when imaging non-homogeneous samples. Hence, their implicit benefits of improved sensitivity over SRS are hard to fully realize in practical environment of biological microscopy.

5.2.2. Analog demodulation SRS

Single-color SRS, using high-frequency modulation and synchronous lock-in detection, has demonstrated very high imaging speeds, with pixel dwell times of the order of a few µs. It would therefore appear straightforward to extend this approach to broadband operation by using an array of detectors, each one coupled to a corresponding input of a multichannel lock-in amplifier. This approach is in principle very powerful, since every spectral component is detected in parallel, avoiding potential bottlenecks. The first attempts in this direction were performed by Fa-Ke Lu *et al.*, [213] by combining a narrowband picosecond pulse acting as Stokes pulse with a broadband femtosecond pump pulse. The latter is directed into a reflection-configured grating-based pulse shaper, which masks part of the spectrum, producing a comb-shaped spectrum with three narrowband peaks. After synchronization and collinear recombination, pump and Stokes pulses are scanned on the sample. After filtering out the Stokes beam, the transmitted pump pulse is again dispersed through a grating, such that each narrowband peak is directed towards an

independent photodiode followed by a lock-in amplifier, thus allowing parallel and simultaneous SRS detection of the three excited Raman resonances.

A first attempt aimed at increasing the number of channels was performed by Kobayashi and coworkers. [214], [215] They used a picosecond Ti:sapphire oscillator coupled to a PCF to generate a broadband visible supercontinuum, resulting in narrowband Stokes and broadband pump pulses. The broadband pump transmitted by the sample was dispersed by a spectrometer and then coupled to a bundle of 128 fibers, each facing an avalanche photodiode connected to one of the channels of a multichannel lock-in amplifier (model 7210, Signal Recovery) in order to measure the SRL in an IRS configuration. However, commercial multi-channel lock-in amplifiers only work for low demodulation frequencies, up to ≈100 kHz. At the 4.8 kHz modulation frequency used by Kobayashi and coworkers, the 1/f noise of the laser system was still very high, resulting in a sensitivity of 10^{-4} for a pixel dwell time of 30 ms, which is too low for applications.

To overcome the 100-kHz limitation of the modulation frequency of commercial multi-channel lock-in amplifiers, Liao *et al*. [216] developed a multichannel lock-in-free detector based on an array of 16 tunable amplifiers (TAMPs). Each TAMP consists of an LC filter, tuned to the modulation frequency (chosen at 2.1 MHz), which selectively amplifies the SRG/SRL signal. [217] This filter is followed by amplifiers, band-pass filters and a rectifier, resulting in a DC signal that is read out by an analog to digital converter. Due to the simplicity of the TAMP circuitry, it is relatively straightforward to multiplex it, realizing an array of TAMPs. The experiment, whose optical scheme is drawn in **Figure 27** by Liao *et al*. used an Yb oscillator, producing 200-fs pulses at 1040 nm, which pumps an OPO, generating 120-fs pulses tunable
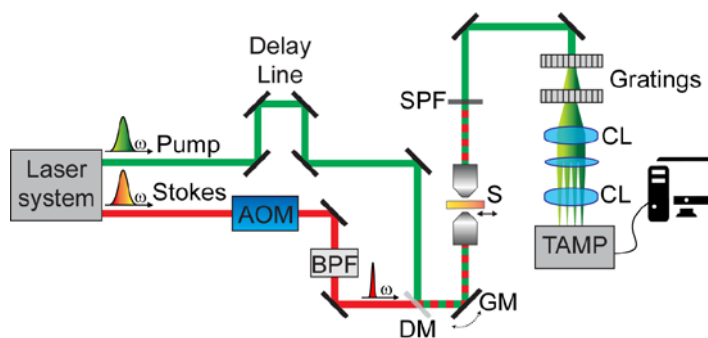
WILEY-VCH

Figure 27 Schematic drawing for SRS measurements with TAMP. M: mirror; AOM: acousto-optic modulator; SPF: shortpass fitler; S: sample; GM: galvo mirror; CL: cylindrical lens; TAMP: see text.

from 680 to 1300 nm. The 1040-nm beam, spectrally narrowed by a pulse shaper to 2.3-ps duration, acts as a fixed-wavelength narrowband Stokes, while the OPO output serves as a tunable broadband pump, covering a 200 cm^{-1} frequency interval. The narrowband Stokes is modulated at 2.1 MHz by an AOM. Pump and Stokes, collinearly combined by a beam splitter, are directed to a home-built laser scanning microscope. At the output of the microscope, the broadband pump is dispersed by two diffraction gratings and sent to an array of photodiodes. To maintain the spectral resolution, the direction of the beam on the plane of dispersion must remain fixed during the image scan. To that purpose, a hybrid scanning scheme is employed, with stage scanning in the direction of the beam dispersion, at speed of 40 μm/s, and a galvanometric mirror scanning scheme in the direction perpendicular to the dispersion plane. The dispersed pump beam is focused on the photodiode array by a 1-m spherical lens; in the direction perpendicular to beam dispersion, the back aperture of the collecting objective is conjugated to the array by a pair of cylindrical lenses. Each diode of the array has both a DC and an AC output; the AC outputs are sent to the TAMP array, and the 16 DC channels and the 16 TAMP outputs are sent to a 32-channel ADC working at 1-MHz acquisition rate. The multi-channel TAMP allows fast broadband SRL imaging with a pixel dwell time down to 32 μs. This broadband SRS microscope has shown its potential in several applications: [217] imaging of lipid droplets composition in live prostate cancer cells; monitoring intracellular metabolic

conversion of *all-trans* retinol to retinoic acid; differentiating within *C. Elegans* lipid droplets from protein-rich organelles; real-time visualization of drug diffusion through the mouse skin tissue *in vivo*, reported in **Figure 28**. This setup represents the current state of the art in multiplex SRS microscopy.
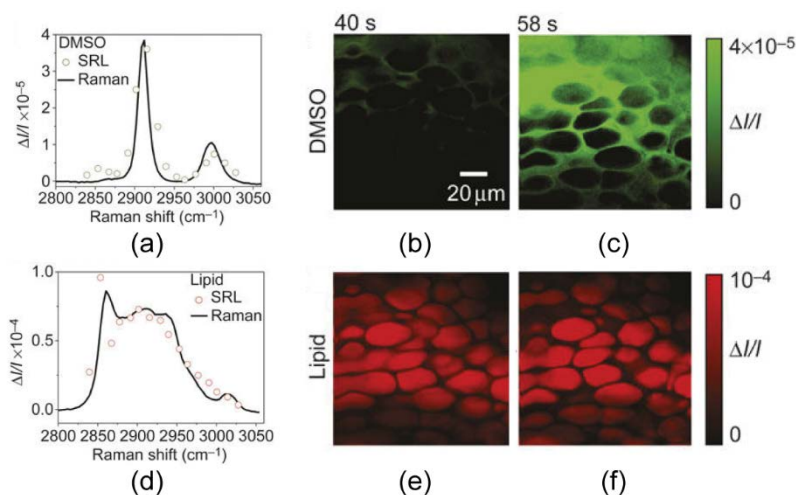

Figure 28 Following drug diffusion through the mouse skin tissue *in vivo* using the TAMP-based multiplex SRS. (a) and (d) comparison of SRL and SR spectra of DMSO and lipid; (b) and (c) time lapsed diffusion of DMSO molecules; (e) and (f) time lapsed diffusion of lipids. Adapted by permission from Macmillan Publishers Ltd: Light: Science & Applications [216] © (2015)

5.2.3 Photonic time stretch SRS

The photonic time stretch (PTS) approach, also known as dispersive FT spectroscopy, is a powerful technique for single-detector measurement of ultrashort pulse spectra at high repetition rates. [218]-[220] It consists in temporally stretching the pulse to be measured, typically by a long optical fiber, to a duration of a few nanoseconds, so that it can be accurately sampled by a high-frequency ADC. By calibrating the dispersion introduced by the optical fiber, each point of the sampled temporal profile can be uniquely associated with a wavelength, allowing measurement of spectra at repetition rates up to tens of MHz. With its unique capability to measure single-shot spectra at high repetition rates, PTS has found application in the detection of rare events, such as optical rogue waves, [221] and in the study of fast dynamical processes, such as the onset of the mode-locking regime from random intracavity power fluctuations. [222]

Recently, Saltarelli *et al.* [223] and Dobner *et al.* [224] applied the PTS approach to the detection of broadband SRS spectra. The concept of PTS-SRS is quite simple: a narrowband pump and a broadband Stokes pulse are combined and sent to the sample, the pump is modulated at high frequency and the Stokes spectra after the sample are detected on a single-shot basis by the PTS technique. The experimental setup of the PTS-SRS is shown in **Figure 29**.
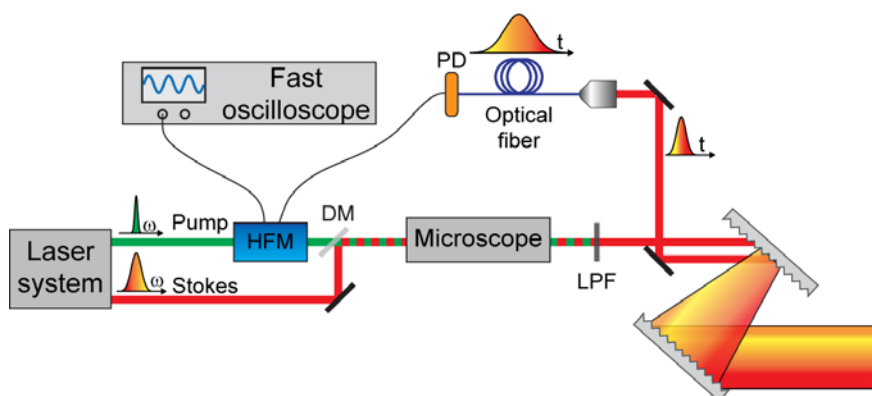

Figure 29 Setup of PTS-SRS. HFM: High Frequency Modulator, DM: dichroic mirror, LPF: Long-pass filter; PD: photodiode.

It starts with a regeneratively amplified Yb:KGW laser generating 290-fs pulses at 1026 nm with 80-kHz repetition rate. The laser output is divided in two arms: the first one generates the narrowband pump pulses and the second one the broadband Stokes pulses. The narrowband pump pulses are obtained by spectral filtering with an etalon, resulting in ≈1.7-ps pulses at 1026 nm with 8 cm^{-1} bandwidth and 350 nJ energy. The broadband Stokes pulses are obtained as the idler of an OPA, pumped by the SH of the laser; they span the 1450-1540 nm wavelength range, corresponding to a frequency detuning of 2700-3400 cm^{-1} and thus covering the entire C-H stretching band. A typical pulse energy of 1 nJ, much lower than the OPA output, is used on the sample.

The pump, modulated at 20-kHz frequency by an AOM, and the Stokes pulses, synchronized by a delay line, are collinearly combined by a dichroic beam splitter and focused on the sample. The transmitted Stokes, after recollimation, is sent to the PTS and the detection chain. The PTS consists of two stages: first a grating pair pre-stretcher introduces a negative dispersion, increasing the pulse duration to 33 ps and decreasing the peak power enough to allow neglecting non-linearities in the fiber. Then a 18.65-km-long single-mode telecom fiber further stretches the Stokes pulse to 15 ns. The stretched pulse is then sent to a fast photodiode and to an ADC through a high-bandwidth digital oscilloscope. Two different ADCs were employed: one with higher bandwidth (2.5 GHz, 40 GS/s sampling rate) but lower resolution (8-bit digitization) and one with lower bandwidth (1 GHz, 2.5 GS/s sampling rate) but higher resolution (12-bit digitization). Following a time-wavelength calibration of the PTS, broadband SRS spectra of different solvents were acquired, as shown in **Figure 30**.
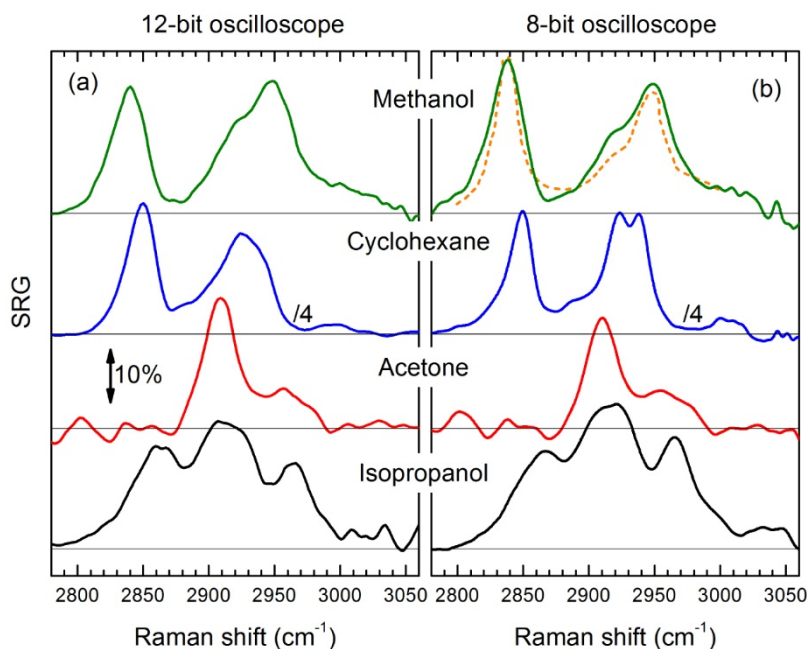

Figure 30 SRS spectra of different solvents measured by the PTS-SRS technique. Each spectrum is obtained acquiring N = 8 consecutive pulses (100-µs acquisition time) for the 12-bit (a) and 8-bit (b) oscilloscope. Orange dashed line in (b) is a reference SR spectrum of methanol. Pump energy was 200-nJ on the sample. The cyclohexane signal has been divided by 4 for comparison. From [223].

The current implementation of PTS-SRS, using an 80-kHz repetition-rate laser, covers a spectral window of 500 cm^{-1}, in the C-H stretching region, with frequency resolution of $\approx$10 cm^{-1} and a sensitivity of 10^{-3} over 400 μs and approaching 2×10^{-5} for a 1 s acquisition time. These performances are already suitable for a number of applications, such as monitoring microfluidic flows, [225] the onset of chemical reactions [226] or solid-state samples such as pharmaceutical products. [227] Future envisaged developments of the technique are: (i) broadening the OPA bandwidth, so as to allow the Stokes pulse to cover simultaneously the C-H stretching and the fingerprint region; in fact PTS-SRS has the remarkable advantage that the acquisition speed does not depend on the covered spectral region; (ii) increasing the laser repetition rate by two orders of magnitude to the 10-MHz range, allowing to improve both the acquisition speed and the detection sensitivity.

5.3 Fourier-transform SRS

A different approach to broadband SRS is based on FT detection of the SRG/SRL spectrum. [228] Similarly to FT-CARS, FT-SRS uses a single photodetector and thus a single-channel lock-in amplifier, however here the FT approach is used to detect the Stokes spectrum rather than the Raman spectrum, thus calling for a much higher accuracy of the interferometer due to the one order of magnitude higher sampled frequencies. FT-SRS relies on the time-domain measurement of spectra, in analogy with the FT-IR technique used in the MIR region. [229] Similarly to multiplex SRS setups described in Sections 5.2, it employs a narrowband pump and a broadband Stokes that are synchronized and focused on the sample. The pump beam is modulated at high frequency (ideally at half the laser repetition rate). Differently from the multiplex schemes which employ multichannel detectors, the Stokes beam, selected by a spectral filter after the sample, is sent to a linear interferometer (e.g. a Michelson) that creates two collinear identical replicas of the pulse, with variable relative delay Δt. The two replicas

interfere onto a single detector, giving rise as a function of Δt to the interferogram sketched in

red in **Figure 31** (a), and called the "Stokes interferogram".
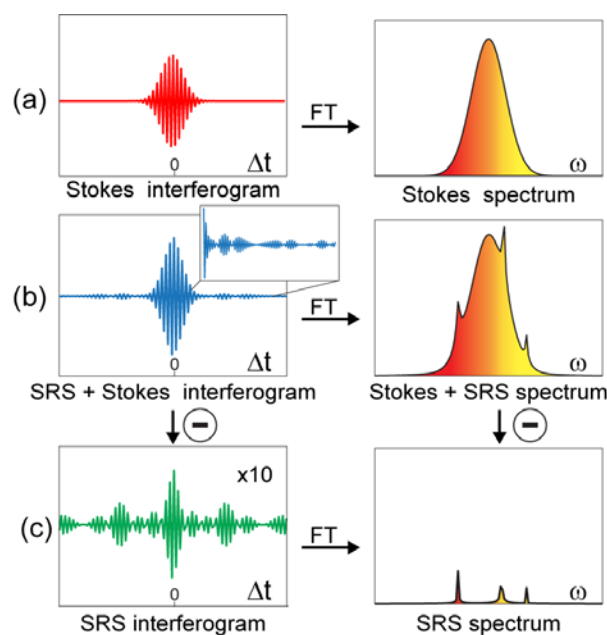

Figure 31 Principle of FT-SRS. Interferograms and corresponding spectra of: (a) Stokes pulse; (b) Stokes pulse
with SRS signal; (c) SRS signal.

According to the Wiener-Kintchine theorem, [230] the FT of the interferogram with respect to

Δt gives the spectrum of the Stokes pulse. The presence of SRG on the Stokes, induced by the

pump pulse in a sample with Raman gain, modifies the interferogram (see Figure 31 (b))

generating tails at long delays. The FT of the modified Stokes interferogram results in a

different Stokes spectrum, which displays gain in the form of sharp peaks at specific Stokes

frequencies. By computing the difference of the pumped and unpumped Stokes spectra and

normalizing over the unpumped Stokes spectrum, one finally obtains the SRG spectrum (Figure

31 (c)). To measure the tiny pump-induced modification of the Stokes interferogram, high speed

modulation transfer and lock-in detection are required. Thanks to the linearity of the FT

operator, the difference between the FTs of two interferograms (see Figure 31 (a) and (b), right

panels) is equal to the FT of their difference (see Figure 31 (c), right panel). One can thus first

obtain directly the difference of the two Stokes pulse interferograms from the lock-in amplifier,

resulting in the so-called "SRS interferogram". Second, by calculating the FT of the SRS

interferogram and normalizing it by the FT of the Stokes interferogram, one obtains the SRG spectrum. The experimental set-up used for broadband FT-SRS is shown in **Figure 32**.
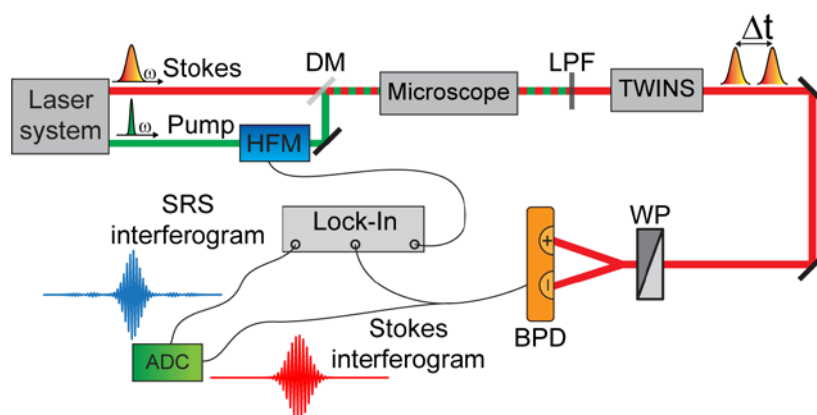

Figure 32 Scheme of the FT-SRS setup. HFM: High Frequency Modulator; DM: dichroic mirror; LPF: long-pass filter; TWINS: see text; WP: Wollaston prism; BPD: balanced photodetector; ADC: analog to digital converter.

It starts with an Er:fiber oscillator feeding two independent EDFAs, each producing 70-fs pulses at 1560 nm with 350-mW average power at 40-MHz repetition rate. One EDFA output is frequency doubled in a 1-cm long PPLN crystal, producing a narrowband (~15 cm^{-1}) 783-nm pump pulse with average power up to 110 mW and ~2ps duration [45], [46]. The second EDFA output is spectrally broadened in a HNF with a zero-dispersion wavelength that is close to, but slightly shorter than, the input laser wavelength. The short-wavelength dispersive wave, peaked at 1050 nm and compressed to nearly TL 20-25 fs duration by an SF10 prism pair, is used as the broadband Stokes pulse, allowing to cover the C-H stretching band. Pump and Stokes are synchronized by a delay line, collinearly combined by a dichroic beam splitter and focused onto the sample by a microscope objective. The pump pulse is modulated by an AOM at a 3-MHz frequency. After the sample, the Stokes is recollimated by a second objective, filtered from the pump by a long-pass filter and sent to a common-mode birefringent interferometer called Translating-Wedge-based Identical pulses eNcoding System (TWINS) [231] [232]. This is a passive delay line capable of generating two pulse replicas with attosecond control of their relative delay, thanks to its common-path geometry. In TWINS the energy of the input beam is equally distributed into two perpendicularly polarized components that collinearly propagate

along the fast and slow axes of the birefringent material. The delay between these two components can be arbitrarily controlled varying the thickness of the birefringent material, inserting the wedges in and out of the beam through a motorized translation stage. The output of the TWINS is sent to a Wollaston prism (WP) oriented at 45° with respect to the optical axes of the birefringent wedges. In this way, two spatially separated and perpendicularly polarized beams are generated. Each beam contains the two interfering delayed pulses generated by the TWINS. These two beams are sent to the photodiodes of a balanced detector, which measure two interferograms that are 180° out of phase. The output of the balanced detector is sent both to an ADC (to record the Stokes interferogram) and to a high-frequency lock-in amplifier (to record the SRS interferogram). Since the output of the balanced detector is the difference of the light intensities at the two photodiodes, the interference pattern is multiplied by two with respect to the single-channel configuration. Furthermore, differential detection effectively cancels the Stokes pulse intensity noise.

The FT-SRS technique was used to measure SRS spectra of different solvents and to acquire images of polymer blends. [228] Currently, the time required for the acquisition of a single FT-SRS spectrum is limited to a fraction of a second by the translation speed of the birefringent wedges. However, there are two strategies that can be used to decrease the measurement time by several orders of magnitude: step scanning and undersampling. The first consists in recording a full SRS image for a given interferometer delay, and performing the FT operation for all pixels in parallel only at the end of the measurement. This is only possible thanks to the inherent long-term delay stability of the TWINS interferometer. The second strategy consists in sampling the interferogram at a frequency lower than the Nyquist limit, thus considerably reducing the number of points. If applied together, these upgrades could increase the acquisition speed of FT-SRS to a point that makes it attractive for applications. In a completely different SRS imaging setup, Liao *et al.* [233] have retrived the multiplex SRG signal using FT in a

single photodiode detection arrangement where the sample was irradiated by a multiplex-modulated broadband pump and a narrowband Stokes. First, a grating dispersed the broadband pump pulses vertically and then a polygon mirror scanner projected them horizontally onto a reflective pattern containing 16 different densities. Consequently, the dispersed pump spectra were modulated at 16 different frequencies ranging from 1.5 to 3.0 MHz. This retro-reflective arrangement sent back the multiplex-modulated pump pylses to be combined on a dichroic mirror with narrowband Stokes pulses before focusing them on to the sample. After spectral filtering of the pump the signal was collected on a photodetector equipped with a resonant circuit centered at 2.25-MHz with 1.5-MHz bandwidth. A 60-μs time trace of the signal was recorded which was Fourier transformed to get full SRG spectra.

6. Conclusions

This concluding paragraph provides a comparative analysis of the most recent and powerful variants of CARS and SRS approaches for broadband label-free imaging. Table 1 summarizes, for every approach, a few relevant parameters. The adopted laser source is a figure of merit since it should ideally match the requirements of compactness, long-term reliability and cost-effectiveness. The pixel dwell time is a crucial benchmark for the data acquisition speed and thus for the capability of *in-vivo* imaging of tissues. The spectral coverage is relevant both in terms of extension and of position (fingerprint and/or C-H region), as it pertains to the capability of the system to detect different spectral signatures and to discriminate among molecular species. It also acts as a normalization parameter for the acquisition speed, since the latter crucially depends on whether the C-H or the fingerprint region is targeted. The number of spectral points is another figure of merit for the chemical selectivity that should be cross-correlated to the spectral coverage. The tuning range assesses the versatility of the system to address or not a given spectral region. Finally, the typology of the investigated samples is an indicator of the maturity level of a given approach with respect to biological applications. The

spectral resolution is also reported, but in this respect, we may already observe that most approaches quite well comply with the 10-20 cm^{-1} level that is considered as a rule of thumb to discriminate among spectral features in the condensed matter phase.

The different approaches have been classified in 4 categories, depending on the CRS technique, either CARS or SRS, and on whether the spectral information is multiplexed in the spectral domain, by means of a dispersive element followed by a parallel acquisition with an array of detectors, or in the time domain, by use of a single detector combined with a FT or a time-encoding approach. A first consideration on laser sources that emerges from the Table is the growing success of green-pumped femtosecond OPOs, as an alternative to the relatively old, bulky and costly solutions given by a pair of electronically synchronized Ti:sapphire oscillators [43] or by a picosecond Nd:YVO$_4$ oscillator pumping an OPO. [44] Besides compactness and cost, femtosecond OPOs afford Watt-level power both at the Stokes and at the pump wavelength, the former being at around 1060 nm as a result of the driving Yb:based oscillator wavelength, the latter tunable from 680 nm up to degeneracy as a result of the OPO output. These laser sources lend themselves both to spectral focusing schemes, where fast spectral reconfigurability is obtained by changing the delay of (properly chirped) pump and Stokes pulse trains, and to more conventional picosecond-femtosecond combinations once spectral filtering has been applied to convert the Yb:based oscillator femtosecond pulses into picosecond pulses at the Stokes wavelength. [216] Their major limitation is currently represented by a typical pulse-width of ≈200 fs, which translates into a spectral coverage limited to 200 cm^{-1} for a predetermined setting of the OPO (pump) wavelength. FT-CARS requires much shorter pulses, down to 15-20 fs if the fingerprint region is targeted, which explains why it has been applied so far almost exclusively with Ti:sapphire oscillators. Prospectively, they are likely to be replaced by more compact and robust Yb-based oscillators followed by proper schemes for spectral broadening and pulse compression. [165] A specific comment concerns fiber-format

sources, which are only represented in the Table by a multi-branch amplified Er:fiber system adopted for broadband CARS: their strength relies on the small footprint, the intrinsic robustness given by optical fibers, the delivery of synchronized pulse trains at different colours and the availability of ultra-broadband pulses [38] by SC generation in HNFs. On the other hand, their power scalability is an issue and, most of all, they do not satisfy the requirement of shot-noise limited detection in SRS approaches (unless with balanced [47], [70], [71] or auto-balanced [49] configurations) due to their relatively high intensity noise, even at high Fourier frequencies.

In terms of acquisition speed, the general behaviour necessarily reflects an inverse relationship with the number of spectral points. This is one of the reasons why CARS approaches, which are typically designed to cover larger spectral ranges with a denser frequency grid, result to be proportionally slower than SRS approaches where the maximum speed has been quite often pursued at the expense of the spectral detail. Another reason is that CARS requires low-noise high-dynamic-range cameras whose time response can't easily match the microsecond range afforded by a high-frequency lock-in amplifier under SRS detection. An exception is represented by the 40 μs time demonstrated by Hashimoto *et al.* in an FT-CARS configuration [156] where a resonantly rotating mirror results in a microsecond-scale tuning of the optical path difference between the two arms of the interferometer. While this result highlights the potential of FT-CARS for ultrafast broadband spectroscopy, it does not fully unveil, on the other hand, its potential for the imaging of biological samples, which are likely to suffer from the very high peak power density needed for ISRS excitation. Pixel dwell times as low as 0.5 μs suitable for real-time imaging have been instead achieved by SRS, yet in a two-colour ([185], 0.5 μs) and in a three-colour version only ([213], 3.8 μs), in the latter case recurring to a dispersive grating and to a rather bulky solution consisting of three lock-in amplifiers. Among multi-detector SRS approaches, the best trade-off between pixel dwell time (32 μs) and number

of spectral points (16) has been demonstrated by Liao *et al.* using a 16-channel detector feeding a chip-scale array of TAMPs. [216] Interestingly, these were shown to nearly match the performance of much more expensive and bulky lock-in amplifiers. Besides dispersive spectrometers, an intriguing solution to get parallel multiplexing of several colours is given by AOTFs, which allow up to sixteen independent spectral bands to be modulated at different frequencies with a resolution as low as 10 cm^{-1} and then re-extracted by proper multi-channel demodulation. Interestingly, this solution requires one detector only. On the other hand, the relatively low modulation frequencies afforded by AOTFs (in the hundreds kHz range) limit the integration time to a few tens of μs and also impose the use of balanced detection schemes to approach the shot-noise limit in a frequency region where laser intensity noise typically remains above that limit. In parallel with multi-detector approaches, a higher and higher number of SRS techniques based on the time-encoding of the spectral information have been developed, the final aim being to sequentially acquire at each pixel the SRS signal over a given spectral band, thus at the microsecond time scale. This brought to a resurgence of interest for the relatively old spectral focusing technique, [84] yet upgraded with ultrafast tunable delay lines given either by scanning mirrors or AOPDFs: these approaches offer quite similar performance, with pixel dwell times of about 30 μs over a 200 cm^{-1} bandwidth, which is available with commercial femtosecond OPOs. Another approach is the so-called TICO Raman, where a rapidly-swept cw laser is coupled to an actively modulated nanosecond pump laser: it exhibits a lower speed (16 ms pixel dwell time), but it offers the advantage of an extreme spectral resolution (1.4 cm^{-1}) that can considerably enhance the chemical selectivity, particularly in the fingerprint region where the spectral detail is known to make the difference. On the technical side, it suffers from the need of a highly specific laser solution and from the nontrivial balancing between reference and signal arms during the spectral sweeping. Still within time-encoded SRS, other promising approaches have been demonstrated very recently, either oriented to a high

degree of spectral reconfigurability by use of digital micro-mirror devices [189] or to the maximum imaging rate in a two-colour microscope (pixel dwell time of 0.5 µs) based on dual-phase SRS.

The above comparative analysis does not exhaustively cover the technical details of the many approaches proposed so far. Moreover, not all approaches offer the same maturity level for biological investigations, as it is evidenced form the application column. The overall picture, however, clearly highlights a rapidly evolving field where the advent of new technology is fuelling new ideas and meanwhile raising the level of performance. On the SRS side, where the fundamental trade-off given by the shot-noise limit has been already demonstrated at the maximum tolerable power levels for biological tissues, revolutionary changes can't be easily expected. Yet, the advent of OPOs with a broader bandwidth is likely to offer more degrees of freedom for the selection of the spectral features to be monitored. [234] Faster delay lines could shorten to the sub-10-µs level the pixel dwell time in the C-H stretching region. Also, the design and development of specific electronics is likely to become a relevant add-on, as it was pioneered by the group of Ji Xin Cheng with a chip-scale array of tunable amplifiers. On the CARS side, major benefits could derive from the rapidly evolving technology of cameras, with higher number of electrons per pixel, lower noise and higher speed and contrast, but also from the laser field, by more powerful fiber lasers and also by spectrally broader fiber and OPO sources, particularly for FT-CARS. The result obtained by Camp *et al.*, with a huge spectral coverage and an integration time of only 3.5 ms in the fingerprint region, though at the price of post-processing for NRB removal, is highly inspiring for future CARS microscopes.

WILEY-VCH

AUTHOR	APPROACH	LASER SOURCE	Pixel dwell time	No. spectral points	Resolution (cm^{-1})	TUNING (cm^{-1})	SAMPLE
Fa-Ke Lu (2012) [213]	Grating + multiple lock-in.	Synchcronized Nd:YVO4 & Ti:sapphire @ 80 MHz	3.8 µs	3	10-20	CH stretching	Lipids/proteins mouse ear skin
Liao (2015) [216]	Grating + TAMP	fs OPO	32 µs	16	11	0-4000	In vivo skin tissues
Dan Fu (2012) [194]	AOTF-3 colours	Synchronized Nd:YVO4 & Ti:sapphire @ 80 MHz	200 µs	3	33	CH stretching	Mouse ear skin tissue
Liao (2015) [233]	FT multiplex SRS	Synchronized dual output fs source @ 80 MHz	60	16	15	CH stretching	Mouse skin, human breast cancerous tissues
Chien-Sheng Liao (2016) [178]	Spectral focusing + resonant delay scanner	fs OPO	83 µs	8	25-32	0-4000	Organelles in live cells
Alshaykh (2017) [184]	Spectral focusing + Dazzler	fs OPO	30 µs	180	25	0-4000	Fungal cells
Karpf (2015) [187]	TICO-Raman	Actively modulated ns source @ 3 wavelengths + 2 FDML	16 ms	64	1.2	750-3150	Geranium phaeum stem
Ruoyu He (2017) [185]	Dual-phase SRS	fs OPO	0.5 µs	2	23	0-4000	In vivo animals
Berto (2017) [189]	DMD + lock-in	Synchronized Ti: sapphire	1 ms	24	0.5	980-1100	Solvents
Muller (2002) [84]	Multiplex CARS	Synchronized ps & fs Ti:sapphire	50 ms	32	5*	0-4000	Multi-lamellar vesicles
Ji-Xin Cheng (2002) [96]	Polarization Multiplex CARS	Synchronized ps & fs Ti:sapphire	2 s	32	5	0-4000	Multi-lamellar vesicles
C.H. Camp Jr (2014) [38]	Multiplex CARS	Er:fiber laser + EDFAs+ HNF	3.5 ms	330	10	470-3800	Hystopathology Liver tissues

J.P. Ogilvie (2006) [154]	FT-CARS	Ti:sapphire + scanning Michelson	1.5 s	400	3	200-1400	Polystyrene beads
Hideguchi (2013) [162]	Dual-comb FT CARS	Synchronized pair of Ti:sapphire	20 ms	120	10	200-1400	Capillary plate
Hashimoto (2016) [156]	Resonant delay scanner FT-CARS	Ti:sapphire	41 μs	130	10	200-1500	Toluene
Duarte (2016) [158]	Wide field FT-CARS	Ti:sapphire + scanning Michelson	1.8 ms	130	9	400-1600	PMMA PS beads
Kun Chen (2017) [164]	Spectral focusing + dual comb FT-CARS	Synchronized Yb-fiber oscillators	0.8 ms	40	15	1100-1700	Retinoic acid β-carotene

*Set by the camera; the laser offers a 1.5 cm^{-1} resolution

Table 1: comparison of different broadband CRS techniques, with spectral coverage, spectral resolution and pixel dwell time.

List of abbreviations:
ADC Analog-to-Digital Converter
AOM Acousto-Optic Modulator
AOPDF Acousto-Optic Programmable Dispersive Filter
AOTF Acousto Optic Tunable Filter
BD-RIKE Balanced Detection RIKE
TAMP Tunable AMPlifier
CARS Coherent Anti-Stokes Raman Scattering
CCD Charge Coupled Device
CRS Coherent Raman Scattering
CW Contituous Wave
DM Dichroic Mirror
DMD Digital Micromirror Device
EDFA Erbium Doped Fiber Amplifier
EM- CCD Electron-Multiplying Charge-Coupled Device.
EOM Electro-Optic Modulator
FDML Frequency-Domani mode-locked
FM-CARS Frequency modulation CARS
FSRS Femtosecond Stimulated Raman Scattering
FT Fourier Transform
FT-CARS Fourier Transform CARS
GM Galvanometer Mirror
GVD Group Velocity Dispersion
H&E hematoxylin and eosin
HNF Highly Nonlinear Fiber
I-CARS Interferometric CARS
IFD Instantaneous Frequency Difference
IRS Inverse Raman Scattering
ISRS Impulsive Stimulated Raman Scattering
LO Local Oscillator
LPF Long-pass filter
MEM Maximum Entropy Method
MIR Mid-Infrared
NIR Near-Infrared
NRB Non-Resonant Background
OHD-RIKE Optically Heterodyne RIKE
OMA Optical Multichannel Analyzer
OPA Optical Parametric Amplifier
OPO Optical Parametric Oscillator

PCF Photonic Crystal Fiber
PM Phase Modulated
PPLN Periodically Poled Lithium Niobate
PTS Photonic Time Stretch
RIKE Raman Induced Kerr Effect
SC supercontinuum
SF Spectral Focusing
SF-CARS Spectral Focusing CARS
SHG Second Harmonic Generation
SLM Spatial light modulator
SNR Signal-to-Noise Ratio
SPF Short-pass filter
SR Spontaneous Raman
SRG Stimulated Raman Gain
SRL Stimulated Raman Loss
SRS Stimulated Raman Scattering
STE-SRS Spectrally Tailored Excitation
TDKK Time Domain Kramers-Kronig
TICO Time encoded Raman
TL Transform-Limited
TR- CARS Time Resolved CARS
TWINS Translating-Wedge-based Identical pulses eNcoding System.
WLC White Light Continuum
WP Wollaston prism
XPM Cross Phase Modulation
YDFA ytterbium Doped Fiber Amplifier

Keywords: biomedical imaging, label-free microscopy, coherent Raman microscopy, coherent Anti-Stokes Raman scattering, stimulated Raman scattering.

References

[1]   J.B. Pawley, *Handbook of Biological Confocal Microscopy*, 3rd ed. (Springer, New York, 2006).

[2]   M. Bruchez Jr., M. Moronne, P. Gin, S. Weiss, and A. Paul Alivisatos, *Science* **281**, 2013-2016 (1998).

[3]   R.Y. Tsien, *Annu. Rev. Biochem.* **67**, 509–544 (1998).

[4]   R. Bhargava, *Appl. Spectrosc.* **66**, 1091–1120 (2012).

[5]   G. Turrell and J. Corset, *Raman microscopy: developments and applications* (Academic, 1996).

[6]   M. Ghomi, *Applications of Raman spectroscopy to biology: from basic studies to disease diagnosis* (IOS, 2012).

[7]   G. J. Puppels, F. F. M. de Mul, C. Otto, J. Greve, M. Robert-Nicoud, D. J. Arndt-Jovin, and T. M. Jovin, *Nature* **347**, 301-303 (1990).

[8]   N. Stone, C. Kendall, J. Smith, P. Crow, and H. Barr, *Faraday Discuss.* **126**, 141–157 (2004).

[9]   A. S. Haka, K. E. Shafer-Peltier, M. Fitzmaurice, J. Crowe, R. R. Dasari, and M. S. Feld, *Natl. Acad. Sci. USA* **102**, 12371-12376 (2005).

[10]   C. Kendall, M. Isabelle, F. Bazant-Hegemark, J. Hutchings, L. Orr, J. Babrah, R. Baker, and N. Stone, *Analyst* **134**, 1029-1045 (2009).

[11]   M. Kirsch, G. Schackert, R. Salzer, C. Krafft, *Anal. Bioanal. Chem.* **398**, 1707-1713 (2010).

[12]   U. Neugebauer, T. Bocklitz, J. H. Clement, C. Krafft, and J. Popp, *Analyst* **135**, 3178–3182 (2010).

[13]   G. J. Thomas jr., *Annu. Rev. Biophys. Biomol. Struct.* **28**, 1-27 (1999).

[14]   S. Sunder, R. Mendelsohn, and H. J. Bernstein, *Chem. Phys. Lipids* **17**, 456–465 (1976).

[15]   M. Noestheden, Q. Hu, L.-L. Tay, A. M. Tonary, A. Stolow, R. MacKenzie, J. Tanha, and J. P. Pezacki, *Bioorg. Chem.* **35**, 284–293 (2007).

[16]   H. Yamakoshi, K. Dodo, M. Okada, J. Ando, A. Palonpon, K. Fujita, S. Kawata, and M. Sodeoka, *J. Am. Chem. Soc.* **133**, 6102-6105 (2011).

[17]   C. Evans and X. S. Xie, *Annu. Rev. Anal. Chem.* **1**, 883-909 (2008).

[18]   J.-X. Cheng and X. S. Xie, *Coherent Raman Scattering Microscopy* (CRC Press, Boca Raton, FL, 2013).

[19]   W. Denk, J.H. Strickler, and W.W. Webb, *Science* **248**, 73–76 (1990).

[20]   M. D. Duncan, J. Reintjes, and T. J. Manuccia, *Opt. Lett.* **7**, 350–352 (1982).

[21]   A. Zumbusch, G. R. Holtom, and X. S. Xie, *Phys. Rev. Lett.* **82**, 4142-4145 (1999).

[22]   M. Hashimoto, T. Araki, S. Kawata, *Opt. Lett.* **24**, 1768-1770 (2000).

[23]   A. Owyoung and E. D. Jones, *Opt. Lett.* **1**, 152-154 (1977).

[24]   C. W. Freudiger, W. Min, B. G. Saar, S. Lu, G. R. Holtom, C. He, J. C. Tsai, J. X. Kang, and X. S. Xie, *Science* **322**, 1857-1861 (2008).

[25]   P. Nandakumar, A. Kovalev, and A. Volkmer, *New J. Phys.* **11**, 033026 (2009).

[26]   C. L. Evans, E. O. Potma, M. Puoris'haag, D. Côté, C. P. Lin, and X. Sunney Xie, *Proc. Natl. Acad. Sci. USA* **102**, 16807-16812 (2005).

[27]   B. G. Saar, C. W. Freudiger, J. Reichman, C. M. Stanley, G. R. Holtom, and X. S. Xie, *Science* **330**, 1368-1370 (2010).

[28]   W.J.Jones and B.P. Stoicheff, *Phys. Rev. Lett.* **13**, 657 - 659 (1964).

[29]   J. X. Cheng and X. S. Xie, *J. Phys. Chem. B* **108**, 827–840 (2004).

[30]   J. P. Pezacki, J.A. Blake, D. C. Danielson, D. C. Kennedy, R. K. Lyn, and R. Singaravelu, *Nat. Chem. Biol.* **7**, 137-145 (2011).

[31]   W. Min, C. W. Freudiger, S. Lu, and X. S. Xie, *Annu. Rev. Phys. Chem.* **62**, 507–530 (2011).

[32]   D. Zhang, P. Wang, M. N. Slipchenko, J.-X. Cheng, *Acc. Chem. Res.* **47**, 2282-2290 (2014).

[33]   C. H. Camp, Jr. and M. T. Cicerone, *Nat. Photonics* **9**, 295–305 (2015).

[34]   J.-X. Cheng and X. S. Xie, *Science* **350**, aaa8870 (2015).

[35]   M. T. Cicerone, C. H. Camp, Jr., *Analyst* **143**, 33-59 (2018).

[36]   G. P. Agrawal, *Nonlinear Fiber Optics*, 4th edn., (Academic Press, New York, USA, 2007).

[37]   G. L. Eesley, *J. Quant. Spectrosc. Radiat. Transfer* **22**, 507-576 (1979).

[38]   C. H. Camp, Jr., Y. J. Lee, J. M. Heddleston, C. M. Hartshorn, A. R. H. Walker, J. N. Rich, J. D. Lathia, and M. T. Cicerone, *Nat. Photonics* **8**, 627–634 (2014).

[39]   Y. Ozeki, F. Dake, S. Kajiyama, K. Fukui, and K. Itoh, *Opt. Express* **17**, 3651-3658 (2009).

[40]   P. Samineni, B. Li, J. W. Wilson, W. S. Warren, and M. C. Fischer, *Opt. Lett.* **37**, 800-802 (2012).

[41]   D. Fu, T. Ye, G. Yurtsever, W. S. Warren, and T. E. Matthews, *J. Biomed. Opt.* **12**, 054004 (2007).

[42]   P. J. Campagnola, H.A. Clark, W.A. Mohler, A. Lewis, and L.M. Loew, *Nature Biotech.* **21**, 1356–1360 (2003).

[43]   E. O. Potma, D. J. Jones, J.-X. Cheng, X. S. Xie, and J. Ye, *Opt. Lett.* **27**, 1168-1170 (2002).

[44]   F. Ganikhanov, S. Carrasco, X. S. Xie, M. Katz, W. Seitz, and D. Kopf, *Opt. Lett.* **31**, 1292-1294 (2006).

[45]   G. Krauss, T. Hanke, A. Sell, D. Träutlein, A. Leitenstorfer, R. Selm, M. Winterhalder, and A. Zumbusch, *Opt. Lett.* **34**, 2847-2849 (2009).

[46]   M. Marangoni, A. Gambetta, C. Manzoni, V. Kumar, R. Ramponi, and G. Cerullo, *Opt. Lett.* **34**, 3262–3264 (2009).

[47]   A. Gambetta, V. Kumar, G. Grancini, D. Polli, R. Ramponi, G. Cerullo, and M. Marangoni, *Opt. Lett.* **35**, 226-228 (2010).

[48]   C. Riek, C. Kocher, P. Zirak, C. Kölbl, P. Fimpel, A. Leitenstorfer, A. Zumbusch, and D. Brida, *Opt. Lett.* **41**, 3731-3734 (2016).

[49]   Ch. W. Freudiger, W. Yang, G. R. Holtom, N. Peyghambarian, X. S. Xie, and K. Q. Kieu, *Nat. Photonics* **8**, 153-159 (2014).

[50]   N. Coluccelli, V. Kumar, M. Cassinerio, G. Galzerano, M. Marangoni, and G. Cerullo, *Opt. Lett.* **39**, 3090-3093 (2014).

[51]   M. Baumgartl, M. Chemnitz, C. Jauregui, T. Meyer, B. Dietzek, J. Popp, J. Limpert, and A. Tünnermann, *Opt. Express* **20**, 4484-4493 (2012).

[52]   Th. Gottschall, M. Baumgartl, A. Sagnier, J. Rothhardt, C. Jauregui, J. Limpert, and A. Tünnermann, *Opt. Express* **20**, 12004-12013 (2012).

[53]   M. Chemnitz, M. Baumgartl, T. Meyer, C. Jauregui, B. Dietzek, J. Popp, J. Limpert, and A. Tünnermann, *Opt. Express* **20**, 26583-26595 (2012).

[54]   S. Lefrancois, D. Fu, G. R. Holtom, L. Kong, W. J. Wadsworth, P. Schneider, R. Herda, A. Zach, X. S. Xie, and F. W. Wise, *Opt. Lett.* **37**, 1652-1654 (2012).

[55]   E. S. Lamb, S. Lefrancois, M. Ji, W. J. Wadsworth, X. S. Xie, and F. W. Wise, *Opt. Lett.* **38**, 4154-4157 (2013).

[56]   T. Steinle, V. Kumar, A. Steinmann, M. Marangoni, G. Cerullo, and H. Giessen, *Opt. Lett.* **40**, 593-596 (2015).

[57]   T. Steinle, V. Kumar, M. Floess, A. Steinmann, M. Marangoni, C. Koch, C. Wege, G. Cerullo, and H. Giessen, *Light-Sci. Appl.* **5**, e16149 (2016).

[58]   J.-X. Cheng, A. Volkmer, L. D. Book, and X. S. Xie, *J. Phys. Chem. B* **105**, 1277–1280 (2001).

[59]   T. Hellerer, C. Axäng, Ch. Brackmann, P. Hillertz, M. Pilon, and A. Enejder, *Proc. Natl. Acad. Sci. USA* **104**, 14658-14663 (2007).

[60]   A. Zumbusch, W. Langbein, and P. Borri, *Prog. Lipid Res.* **52**, 615–632 (2013).

[61]   Y. Yu, P. V. Ramachandran, M. C. Wang, *Biochim. Biophysica Acta* **1841**, 1120-1129 (2014).

[62]   F. Ganikhanov, C. L. Evans, B. G. Saar, and X. S. Xie, *Opt. Lett.* **31**, 1872-1874 (2006).

[63]   Y. S. Yoo, D.-H. Lee, and H. Cho, *Opt. Lett.* **32**, 3254-3256 (2007).

[64]   E. O. Potma, C. L. Evans, and X. S. Xie, *Opt. Lett*. **31**, 241-243 (2006).

[65]   E. R. Andresen, S. R. Keiding, and E. O. Potma, *Opt. Express* **14**, 7246-7251 (2006).

[66]   M. Jurna, J. P. Korterik, C. Otto, and H. L. Offerhaus, *Opt. Express* **15**, 15207-15213 (2007).

[67]   M. Jurna, J. P. Korterik, C. Otto, J. L. Herek, and H. L. Offerhaus, *Opt. Express* **16**, 15863-15869 (2007).

[68]   D. Zhang, M. N. Slipchenko, D. E. Leaird, A. M. Weiner, and J.-X. Cheng, *Opt. Express* **21**, 13864-13874 (2013).

[69]   P. Berto, E. R. Andresen, and H. Rigneault, *Phys. Rev. Lett.* **112**, 053905 (2014).

[70]   K. Nose, Y. Ozeki, T. Kishi, K. Sumimura, N. Nishizawa, K. Fukui, Y. Kanematsu, and K. Itoh, *Opt. Express* **20**, 13958-13965 (2012).

[71]   F. Crisafi, V. Kumar, T. Scopigno, M. Marangoni, G. Cerullo, and D. Polli, *Sci. Rep.* **7**, 10745 (2017).

[72]   A. D. G. Nunn, T. Scopigno, N. Pediconi, M. Levrero, H. Hagman, J. Kiskis, and A. Enejder *Sci. Rep.* **6**, 28025 (2016).

[73]   H. Wang, Y. Fu, P. Zickmund, R. Shi, and J.-X. Cheng, *Biophys. J.* **89**, 581-591 (2005).

[74]   Y. Fu, T. B. Huff, H.-W. Wang, J.-X. Cheng, and H. Wang, *Opt. Express* **16**, 19396-19409 (2008).

[75]   E. Bélanger, S. Bégin, S. Laffray, Y. De Koninck, R. Vallée, and D. Côté, *Opt. Express* **17**, 18419-18432 (2009).

[76]   G. de Vito, I. Tonazzini, M. Cecchini, and V. Piazza, *Opt. Express* **22**, 13733-13743 (2014).

[77]   F.-K. Lu, S. Basu, V. Igras, M. P. Hoang, M. Ji, D. Fu, G. R. Holtom, V. A. Neel, C. W. Freudiger, D. E. Fisher, and X. S. Xie, *Proc. Natl. Acad. Sci. USA*. **112**, 11624–11629 (2015).

[78]   D. Fu, J. Zhou, W.S. Zhu, P.W. Manley, Y.K. Wang, T. Hood, A. Wylie and X. S. Xie. *Nat. Chem.* **6**, 614-622 (2014).

[79]   R. Mittal, M. Balu, T. Kraiseva, E. O. Potma, L. Elkeeb, C. B. Zachary and P. Wilder-Smith, *Laser Surg. Med.* **45**, 496-502 (2013).

[80]   C. W. Freudiger, R. Pfannl, D. A. Orringer, B. G. Saar, M. Ji, Q. Zeng, L. Ottoboni, W. Ying, C. Waeber, J. R. Sims, P. L. De Jager, O. Sagher, M. A. Philbert, X. Xu, S. Kesari, X. S. Xie and G. S. Young, *Lab. Investig.* **92**, 1492-1502 (2012).

[81]   M. Ji, D. A. Orringer, C. W. Freudiger, S. Ramkissoon, X. Liu, D. Lau, A. J. Golby, I. Norton, M. Hayashi, N. Y. R. Agar, G. S. Young, C. Spino, S. Santagata, S. Carmelo-Piragua, K. L. Ligon, O. Sagher and X. S. Xie, *Sci. Transl. Med.* **5**, 201ra119 (2013).

[82]   M. Ji, S. Lewis, S. Camelo-Piragua, S.H. Ramkissoon, M. Snuderl, S. Venneti, A. Fisher-Hubbard, M.Garrard, D. Fu, A. C.Wang, J. A.Heth, C. O. Maher, N. Sanai, T. D. Johnson, C. W. Freudiger, O. Sagher, X. S. Xie and D. A. Orringer, *Sci. Transl. Med.* **7**, 309ra163 (2015).

[83]   D. A. Orringer, B. Pandian, Y. S. Niknafs, T. C. Hollon, J. Boyle, S. Lewis, M. Garrard, S. L. Hervey-Jumper, H. J. L. Garton, C. O. Maher, J. A. Heth, O. Sagher, D. A. Wilkinson, M. Snuderl, S. Venneti, S. H. Ramkissoon, K. A. McFadden, A. Fisher-Hubbard, A. P. Lieberman, T. D. Johnson, X. S. Xie, J. K. Trautman, C. W. Freudiger and S. Carmelo-Piragua, *Nat. Biomed. Eng.* **1**, 0027 (2017).

[84]   T. Hellerer, A. M. K. Enejder and A. Zumbusch, *Appl. Phys. Lett.* **85**, 25–27 (2004).

[85]   I. Rocha-Mendoza, W. Langbei and P. Borri, *Appl. Phys. Lett.* **93**, 201103 (2008).

[86]   A. F. Pegoraro, A. Ridsdale, D. J. Moffatt, Y. Jia, J. P. Pezacki and A. Stolow, *Opt. Express.* **17**, 2984-2996 (2009).

[87]   A. D. Slepkov, A. Ridsdale, A. F. Pegoraro,D. J. Moffatt, and A. Stolow, *Biomed. Opt. Express* **1**, 1347-1357 (2010).

[88] L. B. Mostaço-Guidolin, M. G. Sowa, A. Ridsdale, A. F. Pegoraro, M. S. D. Smith, M. D. Hewko, E. K. Kohlenberg, B. Schattka, M. Shiomi, A. Stolow, and A. C.-T. Ko, *Biomed. Opt. Express* **1**, 59-73, (2010).

[89] W. Langbein, I. Rocha-Mendoza, and P. Borri, *Appl. Phys. Lett.* **95**, 081109 (2009).

[90] I. Pope, W. Langbein, P. Watson, and P. Borri, *Opt. Express* **21**, 7096-7106 (2013).

[91] F. Masia, A. Glen, P. Stephens, P. Borri, and W. Langbein, *Anal. Chem.* **85**, 10820−10828 (2013).

[92] C. D. Napoli, I. Pope, F. Masia, P. Watson, W. Langbein, and Paola Borri, *Biomed. Opt. Express* **5**, 1378-1390 (2014).

[93] C. D. Napoli, I. Pope, F. Masia, W. Langbein, , P. Watson and Paola Borri, *Anal. Chem.* **88**, 3677−3685 (2016).

[94] B.-C. Chen, J. Sung, X. Wu, and S.-H. Lim, *J. Biomed. Opt.* **16**, 021112 (2011)

[95] M. Muller and J. M. Schins, *J. Phys. Chem. B* **106**, 3715-3723 (2002).

[96] J. X. Cheng, A. Volkmer, L. D. Book and X. S. Xie, *J. Phys. Chem. B* **106**, 8493-8498 (2002).

[97] T. W. Kee and M. T. Cicerone, *Opt. Lett.* **29**, 2701-2703 (2004).

[98] H. Kano and H. Hamaguchi, *Appl. Phys. Lett.* **86**, 121113 (2005).

[99] H. Kano and H. Hamaguchi, *Opt. Express* **13**, 1322-1327 (2005).

[100] B. von –, L. Meyer, M. Motzkus, *J. Raman Spectroscopy* **38**, 916-926 (2007).

[101] C. Pohling, T. Buckup, A. Pagenstecher, and M. Motzkus, *Biomed. Opt. Express* **2**, 2110-2116 (2011).

[102] C. Pohling, T. Buckup, M. Motzkus, *J. Biomed. Opt.* **16**, 021105 (2011).

[103] E. M. Vartiainen, *J. Opt. Soc. Am. B* **9**, 1209-1214 (1992).

[104] E. M. Vartiainen, H. A. Rinia, M. Müller and M. Bonn, *Opt. Express* **14**, 3622-3630 (2006).

[105] Y. Liu, Y. J. Lee and M. T. Cicerone, *Opt. Lett.* **34**, 1363-1365 (2009).

[106] M. T. Cicerone, K. A. Aamer, Y. J. Lee and E. Vartiainen, *J. Raman Spectrosc.* **43**, 637–643 (2012).

[107] M. Okuno, H. Kano, P. Leproux, V. Conderc and H. Hamaguchi, *Opt. Lett.* **32**, 3050-3052 (2007).

[108] M. Okuno, H. Kano, P. Leproux, V. Couderc and H. O. Hamaguchi, *Opt. Lett.* **33**, 923–925 (2008).

[109] J. M. Dudley, G. Genty and S. Coen, *Rev. Mod. Phys.* **78,** 1135-1184 (2006)

[110] P. Leproux, V. Couderc, A. de Angelis, M. Okuno, H. Kano and H. Hamaguchi, *J. Raman Spectrosc.* **42**, 1871–1874 (2011).

[111] H. Mikami, M. Shiozawa, M. Shirai and K. Watanabe, *Opt. Express* **23**, 2872-2878 (2015).

[112] H. Mikami, M. Shiozawa, M. Shirai and K. Watanabe, *Opt. Express* **23**, 17217-17222 (2015).

[113] M. Okuno, H. Kano, P. Leproux, V. Couderc, J. Day, M. Bonn and H.-O. Hamaguchi, *Angew. Chem., Int. Ed.* **49**, 6773-6777 (2010).

[114] F. Tauser, F. Adler, and A. Leitenstorfer, *Opt. Lett.* **29**, 516-518 (2004).

[115] Y. X. Yan and K. A. Nelson, *J. Chem. Phys.* **87**, 6257-6265 (1987).

[116] S. Ruhman, A.G. Joly and K.A. Nelson, *IEEE J. Quantum Electron.* **24**, 460-469 (1988).

[117] A. Laubereau and W. Kaiser, *Rev. Mod. Phys.* **50**, 607-665 (1978).

[118] F. M. Kamga and M. G. Sceats, *Opt. Lett.* **5**, 126-128 (1980).

[119] D. Pestov, G.O. Ariunbold, X. Wang, R.K. Murawski, V.A. Sautenkov, A.V. Sokolov and M.O. Scully, *Opt. Lett.* **32**, 1725-1727 (2007).

[120] D. Pestov, R. K. Murawski, G. O. Ariunbold, X. Wang, M. Zhi, A. V. Sokolov, V. A. Sautenkov, Y. V. Rostovtsev, A. Dogariu, Y. Huang and M. O. Scully, *Science* **316**, 265 (2007).

[121] R. Selm, M. Winterhalder, A. Zumbusch, G. Krauss, T. Hanke, A. Sell and A. Leitenstorfer, *Opt. Lett.* **35**, 3282-3284 (2010).

[122] F. Adler, A. Sell, F. Sotier, R. Huber and A. Leitenstorfer, *Opt. Lett.* **32**, 3504-3506 (2007).

[123] M. Marangoni, D. Brida, M. Quintavalle, G. Cirmi, F. M. Pigozzo, C. Manzoni, F. Baronio, A. D. Capobianco and G. Cerullo, *Opt. Express* **15**, 8884-8891 (2007).

[124] K. Moutzouris, F. Adler, F. Sotier, D. Träutlein and A. Leitenstorfer, *Opt. Lett.* **31**, 1148-1150 (2006).

[125] N. Dudovich, D. Oron and Y. Silberberg, *Nature* **418**, 512-514 (2002).

[126] A. M. Weiner, *Rev. Sci. Instrum.* **71**, 1929-1960 (2000).

[127] A. M. Weiner, D. E. Leaird, G. P. Wiederrecht, and K. A. Nelson, *Science* **247**, 1317-1319 (1990).

[128] B. von Vacano, W. Wohlleben, M. Motzkus, *J. Raman Spectrosc.* **37**, 404-410 (2006).

[129] V. V. Lozovoy, B. Xu, J. C. Shane, and M. Dantus, *Phys. Rev. A* **74**, 041805(R) (2006).

[130] M. T. Bremer, and M. Dantus, *Appl. Phys. Lett.* **103**, 061119 (2013).

[131] J. Rehbinder, L. Brückner, A. Wipfler, T. Buckup, M. Motzkus, *Opt. Express* **22**, 28709-28797 (2014).

[132] D. Oron, N. Dudovich and Y. Silberberg, *Phys. Rev. Lett.* **89**, 273001 (2002).

[133] O. Katz, A. Natan, Y. Silberberg, and S. Rosenwaks, *Appl. Phys. Lett* **92**, 171116 (2008).

[134] D. Oron, N. Dudovich and Y. Silberberg, *Phys. Rev. Lett.* **90**, 213902 (2003).

[135] S. Roy, P. Wrzesinski, D. Pestov, T. Gunaratne, M. Dantus, and J. R. Gord, *Appl. Phys. Lett.* **95**, 074102 (2009).

[136] H. Li, D. A. Harris, B. Xu, P. J. Wrezesinski, V. V. Lozovoy, and M. Dantus, *Appl. Optics* **48**, B17-B22 (2009).

[137] S.-H. Lim, A. G. Caster, and S. R. Leone, *Phys. Rev. A* **72**, 041803(R) (2005).

[138] S.-H. Lim, A. G. Caster, O. Nicolet, and S. R. Leone, *J. Phys. Chem B* **110**, 5196-5204 (2006).

[139] L. Lepetit, G. Chériaux, and M Joffre, *J. Opt. Soc. Am. B* **12**, 2467-2474 (1995).

[140] B. von Vacano, T. Buckup, and M. Motzkus, *Opt. Lett.***31**, 2495-2497 (2006).

[141] C. Müller, T. Buckup, B. von Vacano, M. Motzkus, *J. Raman Spectrosc.* **40**, 809-816 (2009).

[142] A. Wipfler, T. Buckup, and M. Motzkus, *Appl. Phys. Lett.* **100**, 071102 (2012).

[143] A. Natan, O. Katz, S. Rosenwaks, and Y. Silberberg, *Proceedings of Ultrafast Phenomena XVI*, Springer Series in Chemical Physics **92**, 985–987 (2009).

[144] O. Katz, J. M. Levitt, E. Grinvald, and Y. Silberberg, *Opt. Express* **18**, 22693-22701 (2010).

[145] A. Natan, J. M. Levitt, L. Graham, O. Katz, and Y. Silberberg, *Appl. Phys. Lett.* **100**, 051111 (2012).

[146] Y. Shen, D. V. Voronine, A. V. Sokolov, and M. O. Scully, *Opt. Lett.* **40**, 1223-1226 (2015).

[147] T. Suzuki and K. Misawa, *Opt. Express*, **19**, 11463-11470 (2011).

[148] B. von Vacano and M. Motzkus, *Phys. Chem. Chem. Phys.* **10**, 681-691 (2008).

[149] L. Brückner, T. Buckup, and M. Motzkus, *Opt. Lett.* **22**, 5204-5207 (2015).

[150] L. Brückner, T. Buckup, and M. Motzkus, *J. Opt. Soc. Am. B* **33**, 1482-1492 (2016).

[151] M. T. Bremer and M. Dantus, *Appl. Phys. Lett.* **103**, 061119 (2013).

[152] R. Glenn and M. Dantus, *J. Phys. Chem. Lett* **7**, 117-125 (2016).

[153] T. Ito, Y. Obara, and K. Misawa, *J. Opt. Soc. Am. B* **34**, 1004-1015 (2017).

[154] J. P. Ogilvie, E. Beaurepaire, A. Alexandrou and M. Joffre, *Opt. Lett.* **31**, 480-482 (2006).

[155] M. Cui, M. Joffre, J. Skodack and J.P. Ogilvie, *Opt. Express* **14**, 8448-8458 (2006).

[156] K. Hashimoto, M. Takahashi, T. Ideguchi and K. Goda, *Sci. Rep.* **6**, 21036 (2016).

[157] M. Tamamitsu, Y. Sakaki, T. Nakamura, G. K. Podagatlapalli, T. Ideguchi and K. Goda, *Vib. Spectrosc.* **91**,163-169 (2017) .

[158] A.S. Duarte, C. Schnedermann and P. Kukura et al., *Sci. Rep.* **6**, 37516 (2016).

[159] F. Keilmann, C. Gohle and R. Holzwarth, *Opt. Lett.* **29**, 1542-1544 (2004).

[160] Ian Coddington, Nathan Newbury and William Swann, *Optica* **3**, 414-426 (2016).

[161] S. T. Cundiff and J. Ye, *Rev. Mod. Phys.* **75**, 325-342 (2003).

[162] T. Ideguchi, S. Holzner, B. Bernhardt, G. Guelachvili, N. Picqué and T. W. Hänsch, *Nature* **502**, 355-358 (2013).

[163] K. J. Mohler, B. J. Bohn, M. Yan, G. Mélen, T. W. Hänsch and N. Picqué, *Opt. Lett.* **42**, 318-321 (2017).

[164] K. Chen, T. Wu, T. Chen, H. Wei, H. Yang, T. Zhou and Y. Li, *Opt. Lett.* **42**, 3634-3637 (2017).

[165] N. Coluccelli, C.R. Howle, K. McEwan, Y. Wang, T. Teddy Fernandez, A. Gambetta, P. Laporta and G. Galzerano, *Opt. Lett.* **42**, 4683-4686 (2017)

[166] H.T. Beier, G.D. Noojin and B.A. Rockwell, *Opt. Express* **19**, 18885-18892 (2011)

[167] E. R. Andresen, P. Berto and H. Rigneault, *Opt. Lett.* **36**, 2387–2389 (2011).

[168] C, W, Freudiger, W. Min, G. R. Holtom, B. Xu, M. Dantus and X.S. Xie, *Nat. Photonics* **5**, 103-109 (2011).

[169] J. Rehbinder, C. Pohling, T. Buckup, and M. Motzkus, *Opt. Lett.* **35**, 3721-3723 (2010).

[170] Y. Ozeki, W. Umemura, Y. Otsuka, S. Satoh, H. Hashimoto, K. Sumimura, N. Nishizawa, K. Fukui and K. Itoh, *Nat. Photonics* **6**, 845-851 (2012).

[171] Y. Ozeki, Y. Kitagawa, K. Sumimura, N. Nishizawa, W. Umemura, Sh. Kajiyama, K. Fukui and K. Itoh, *Opt. Express* **18**, 13708-13719 (2010).

[172] Y. Ozeki, W. Umemura, K. Sumimura, N. Nishizawa, K. Fukui and K. Itoh, *Opt. Lett.* **37**, 431-433 (2012).

[173] L. Kong, M. Ji, G. R. Holtom, D. Fu, C. W. Freudiger, and X. S. Xie, *Opt. Lett.* **38**, 145-147 (2013).

[174] E. R. Andresen, P. Berto and H. Rigneault, *Opt. Lett.* **36**, 2387-2389 (2011).

[175] D. Fu, G. Holtom, C. Freudiger, X. Zhang and X. S. Xie, *J. Phys. Chem. B* **117**, 4634-4640 (2013).

[176] B. Liu, H. J. Lee, D. Zhang, C. S. Liao, N. Ji, Y. Xia and J.-X. Cheng, *Appl. Phys. Lett.* **106**, 173704 (2015).

[177] D. Huang, E. A. Swanson, C. P. Lin, J. S. Schuman, W. G. Stinson, W. Chang, M. R. Hee, T. Flotte, K. Gregory, C. A. Puliafito, and J. G. Fujimoto, *Science* **254**, 1178-1181 (1991).

[178] C.-S. Liao, K.-C. Huang, W. Hong, A. J. Chen, C. Karanja, P. Wang, G. Eakins and J.-X. Cheng, *Optica* **3**, 1377-1380 (2016).

[179] C.-S. Liao, P. Wang, C. Y. Huang, P. Lin, G. Eakins, R. T. Bentley, R. Liang, and J. X. Cheng, *ACS Photonics*, Just Accepted Manuscript, DOI: 10.1021/acsphotonics.7b01214.

[180] R. He, Z. Liu, Y. Xu, W. Huang, H. Ma and M. Ji, *Opt. Lett.* **42**, 659-662 (2017).

[181] G. J. Tearney, B. E. Bouma and J. G. Fujimoto, *Opt. Lett.* **22**, 1811-1813 (1997).

[182] P. Tournois, *Opt. Commun.* **140**, 245-249 (1997).

[183] F. Verluise, V. Laude, Z. Cheng, C. Spielmann and P. Tournois, *Opt. Lett.* **25**, 575–577 (2000).

[184] M. S. Alshaykh, C.-S. Liao, O. E. Sandoval, G. Gitzinger, N. Forget, D. E. Leaird, J.-X. Cheng and A M. Weiner, *Opt. Lett.* **42**, 1548-1551 (2017).

[185] R. He, Y. Xu, L. Zhang, S. Ma, X. Wang, D. Ye and M. Ji, *Optica* **4**, 44-47 (2017).

[186] W. Yang, A. Li, Y. Suo, F.-K. Lu, and X. S. Xie, *Opt. Lett* **42**, 523-526 (2017).

[187] S. Karpf, M. Eibl, W. Wieser, T. Klein and R. Huber, *Nat. Commun.* **6**, 6784 (2015).

[188] W. Wieser, B. R. Biedermann, T. Klein, C. M. Eigenwillig and R. Huber, *Opt. Express* **18**, 14685-14704 (2010).

[189] P. Berto, C. Scotté, F. Galland, H. Rigneault and H. B. de Aguiar, *Opt. Lett.* **42**, 1696-1699 (2017)

[190] M. Hashimoto, T. Minamikawa, T. Araki, Proc. of SPIE **7569**, 75690Q (2010).

[191] Z. Meng, G. I. Petrov and V. V. Yakovlev, *Sci. Rep.* **6**, 20017 (2016).

[192] H. Cahyadi, J. Iwatsuka, T. Minamikawa, H. Niioka, T. Araki, M. Hashimoto, *J. Biomed. Opt.* **18**, 096009 (2013).

[193] K. Mars, De X. Lioe, S. Kawahito, K. Yasutomi, K. Kagawa, T. Yamada and Mamoru Hashimoto, *Sensors* **17**, 2581 (2017).

[194] D. Fu, F. K. Lu, X. Zhang, Ch. Freudiger, D. R. Pernik, G. Holtom and X. S. Xie, *J. Am. Chem. Soc.* **134**, 3623−3626 (2012).

[195] D. W. McCamant, P. Kukura, S. Yoon and R. A. Mathies, *Rev. Sci. Instrum.* **75**, 4971-4980 (2004).

[196] P. Kukura, D. W. McCamant and R. A. Mathies, *Annu. Rev. Phys. Chem.* **58**, 461-488 (2007).

[197] P. Kukura, D. W. McCamant, S. Yoon, D. B. Wandschneider and R. A. Mathies, *Science* **310**, 1006 (2005).

[198] C. Fang, R. R. Frontiera, R. Tran and R. A. Mathies, *Nature* **462**, 200-204 (2009).

[199] E. Ploetz, S. Laimgruber, S. Berner, W. Zinth and P. Gilch, *Appl. Phys. B* **87**, 389-393 (2007).

[200] D. Polli, L. Lüer and G. Cerullo, *Rev. Sci. Instrum.* **78**, 103108 (2007).

[201] E. Ploetz, B. Marx, T. Klein, R. Huber and P. Gilch, *Opt. Express* **17**, 18612-18620 (2009).

[202] W. Rock, M. Bonn and S. H. Parekh, *Opt. Express* **21**, 15113-15120 (2013).

[203] L. Czerwinski, J. Nixdorf, G. Di Florio and P. Gilch, *Opt. Lett.* **41**, 3021-3024 (2016)

[204] R. A. Light, R. J. Smith, N. S. Johnston, S. D. Sharples, M. G. Somekh, and M. C. Pitter, Proc. SPIE **7570**, 75700U (2010).

[205] D. Heiman, R. W. Hellwarth, M. D. Levenson and G. Martin, *Phys. Rev. Lett.* **36**, 189-192 (1976).

[206] S. Shim and R. A. Mathies, *J. Raman Spectrosc.* **39**, 1526–1530 (2008).

[207] B. R. Bachler, M. E. Fermann and J. P. Ogilvie, *Opt. Express* **20**, 835-844 (2012).

[208] M. D. Levenson, S. S. Kano, *Introduction to Nonlinear Laser Spectroscopy* (Academic Press, San Diego, USA, 1988).

[209] D. Klenerman, *Opt. Lett.* **16**, 838-839 (1991).

[210] M. O. McAnally, Y. Guo, G. Balakrishnan, G. C. Schatz, and R. P. Van Duyne, *Opt. Lett.* **41**, 5357-5360 (2016).

[211] C. W. Freudiger, M. B. Roeffaers, X. Zhang, B. G. Saar, W. Min, and X. S. Xie, *J. Phys. Chem. B* **115**, 5574-5581 (2011).

[212] V. Kumar, M. Casella, E. Molotokaite, D. Gatti, P. Kukura, C. Manzoni, D. Polli, M. Marangoni, and G. Cerullo, *Phys. Rev. A* **86**, 053810 (2012).

[213] F.-K. Lu, M. Ji, D. Fu, X. Ni, C. W. Freudiger, G. Holtom, and X. S. Xie, *Mol. Phys.* **110**, 1927-1932 (2012).

[214] K. Seto, Y. Okuda, E. Tokunaga and T. Kobayashi, *Rev. Sci. Instrum.* **84**, 083705 (2013).

[215] K. Seto, Y. Okuda, E. Tokunaga and T. Kobayashi, *J. Phys. D. Appl. Phys.* **47**, 345401 (2014).

[216] C.-S. Liao, M. N. Slipchenko, P. Wang, J. Li, S.-Y. Lee, R. A. Oglesbee and J.-X. Cheng, *Light Sci. Appl.* **4**, e265 (2015).

[217] M. N. Slipchenko, R. A. Oglesbee, D. Zhang . W. Wu and J.-X. Cheng, *J. Biophotonics* **5,** 801-807 (2012).

[218] A. Bhushan, F. Coppinger, and B. Jalali, *Electron. Lett.* **34**, 839–841 (1998).

[219] F. Coppinger, A. S. Bhushan and B. Jalali, *IEEE T. Microw. Theory* **47**, 1309–1314 (1999).

[220] A.M. Fard, S. Gupta and B. Jalali, *Laser Photonics Rev.* **7**, 207–263 (2013).

[221] D. Solli, C. Ropers, P. Koonath, and B. Jalali, *Nature* **450**, 1054–1057 (2007).

[222] G. Herink, B. Jalali, C. Ropers and D. R. Solli, *Nat. Photonics* **10**, 321–326 (2016).

[223] F. Saltarelli, V. Kumar, D. Viola, F. Crisafi, F. Preda, G. Cerullo and D. Polli, *Opt. Express* **24**, 21264-21275 (2016).

[224] S. Dobner, and C. Fallnich, *Appl. Phys. B* **122**, 278 (2016).

[225] C. H. Camp, Jr., S. Yegnanarayanan, A. A. Eftekhar, H. Sridhar and A. Adibi, *Opt. Express* **17**, 22879–22889 (2009).

[226] G. V. Oshovsky, G. Rago, J. P. R. Day, M. L. Soudijn, W. Rock, S. H. Parekh, G. Ciancaleoni, J. N. H. Reek and M. Bonn, *Anal. Chem.* **85**, 8923–8927 (2013).

[227] M. Windbergs, M. Jurna, H. L. Offerhaus, J. L. Herek, P. Kleinebudde and C. J. Strachan, *Anal. Chem.* **81**, 2085–2091 (2009).

[228] J. Réhault, F. Crisafi, V. Kumar, G. Ciardi, M. Marangoni, G. Cerullo and D. Polli, *Opt. Express* **23**, 25235-25246 (2015).

[229] S. P. Davis, M. C. Abrams and J. W. Brault, *Fourier Transform Spectrometry* (Elsevier, 2001).

[230] A. Papoulis, *Signal Analysis* (McGraw-Hill, New York, NY, USA, 1977).

[231] D. Brida, C. Manzoni and G. Cerullo, *Opt. Lett.* **37**, 3027–3029 (2012).

[232]   J. Réhault, M. Maiuri, A. Oriana and G. Cerullo, *Rev. Sci. Instrum.* **85**, 123107 (2014).

[233]   C.-S. Liao, P. Wang, P. Wang, J. Li, H. J. Lee, G. Eakins, J.-X. Cheng, *Sci. Adv.* **1**, e1500738 (2015).

[234]   N. Coluccelli, D. Viola, V. Kumar, A. Perri, M. Marangoni, G. Cerullo, and D. Polli, *Opt. Lett.* **42**,4545-4548 (2017).

Dario Polli is Associate Professor of physics in the Physics Department, Politecnico di Milano since 2014. His research interests include the generation and characterization of tunable femtosecond laser pulses and their application to pump-probe spectroscopy and microscopy of several samples such as carotenoids, light-harvesting systems, conjugated polymer films, bio-molecules, and carbon nanotubes. Recently, he focused his attention on coherent Raman spectroscopy and microscopy, developing several techniques for stimulated Raman scattering, coherent anti-Stokes Raman scattering, and Raman-induced Kerr effect. He was awarded with a European Research Council Consolidator Grant in 2015. He is also affiliated with the Italian Institute of Technology in Milan, Italy.

Vikas Kumar is a postdoctoral researcher at Physics Department, Politecnico di Milano. He has extensive experience working in the field of Coherent Raman spectroscopy and microscopy. He graduated as Ph.D. in Physics in 2012 at Politecnico di Milano, Milan; as M. Tech. in Laser science & Applications in 2007 at Devi Ahilya University, Indore; as M. Sc. in Physics in 2004 at Lucknow University, Lucknow. His current research interest involves source and technological development in nonlinear optics for fast broadband multi-photon spectroscopy and imaging.

Carlo Michele Valensise graduated in 2017 at University of Rome "La Sapienza". He is currently Ph. D. candidate at the Physics Department, Politecnico di Milano, Italy, within the ERC Consolidator Grant VIBRA. His research interest is mainly focused on Broadband Coherent Raman.

Marco Marangoni is Associate Professor in Physics at Politecnico di Milano. He boasts a long-standing experience in the field of nonlinear optics. His current research activity is focused on Coherent Raman spectroscopy and in the development of frequency comb synthesizers and of spectrometers for high-precision molecular spectroscopy. He is currently Director of the Lecco Research Unit of the Photonics and Nanotechnology Institute (IFN) of the National Research Council (CNR).

Giulio Cerullo is Full Professor at the Physics Department, Politecnico di Milano, Italy. His research focuses on the broad area known as ultrafast optical science, and concerns the generation of few-optical-cycle tunable light pulses and their application to ultrafast spectroscopy and nonlinear microscopy. He is a Fellow of the Optical Society of America and Chair of the Quantum electronics and Optics Division of the European Physical Society.

WILEY-VCH

Graphical Abstract

ToC entry: scheme of broadband coherent Raman scattering, combining a narrowband pump and a broadband Stokes beam. The nonlinear Raman spectrum can be detected either as CARS or as Sotkes beam amplification (SRS). The paper reviews the technical implementations of broadaband CARS and SRS.

ToC figure